MECHANICS OF MICRO AND NANOSCALE STRUCTURES IN SELF-ASSEMBLED SURFACE FEATURES, MOLECULAR MACHINES AND BIOMATERIALS

by

Seungjun Lee

A dissertation submitted in partial fulfillment
of the requirements for the degree of
Doctor of Philosophy
(Mechanical Engineering)
in The University of Michigan
2011

Doctoral Committee:

Associate Professor Wei Lu, Chair
Professor Lumin Wang
Assistant Professor Samantha Hayes Daly
Assistant Professor Anastasios John Hart

DEDICATION

This dissertation is dedicated to my family who always supported me with their warm hearts: to my parent who trusted me and supported me to achieve my goals; to my sister who cheered me and stayed with my parent instead me in Korea; to my aunt who encouraged me and stayed with my mother.

ACKNOWLEDGMENTS

I would like to deeply thank my advisor, Professor Wei Lu, for his guidance and support during my doctoral studies. He gave me a priceless opportunity to pursuit my doctoral degree in the University of Michigan and led me to an exciting field of nanotechnology. Great insight and systematic approach for solving problems that I learned from him will be strength in my life. I would like to thank Professor Lumin Wang for guiding me an interesting topic and giving me kind suggestions for successful research. I would also like to thank my committee members, Professor Samantha Daly and Professor John Hart for her and his invaluable discussions on my research. I especially thank Jonghyun Park, who gave me thoughtful advices and helpful discussions. I would like to thank the professors who gave me tremendous learning through their enthusiastic lectures. Additionally I want to thank my friends and people, who spent a wonderful time together in Ann Arbor: Jaewon Lee, Jaewook Lee, Jedo Kim, Sungkwon Hong, Il Yeo, Gisuk Hwang, Jonghun Lee, Jaewook Oh, Naomi, other church members and other Korean students in Mechanical Engineering who came here at the same year.

TABLE OF CONTENTS

LIST OF FIGURES

FIGURE

LIST OF APPENDICES

APPENDIX

ABSTRACT

This research is motivated by the interest to understand how physical forces affect the configurational change of small structures.

First, I report a mechanism that under an off-normal incident ion beam, ordered nanodroplets may emerge spontaneously on a solid surface. My continuum theory considers sputtering, deposition, wetting and surface energy. The simulations show that a competition between the mass supply and sputtering determines the stable size of the droplet, while the anisotropic mass flux drives the droplet to move. The balance of the flux leads to a hexagonal pattern. The shadow effect causes the droplets to line up perpendicular to the incident beam. The mechanism may be applicable to other systems to form ordered nanoscale features by self-assembly.

Next, I consider individual functional structures, and use molecular dynamics simulations to investigate the effect of force on stimulus-induced deformation of rotaxane-based artificial molecular muscles. Bistable rotaxanes are composed of ring and dumbbell-shaped backbone. Upon an external stimulus, the ring switches between two recognition sites along the backbone, enabling large deformation like molecular muscles. My study shows that a small external force slows down the shuttling motion, leading to longer actuation time to full extension. Larger force significantly reduces the traveling

distance of the ring and strain output. A maximum load exists which completely suppresses the shuttling motion.

Last, I extend research to living structures. I use light scattering experiment to detect normal and malaria-infected blood cells. The latter are stiffer with different scattering property. By measuring the wavelength-dependent scattering at discrete angles of both forward and backward directions, I find that the signal can clearly distinguish healthy and ring stage malaria infected red blood cells. The results demonstrate elastic light scattering as a promising non-invasive diagnostic tool.

In a small structure, forces of different physical origins contribute to the free energy. When the configuration changes, the free energy also changes. This free energy change defines a thermodynamic force that drives the configuration change. Insight into the process becomes increasingly valuable as the structures miniaturize. The representative systems studied in this thesis highlights the rich dynamics.

CHAPTER 1

Introduction

Self-assembly in mico/nanoenineering is considered as a technology that can break though the limit of the top-down approach, which may not be applicable in the fabrication of small system if the size is reduced below the width of light that is used. As electronic and optical devices become smaller, the size of parts inside devices needs to be reduced to a few nanometers. The current top-down methods such as lithography may be unable to fabricate atomic scale structures. In addition, as the unique and useful features of nanostructures have been discovered, nanostructures are expected to play an important role in advancing the performance of systems by being incorporated into them. With the increasing needs of nanostructures, self-assembly for efficient mass production with reduced efforts and time has been gathered great attention as a future technology.

Quantum dots are one promising nanostructure that can be applied to photovoltaic, optic, thermoelectric devices or mass storage. Quantum dots sized from tens to hundreds of nanometers have unique electric and optical properties due to dimensional confinement, and they are expected to improve the dimensional and functional qualities of current electronic devices. For example, the array of quantum dots can increase the range of solar wavelengths absorbed by photovoltaic devices, increasing the efficiency

significantly. In addition, the array can be used for optic display panels or logic circuits using each dot as on-off transistors.

There have been a wide range of studies about the fabrication of quantum dots using the self-assembly approach. A famous method is to use the strain energy induced by a lattice mismatch in epitaxial growth to fabricate quantum dots. Upon the lattice mismatch, the surface tends to wrinkle to decrease the strain energy. The wrinkled structure will compete against the increase of surface energy. Through the competition, a dot formation with a certain wavelength is generated. The size of the quantum dots can be controlled by the selection of species, considering parameters such as the size of lattice and the surface free energy of the species. As seen this example, the advantage of self-assembly lies in the capability of the spontaneous mass production of periodic nanostructures by a simple process.

The understanding of the fundamental physics and mechanics happening on the surface are essential in order to develop novel methods using self-assembly for different materials and systems. The understanding of underlying mechanisms will be helpful to control the size and to enhance the regularity of nanostructures.

Ion beam bombardment is a promising process that can self-assemble nanostructures such as ripples and dots on surfaces. The ripple structures under ion beam bombardment were found at the 1960s. The mechanism is explained by the competition between roughening due to curvature-dependent sputtering and thermal smoothening. A number of studies have been performed to figure out the influence of various parameters such as ion beam energy, fluence, incident angles and kinds of materials. Recently, regular dot structures were successfully generated by ion beam bombardment. This dot

formation gathers more interest because of a higher possibility for potential applications than the ripple formation. However, the fundamental mechanism of how regular dots are generated is not as clear as ripple formation, and theoretical studies still continue for a better understanding.

Self-assembled structures are not limited in material science and engineering. In chemical engineering, self-assembled structures such as self-assembled monolayers (SAM) and self-assembled functional molecules are expected to have enormous applications in nano/micro engineering. The size of these molecular structures is rather smaller, ranging from angstroms to tens of nanometers. These functional materials can be used for a drug delivery, nanosensors or changing material properties by being coated on surfaces.

Most functional molecules are operated in combination with NEMS/MEMS devices. When they attach to the surface, they undergo interactions with the surface. That can affect their performance due to external forces transmitted from the surface. Here, interesting questions can be raised; whether artificial molecular machines mimicking biological units in the human body can produce designed work output when they are actually bonded to microdevices; what the influences are on a responding time or strain outputs. The effect of external forces is directly related to the mechanical properties of functional molecules, and the understanding of their mechanical properties is necessary for designing the system and developing new functional molecules.

The understanding of the mechanical properties of nanostructures is useful not only for artificial functional molecules, but also for biomaterials in nature. Recently, there are many efforts to understand changes in the mechanical properties of diseased

cells or tissue in the human body and use it for the development of novel diagnostic tools. Diseased tissues generally lose flexibility and become harder than normal tissues. Because changes of mechanical properties are usually accompanied by changes of optical properties, non-invasive methods using light can be considered to diagnose diseases, especially when the tissues are located near the surface of the skin.

The dissertation will address the mechanics of atoms and molecules in the formulation of self-assembled nanostructures and in the operation of functional molecules. In addition the application of mechanical properties to biomaterials will be addressed. What is the fundamental mechanism in the formation of nanostructures such as quantum dots? How can the mechanical properties of functional molecules be measured and what are they? How can the change of mechanical properties in biomaterials be used in an engineering sense? All of these questions are interesting topics in nanotechnology, and the relation between forces and nanostructures should be addressed for the development of the field in nanoscience and nanoengineering. In this dissertation, each chapter will include a topic of the self-assembled dot structures produced by ion beam bombardment, the mechanical properties of bistable artificial motors and muscles, and light scattering of healthy and malaria-infected red blood cells.

Chapter 2 investigates the mechanisms of the formation of self-assembled nanostructures in ion bombardment. A unique experimental result recently reported will be focused on in the study. It has been known that at off-normal bombardment, the sample should be rotated to generate dot structures. Contrary to other experiments, the recent experiment that motivated our studies observed ordered dot formation at off-

normal bombardment without rotation of the surface. Three different models are suggested in this chapter, and possible mechanisms are discussed.

Chapter 3 includes the mechanics of artificial molecular motors and muscles, which are self-assembled functional molecules. The main interest is what the influences of geometric constrains or mechanical forces are on their performance. The purpose of the study is to investigate how their performance can be changed when they are attached to surfaces for applications. A bistable rotaxane is chosen for the study. It can produce work output by the switching process of an encircling ring between two stable positions. First, a dynamic switching process is studied by molecular dynamics simulations. The study focused on changes of strain and a responding time when the structure is constrained at the ends, assuming they are bonded to surfaces. Next, an artificial molecular muscle, which can be generated by chaining two rotaxanes, is simulated under load conditions. The study focused on the change of strain as increasing the external forces applied at the ends of the structure.

Chapter 4 studied the application of the mechanical property in biomaterials. We paid attention to the observation that the mechanical property of red blood cells changes when they are infected by malaria parasites. Non-invasive diagnostics for malaria may be possible if we detect the corresponding changes by optical devices. For the purpose of the development of non-invasive diagnostics, the patterns of light scattering between healthy and malaria infected red blood cells are compared. If the pattern of scattered light is different, detecting diseases without drawing blood will be possible by shining light sources on human skin.

CHAPTER 2

Ordered Dot Structures in Ion Beam Bombardment

2.1 Previous Experiments

2.1.1 Formation of Ripples

Ripple structures are produced when ion beams are bombarded at off-normal incident angles. It is accepted as universal phenomenon since observations are reported on different materials ranging from semiconductors[1-4], metals[5, 6], graphite[7, 8] to insulators[9]. After ripple structures under ion bombardment were reported, many studies followed to figure out the influence of parameters such as fluence[10-15], temperature[16-18], energy[8, 19-21] and angles[7, 21, 22] on the morphology of ripples. Rusponi et al studied the morphological change of Cu surfaces at low temperature (180 K) as a function of the incident ion beam angle (Figure 2.1)[5]. Habenicht et al found the ripple spacing increases from 40 to 350 nm when Xe^+ ions are bombarded on graphite surfaces with 30° incident angle and fluences of $(3\text{-}5)\times 10^{17}$ cm^{-2}. Ziberi et al reported well-ordered ripples are generated on Si surfaces as increasing ion fluencies while the wavelength of the ripple remains constant (Figure 2.2) [21].

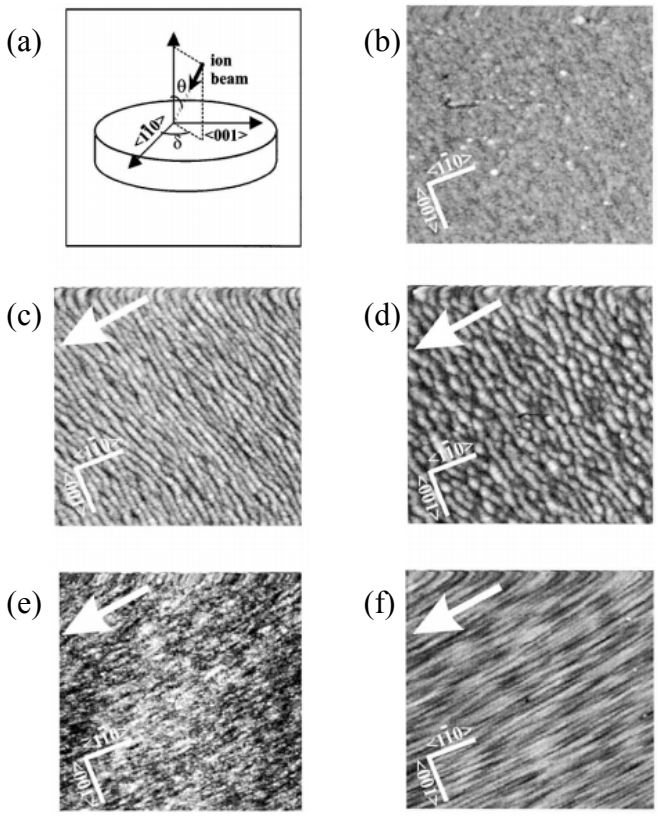

Figure 2.1 STM images of size 400×400 nm^2 of Cu(110) surfaces with the change of the incident angle: (a) the experimental geometry (b) 0˚, (c) 15˚, (d) 55˚, (e) 65˚, (f) 75˚ [5].

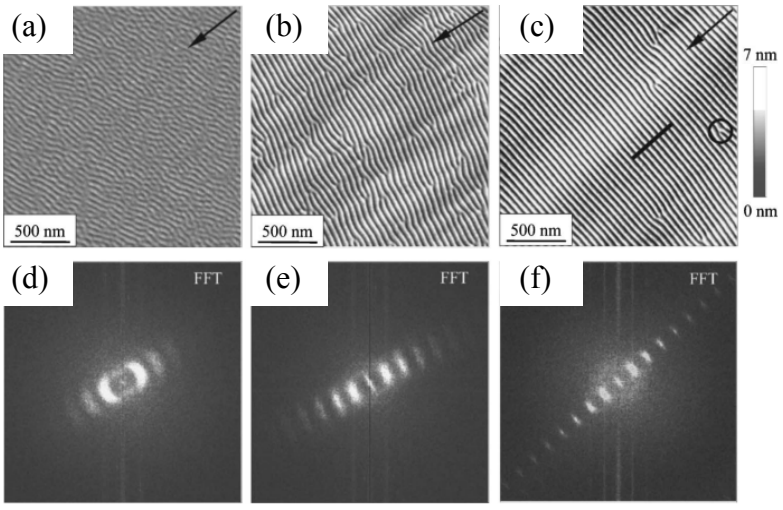

Figure 2.2 AFM images of size 2000×2000 nm^2 of Si bombarded by Kr^+ ions with 1.2 keV and at 15˚ with different fluencies: (a) 3.36×10^{17} cm^{-2} , (b) 2.24×10^{18} cm^{-2} , (c) 1.34×10^{19} cm^{-2} ; the arrows give the ion-beam direction, the circle in (c) shows the defect, and (d)-(f) corresponding Fourier spectrum [21].

2.1.2 Formation of Dots

Late 1990s, a periodic dot structures by ion bombardment reported by Facsko et al for the first time[23]. They obtained crystalline dots of 35 nanometers in diameter on GaSb surfaces by normal bombardment of 0.42keV Ar^+ ions (Figure 2.3). Although dot structures at normal bombardment is expected by a theory about thirty years ago, it is the first time that ordered dots are reported. At the same time, ordered dots at off-normal bombardment with simultaneous rotation of the substrate are also reported on InP surfaces (Figure 2.4)[24]. These two methods, which are normal bombardment and off-normal bombardment with rotation, have been mainly used for fabricating regular dot structures on different semiconductor materials such as InP[25, 26], Si[27], GaSb[28], InSb[29], InAs[26], and Ge[30].

The dots made by these methods have a diameter less than 100 nm and uniform size, and show crystalline structures mostly with a damaged zone at the top (Figure 2.5). In addition, they are highly packed and hexagonally ordered (Figure 2.6).

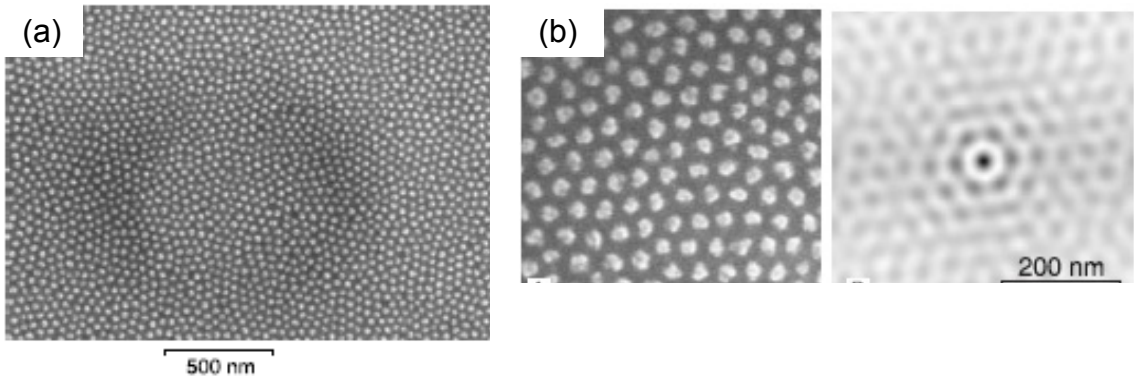

Figure 2.3 (a) Hexagonally ordered dot structures on GaSb surfaces with normal bombardment of ion flux 1×10^{16} cm^{-2} s^{-1} and ion energy 0.42 keV, (b) a SEM image and the corresponding autocorrelation showing the regularity and hexagonal ordering of the dots [23].

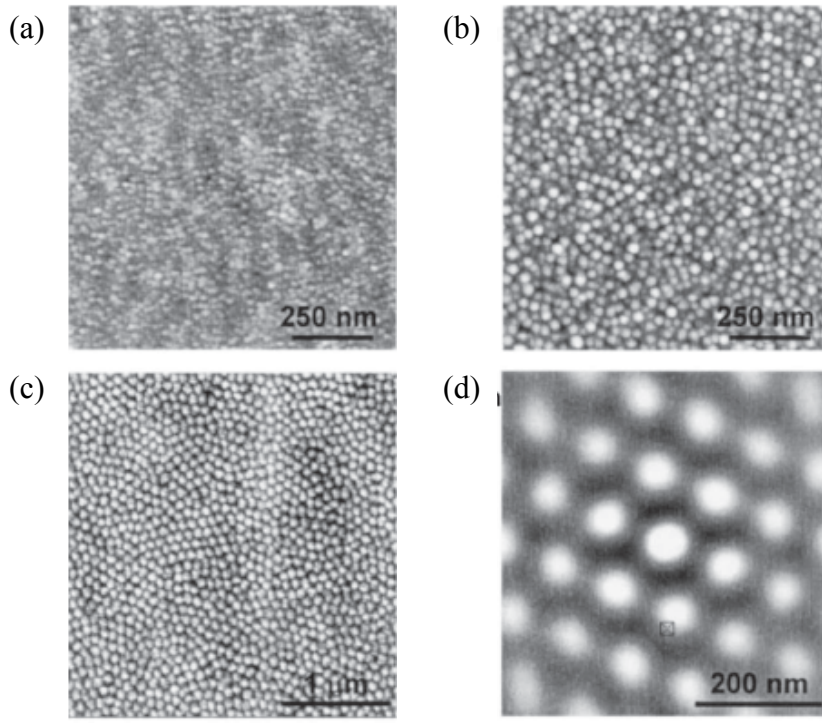

Figure 2.4 AFM images, showing a sequence of the evolution of InP surface with Ar^+ ion energy 0.5 keV and 40˚ incident angle with simultaneous rotation: (a) t=10s, (b) t=40 s, and (c) t=9600 s, and (d) two-dimensional autocorrelation function [24].

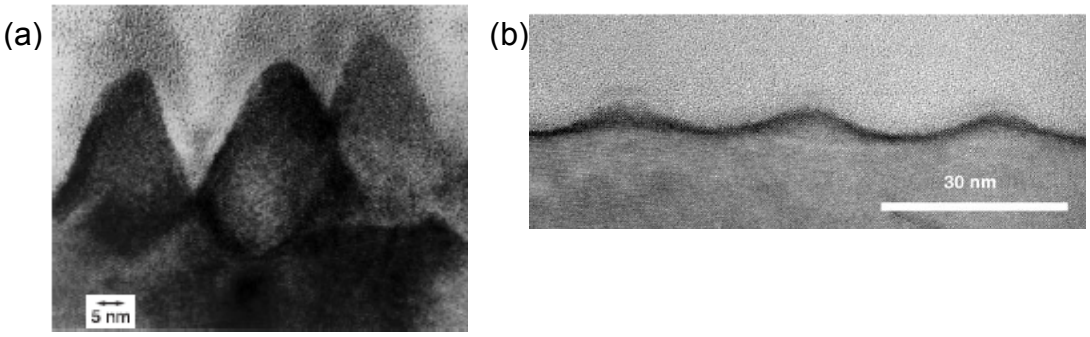

Figure 2.5 (a) A cross-sectional TEM image of the dots on GaSb surfaces produced by Ar^+ ions 0.42keV energy. They are crystalline with an amorphous layer of 2nm, which is the penetration depth of the ions into the material. The height is measured 30nm[23]. (b) A cross-sectional HRTEM image of Si nanodots produced by Ar^+ ions 0.5keV energy and 75˚ with rotation. It shows an amorphous capping layer of 2.5 nm [31].

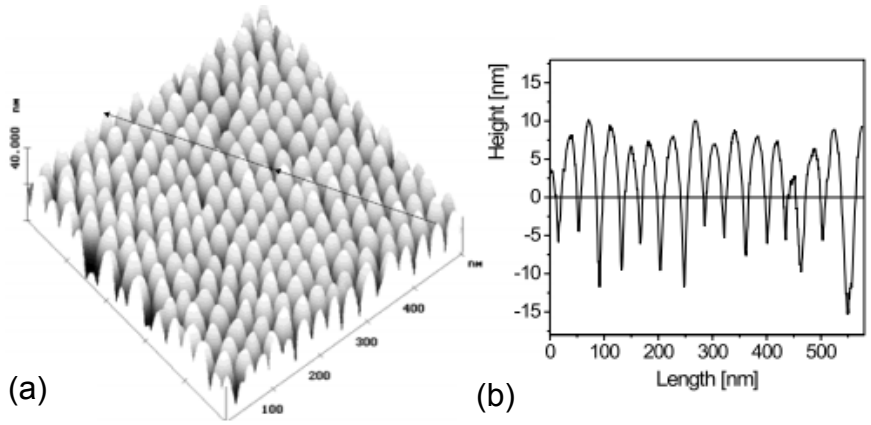

Figure 2.6 (a) An AFM image of dot structures on GaSb surfaces produced by normal bombardment of Ar^+ ions with 0.5keV energy and 3×10^{18} cm^{-2} s^{-1} fluence, and (b) A height profile along the line plotted in the left AFM image [29].

There have been many studies about parameters that influence on the morphology of the surface. Frost et al studied the influence of incident angles and temperature on the size of dots on the InP and GaSb surfaces using both methods of normal bombardment and off-normal bombardment with rotation[25]. Besides, another parameters such as crystal orientation[32], ion type[33] and temperature[34] were studied to increase ordering of dot structures by ion bombardment.

Recently, interesting observations of transformation between ripples and dots were reported. Allmers et al showed dot structures are transformed to ripple structures by varying the incident angle (Figure 2.7) [35]. Zeberi et al reported evolution of the formation from dot structures at normal bombardment to ripple structures at increased angles and to dot structures again with further increase of the angle on Ge surfaces[30]. The same group also demonstrated the evolution of ripples to dots and claimed the local angular distribution of the ion beam can be an additional parameter for the change of morphology on ion-bombarded surfaces (Figure 2.8) [36].

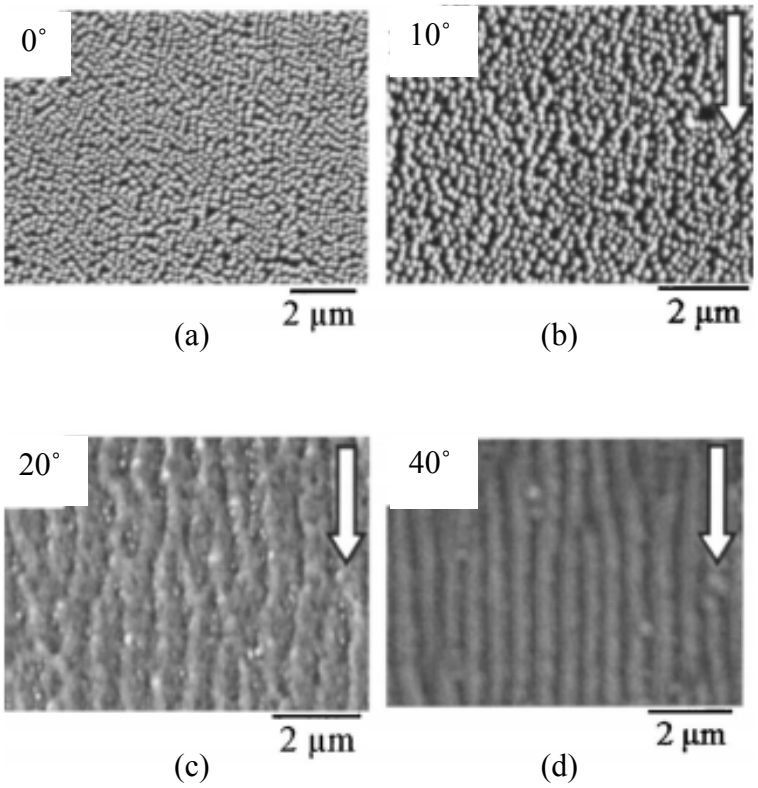

Figure 2.7 SEM images of GaSb surfaces with ion bombardment of Ar^+ ions with 3 keV energy and 1×10^{18} cm^{-2} s^{-1} fluence under different angles. Dot structures transform to ripple structures by varying incident angles (a) 0˚, (b) 10˚, (c) 20˚ and (d) 40˚. The arrows point out the projected direction of the ion beam [35].

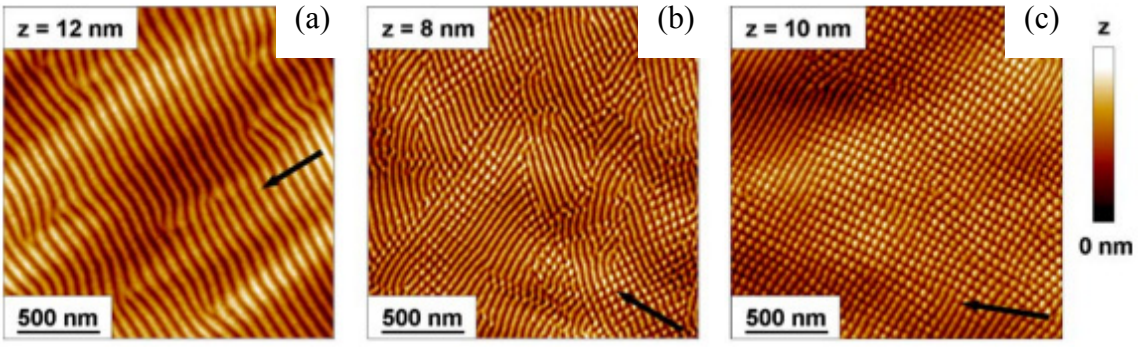

Figure 2.8 AFM images of 2keV Xe ion beam bombarded on Si surfaces with fluence 5.8×10^{18} cm^{-2} at different angles. Ripple structures evolves into dot structures by increasing the incident angles: (a) 5˚, (b) 25˚ and (c) 26˚ [36].

2.1.3 Formation of Dots by Preferential Sputtering

It is known that dot structures can be formulated by normal bombardment or off-normal bombardment with rotation. However, experimental observations of dot structures at off-normal bombardment without rotation have been reported. Maclaren et al showed droplet-like islands form on ripple structures generated at off-normal bombardment (Figure 2.9)[37]. GaAs surfaces are bombarded by 17 keV ions with 25˚ incident angle of the beam. They referred to those islands as 'bubblelike' structures and mentioned those structures appear in most cases of InP and GaAs. At that time, the appearance of these droplets remained as an observation, happening in the ion beam process of the ripple formation at off-normal bombardment.

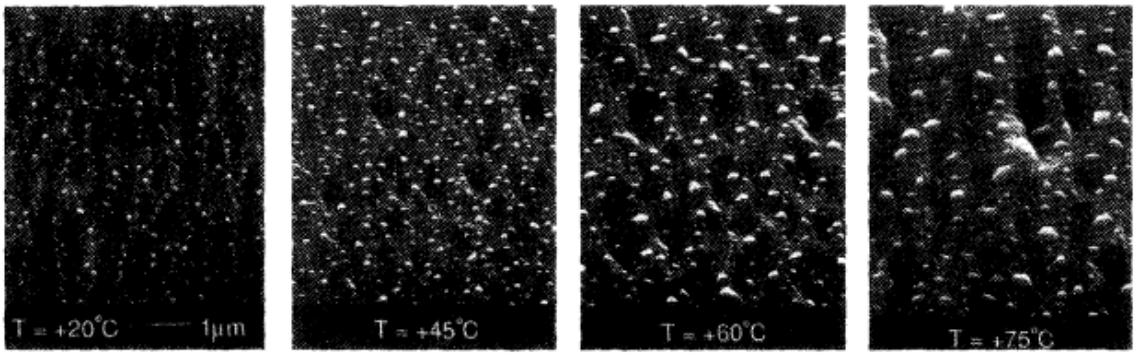

Figure 2.9 SEM images of ripples and droplets on GaAs surfaces produced by 25˚ off-normal bombardment of 17 keV Cs^+ ions [37].

In the early 2000s, experiments focusing on the intentional formation of GaAs droplets were performed by Datta et al[38] with the increase of interest of compound semiconductors such as GaAs and InP, which are important materials for electronic and optical applications. They observed morphological transformation between ripples and droplets as the ion flux changes (Figure 2.10). They mentioned the density of islands is

smaller than what was reported by Facsko et al[23]. The mechanism of the formation of droplets was considered as diffusion and agglomeration of Ga atoms enriched on the surface by preferential sputtering of As.

Preferential sputtering refers to the ratio of species becoming different from the original ratio of compounds due to different sputtering yield. It is mostly observed in GaAs and InP compounds, and nanostructures generated on the surface become enriched by Ga or In atoms after ion sputtering. Dot structures produced by off-normal bombardment on GaAs and InP surfaces imply that preferential sputtering may be used as another method to obtain dot structures by ion bombardment.

Schoendo et al[39] and Rose et al[40] studied the influence of temperature and ion doses on morphological changes on GaAs surfaces at off-normal incident ion bombardment. Two parameters are closely related to diffusion, so we can know diffusion is an important mechanism in the formation of dots due to preferential sputtering.

The characteristics of dots or droplets produced by preferential sputtering are that they are amorphous and composed of only a part of components of the substrate (Figure 2.11). These characteristics are different from the dots reported in the previous studies using normal and off-normal bombardment with rotation, and suggest that the mechanism of the formation of dots depends on diffusion, rather than etching, removal of materials.

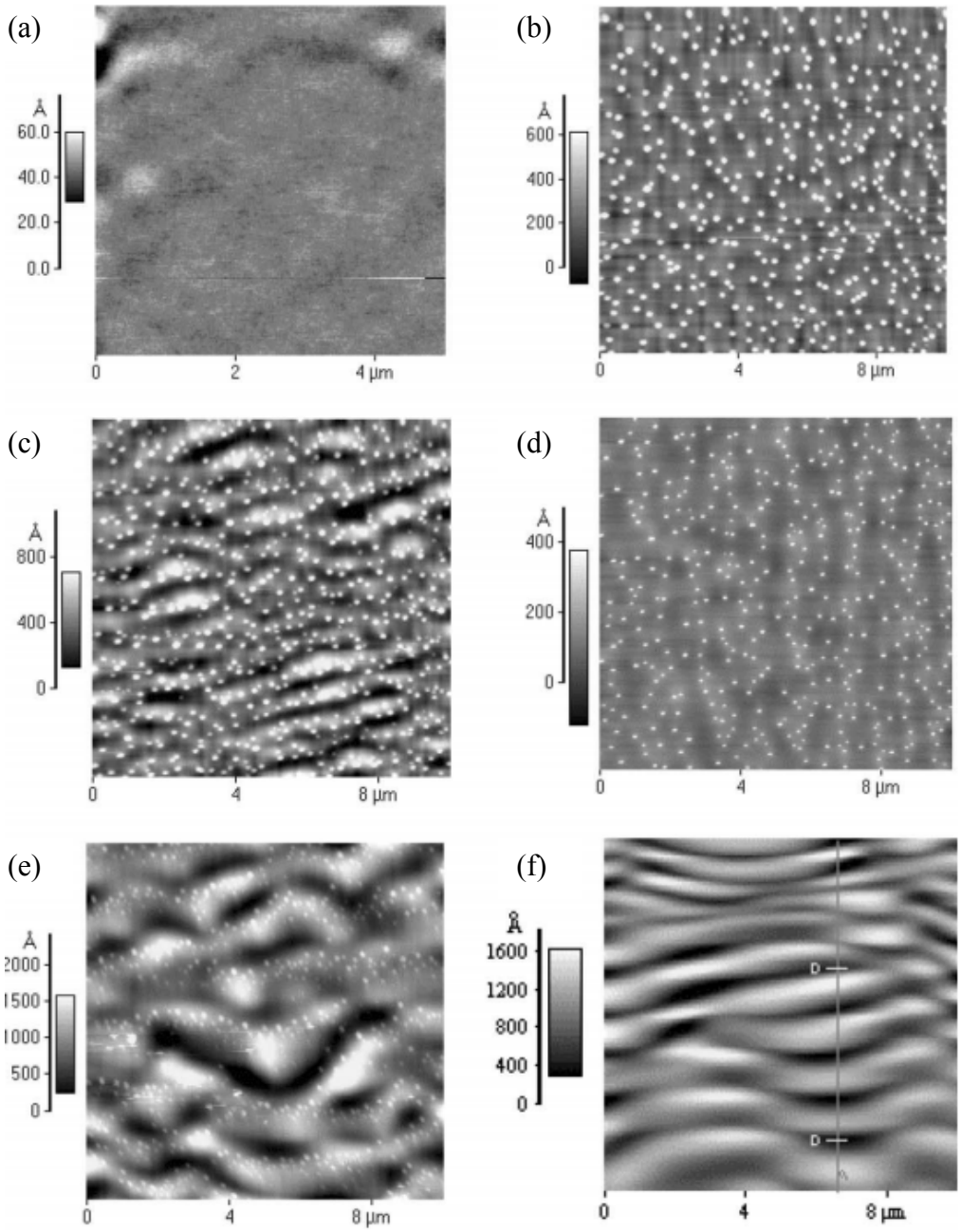

Figure 2.10 AFM images of the evolution of GaAs surfaces bombarded by 60keV Ar at the incident angle of 60˚ according to the doses. Ripples and droplet-like dots are formed together at (c), (d), and (e): (a) 1×10^{17} ions/cm^{-2} (b) 2×10^{17} ions/cm^{-2} (c) 5×10^{17} ions/cm^{-2} (d) 7×10^{17} ions/cm^{-2} (e) 1×10^{18} ions/cm^{-2} (f) 3×10^{18} ions/cm^{-2} [38].

(a)

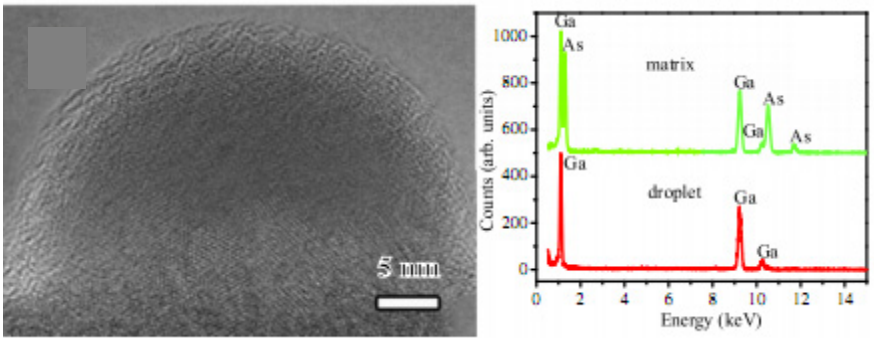

(b)

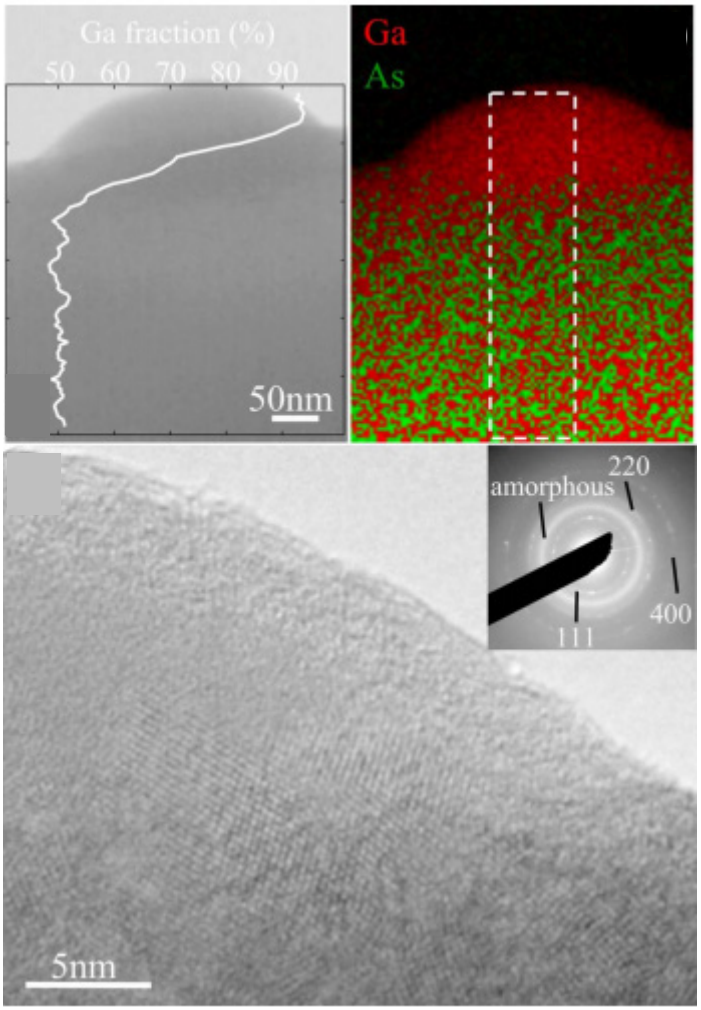

Figure 2.11 (a) A TEM image of cross section of a droplet showing it is amorphous and EDS showing Ga rich component inside the droplet [41], and (b) TEM and EDS map showing amorphous cross section and Ga fraction of a droplet [42].

2.2 Motivation

Recently people began to study how ordered GaAs dots can be produced using preferential sputtering. Lugstein et al showed an array of Ga dots by combining a pre-patterned surface and preferential sputtering on the GaAs substrate (Figure 2.12) [43]. They generated nano-sized holes on the GaAs surface using focused ion beams and let the holes play as seeding points for the growth of Ga dots. Figure 2.12 shows the AFM image of Ga-rich dots whose diameter is 250 nm and height is 55 nm. Similar works have been performed by Shcoendo et al[39] and Wu et al[42].

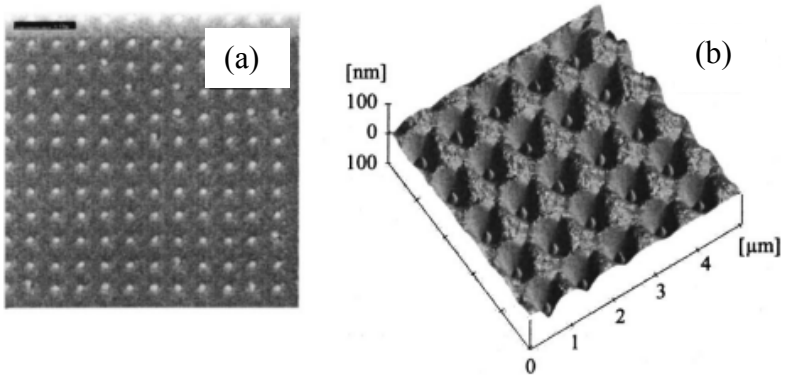

Figure 2.12 (a) A SEM image of the array of Ga dots, and (b) AFM image of an array of Ga dots in the 80 nm deep holes with spacing of 1 μm [43].

Pre-patterning may be a promising approach because the location of dots can be decided. However, when we consider that the advantage of self-assembled nanostructures over lithography is on the cost and time efficiency, it would be better if the pattern is also able to be self-assembled. In this sense, the formation of nanodot chains reported by Tan et al[44] showed the potential of fabricating self-assembled regular dot structures by preferential sputtering. When 1 keV O_2^+ ion beam are bombarded on InP surfaces at 38˚ and 44˚ incident angles of the ion beam, ordered nanodot chains are observed with the dot

size less than 100 nm. The direction of the chains is aligned perpendicular to the incident ion beam.

Qiangmin Wei et al showed hexagonally self-assembled Ga droplets on GaAs surfaces [41]. Figure 2.13 shows Ga droplets are arranged hexagonally and generate chains after 30 minutes of ion bombardment of 5 keV energy, 1×10^{16} cm^{-2} s^{-1} flux and 35˚ incident angle. The droplets are uniform and have an averaged diameter of 50 nm. The direction of the chains of the droplets is perpendicular to the incident beam. As they show, the diameter and wavelength of droplets depend on the incident angle of the ion beam, and the incident angle turns out an important parameter to generate a regular pattern in preferential sputtering. This is an interesting observation since regular dots form at off-normal bombardment without substrate rotation. It is well-known that close to the melting point, Ostwald ripening or coalescence often leads to nonuniform particle sizes during particle growth. Here, this normal physical behavior was hindered under low energy ion bombardment, and highly ordered and uniform hexagonal patterns were induced. Motivated by the experimental results, we will propose models to explain mechanisms of the formation of ordered dots at off-normal bombardment.

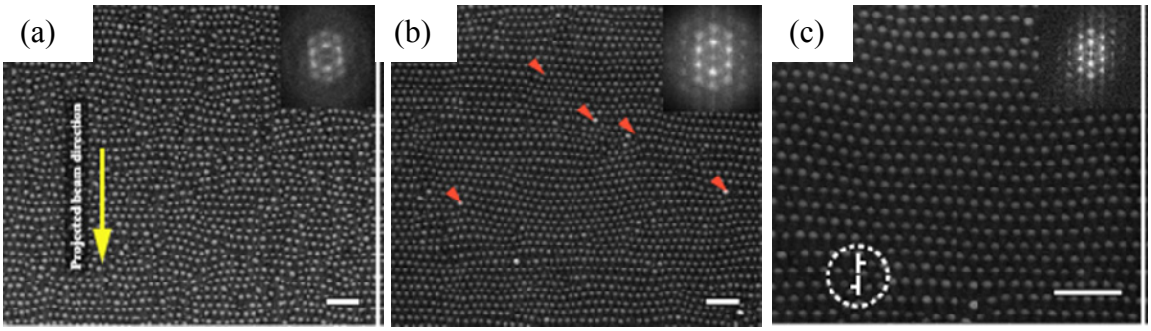

Figure 2.13 SEM images of a sequence of droplet development produced by ion bombardment of 5 keV energy, 1×10^{16} cm^{-2} s^{-1} flux and 35˚ incident angle: (a) 1minute, (b) 20 minutes, and (c) 30 minutes. The scale bar is 500nm [41].

2.3 Previous Modeling Studies

Most ion bombardment models are based on the theory proposed by Bradley and Harper (BH)[45]. The BH equation was derived from Simund's theory[46] that explains the fundamental mechanism of local sputtering induced by energetic interactions of bombarded ions. The BH equation is written as

$$\frac{\partial h}{\partial t} = -v_0 + v_0 '\frac{\partial h}{\partial x} + v_x(\theta)\frac{\partial^2 h}{\partial x^2} + v_y(\theta)\frac{\partial^2 h}{\partial y^2} - B\nabla^4 h, \tag{2.1}$$

where v_0 is constant erosion due to sputtering, $v_x(\theta)$ and $v_y(\theta)$ are incident angle (θ) dependent surface tension, and B is a thermal diffusion coefficient. In a physical sense, they explain the growth of ripples as induced by curvature-dependent sputtering; this explanation is the most accepted theory in the field of ion bombardment. Curvature-dependent sputtering means that the energy distribution by penetrated ions is higher in valleys than in hills (Figure 2.14), which leads to more sputtering in valleys than in hills. The BH theory predicts a ripple wavelength from in ion bombardment as

$$\lambda = 2\pi\left(\frac{2B}{\min\left[v_x, v_y\right]}\right)^{\frac{1}{2}}, \tag{2.2}$$

and the change of the ripple direction at large incident angles from perpendicular to parallel to the incident beam.

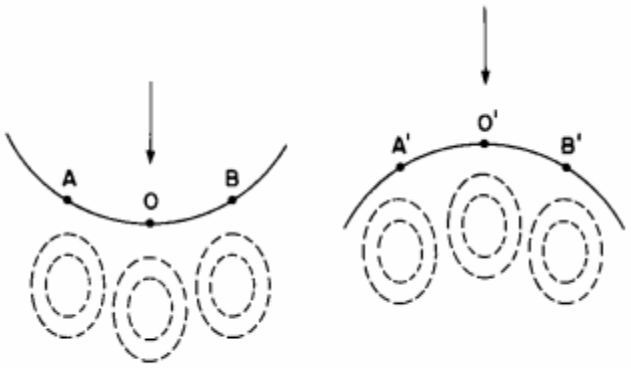

(a) (b)

Figure 2.14 Curvature-dependent sputtering. (a) a valley (b) a hill; The arrows indicate the beam direction. Dashed contours represent equal energy distribution produced by penetrated ions at O, O', A, A', B and B'. The distance to O from each contour at a valley is shorter than O' at a hill. The larger energy concentration at a valley results in more sputtering than a hill, which leads to instability of the surface in ion bombardment [45].

In the 1990s people began to introduce non-linear terms to describe features that the BH theory had not explained. For example, Cuerno et al derived additional nonlinear terms $\nabla^2 h$ to explain the saturation of ripple height[47]. Park et al reported that nonlinear terms determine coarsening or the change of ripple directions after a characteristic time[48]. With the same model, Kahng et al tried to explain a dot formation at normal bombardment[49], but here dots are not regularly arranged. Makeev et al compared theories and experiments systematically in terms of morphological characteristics such as the amplitude, orientation and wavelength of ripples depending on parameters. Kim et al discovered the growing behavior of a surface does not match existing theories and proposed another new nonlinear term $\nabla^2\left(\nabla^2 h\right)$ [50].

Periodic dot structures started to gather interest in late 1990s and are explained by introducing a new term bh with $b<0$, called as a damping term in the report of Facsko et

al[51]. The equation used for the explanation of regular dot formation is called as damped Kuramoto-Sivashinsky (dKS) equation, and it was originally proposed by Paniconi et al[52] for the appearance of hexagonal pattern. This damping term is physically interpreted as redeposition of particles sputtered from the surface. Through parametric studies with the dKS equation, Vogel et al investigated transition from ripples to dots[53].

However, the damping term that is proposed by Facsko conflicts with symmetries of the system. To overcome this shortcoming, Castro et al proposed coupled equations that represent a mobile layer and immobile layer, hinted from modeling of Aste et al[54]. Aste et al applied a theory describing the ripple formation of sand dunes in desert into the ripple formation in ion bombarded surfaces for the first time[55]. The frame is written as

$$\frac{\partial h}{\partial t} = -\Gamma\left(R,h\right)_{ex} + \Gamma\left(R,h\right)_{ad}, \quad \frac{\partial R}{\partial t} = -\nabla \mathbf{J}\left(R,h\right) + \left(1-\phi\right)\Gamma\left(R,h\right)_{ex} - \Gamma\left(R,h\right)_{ad}, \quad (2.3)$$

where h is the height of the immobile layer, R is the thickness of the mobile layer, $\Gamma\left(R,h\right)_{ex}$ and $\Gamma\left(R,h\right)_{ad}$ are the contribution to each layer due to excavation and addition of particles, $\mathbf{J}$ is flux of diffusing particles and ϕ is a rate of sputtered particles into air.

Although the length scale of sand dune in desert and ripples in ion bombardment is different, the same morphology of the ripple formation on surfaces may connect the mechanism of surface instability on both cases. The key concept of this model is introducing two layers, a mobile layer and an immobile layer. Sputtered particles from the immobile layer diffuse through the mobile layer and redeposit on the immobile layer. The advantage of the model is that redeposition can be explained explicitly, compared to the damping term, where physical meanings are implied by approximations. The behavior of morphology based on the two layers is investigated by many other groups[56-59].

In addition to the effort of modeling for various experiment observations, Alkemade et al observed propagation of the ripples on SiO_2 surfaces and introduced a new model explaining viscous flow in a thin layer based on the Navier-Stokes relations[60]. Yewande et al investigated propagation of ripples using Monte Carlo models and expanded their model by including lateral erosion for the scaling analysis of roughness [61, 62].

2.4 Modeling I: Transition from Ripples to Dots

2.4.1 Model

We consider the GaAs substrate subjected to the Ga ion beam bombardment. In our model, two layers are introduced to describe different materials of a GaAs substrate and Ga rich droplets. We define these two layers as an immobile layer and a mobile layer respectively. The immobile layer represents the GaAs substrate, which supplies Ga atoms to the mobile layer. The mobile layer represents Ga atoms, which can move around on the immobile layer. Three main mechanisms are considered in the model: sputtering, redeposition, and mass transportation. Figure 1 shows schematics of the mechanism considered in our model.

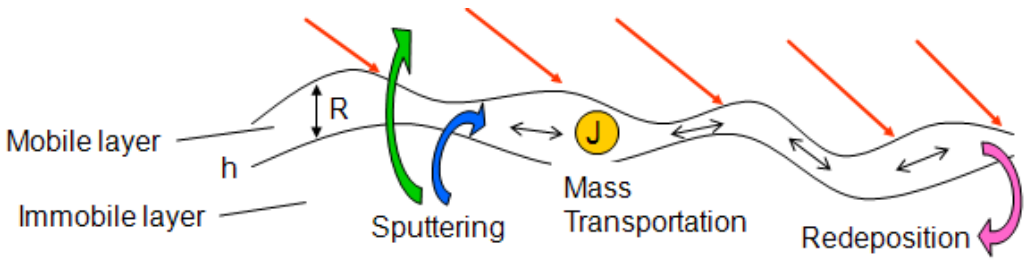

Figure 2.15 Schematic representing main mechanisms in the model.

Sputtering describes the movement of materials from the immobile layer to the mobile layer. Although the Ga atoms in the mobile layer are the remains after the As atoms are sputtered away due to preferential sputtering, it is modeled as they are supplied from the immobile layer. In sputtering, the portion that sputtered into air is also considered, so the rest of it moves into the mobile layer. Redeposition describes the movement of materials from the mobile layer to immobile layer on the other way. Ga atoms moving around in the mobile layer are deposited into the immobile layer when they lose kinetic energy during diffusion. Mass transport describes the movement of materials in the mobile layer. These ideas are modeled as following differential equations,

$$\frac{dh}{dt} = -\Gamma_{sp} + \Gamma_{de}, \tag{2.4}$$

$$\frac{dR}{dt} = (1-\phi)\Gamma_{sp} - \Gamma_{de} - \nabla \cdot \mathbf{J}, \tag{2.5}$$

where, R(r,t) is the thickness of the mobile layer and h(r,t) is the height of the immobile layer. r=(x,y) is a spatial coordinate and t is time. Γ_{sp} is the sputtering rate and Γ_{de} is the redepostion rate.

As the sputtering term represents the movement of materials from the immobile layer to mobile layer, it contributes to lower the height of the immobile layer, so the sputtering rate should be subtracted at Equation (2.4). In a similar way, the redepostion rate should be added because redepostion increases the height of the immobile layer. On the contrary, these should be considered in the opposite way in terms of the mobile layer; the sputtering rate is added and the redeposition rate is subtracted at Equation (2.5). The multiplication of $1-\phi$ in the sputtering rate came from the meaning of ϕ, which represents the portion of sputtered materials into air. $\mathbf{J}$ describes mass flux within the

mobile layer. From the conservation of mass, the thickness of the mobile layer is expressed with the gradient of the mass flux. The negative sign is added because outward flux is defined as positive. The model describes the circulation of materials: sputtered materials into the mobile layer by ion beam are transported on the surface of the immobile layer, and then, redeposited into the immobile layer. How these terms are formulated is described below in detail.

The sputtering rate Γ_{sp} is given by

$$\Gamma_{sp} = \eta\left(1 + b_x \frac{\partial^2 h}{\partial x^2} + b_y \frac{\partial^2 h}{\partial y^2}\right), \tag{2.6}$$

where η is the sputtering rate for a flat surface, and b_x and b_y describes curvature dependent instability since sputtering happens more easily at valleys than at peaks[63]. The reason is that the transferred energy from penetrated ions concentrates more at valleys. Coefficients b_x and b_y can be written by $faY\tau_x / n\eta$ and $faY\tau_y / n\eta$, respectively, where f is the flux, a is the averaged depth of ion deposition, Y is the sputtering yield, τ_x and τ_y are a constant of a function of the incident angle, and n is a number of atoms per unit volume. Thus, the coefficients b_x and b_y depend on the incident angle. At normal bombardment they have the same values, but at off-normal bombardment they become different[63].

The redeposition rate Γ_{de} is given by

$$\Gamma_{de} = R\left(\gamma + d_x \frac{\partial^2 h}{\partial x^2} + d_y \frac{\partial^2 h}{\partial y^2}\right), \tag{2.7}$$

where, γ is a nucleation rate, d_x and d_y are curvature dependent deposition rate. γ^{-1} reflects the time between the nucleation events. The redeposition rate is assumed proportional to the number of mobile atoms per surface area, so it is proportional to the thickness of the mobile layer. d_x and d_y are positive coefficients because deposition to happen is in valleys.

The mass flux **J** is given by

$$\mathbf{J} = -R\nabla\mu - D\nabla R + sR\frac{\nabla h}{1+\alpha\left(\nabla h\right)^2}, \tag{2.8}$$

where, μ is chemical potential, D is temperature dependent diffusion constant, and s and α are constant related to diffusion distance. Note that $\mathbf{J}(x,y)$ at position (*x,y*) refers to the mass flux across the layer thickness at that position.

The first term in Equation (2.8) describes the surface diffusion of mobile atoms on top of the immobile layer. This term tends to make the surface flat to reduce the surface energy. Note that $\nabla\mu$ gives the mass flux for a unit layer thickness, so $R\nabla\mu$ gives the mass flux across the layer thickness. For a surface with surface energy density, κ, and surface curvature, *K*, the chemical potential is given by

$$\mu=\kappa\mathrm{K}, \tag{2.9}$$

The surface curvature relates to the surface height by

$$\mathrm{K} = -\frac{\nabla^2 h}{\left\{1+\left(\nabla h\right)^2\right\}^{\frac{3}{2}}}, \tag{2.10}$$

The second term in Equation (2.8) describes the hydrodynamic mass transport that is related to the gradient of the concentration of the mobile layer. The concentration is the

number of mobile atoms per surface area, so it is proportional to the thickness of the mobile layer. This term also tends to make the surface flat.

The third term in Equation (2.8) describes a mass current moving uphill due to the Ehrlich─Schwoebel barrier, which is in contrast to the first two surface smoothing terms. While diffusing on a terrace, an atom may not jump down to a descending step because of an energy barrier at the end of the terrace. An atom that meets an ascending step tends to stick to that step. The asymmetry in energy barriers favors the attachment of atoms arriving at a step from the lower side and causes an overall uphill mass current. This third term involves the effect of the diffusion length in the following way. The terrace length depends on the surface slope. If the slope is small, the diffusion length of an atom becomes less than the terrace length. In this case only atoms within the diffusion length contribute to a current to uphill[64]. A detailed explanation is in Appendix A.

2.4.2 Stability Analysis

We performed stability analysis to understand what affects the fastest growth wavelength. Putting the expressions of Γ_{sp}, Γ_{de}, and **J** into Equations (2.4) and (2.5), and considering perturbation along the *x* axis gives a set of coupled differential equations,

$$\frac{\partial h}{\partial t} = -\eta\left(1 + b\frac{\partial^2 h}{\partial x^2}\right) + R\left(\gamma + d\frac{\partial^2 h}{\partial x^2}\right), \tag{2.11}$$

$$\frac{\partial R}{\partial t} = (1-\phi)\eta\left(1 + b\frac{\partial^2 h}{\partial x^2}\right) - R\left(\gamma + d\frac{\partial^2 h}{\partial x^2}\right)$$
$$-\kappa\frac{\partial}{\partial x}\left\{R\frac{\partial}{\partial x}\left(\frac{\frac{\partial^2 h}{\partial x^2}}{\left\{1+\left(\frac{\partial h}{\partial x}\right)^2\right\}^{3/2}}\right)\right\} + D\frac{\partial^2 R}{\partial x^2} - s\frac{\partial}{\partial x}\left\{R\frac{\frac{\partial h}{\partial x}}{1+\alpha\left(\frac{\partial h}{\partial x}\right)^2}\right\}. \quad (2.12)$$

A trivial solution of the equations is a flat surface, which is written by

$$R_0 = (1-\phi)\frac{\eta}{\gamma}, \quad h_0 = -\phi\eta t + const.. \quad (2.13)$$

The mobile layer becomes constant when the sputtering rate and the redepostion rate reach equilibrium, and the immobile layer continue to decrease by the portion of sputtered into air and the sputtering rate. However, in general spontaneous roughening occurs due to instability of small perturbation on a surface. We can assume the solution of equations is composed of a flat term and a wavy term,

$$R = R_0 + \hat{R}\exp(iwt + ikx), \quad h = h_0 + \hat{h}\exp(iwt + ikx). \quad (2.14)$$

Substituting Equations (2.13) and (2.14) into Equations (2.11) and (2.14), removing the nonlinear terms, and keeping only the first order terms of $\hat{R}$ and $\hat{h}$, we obtain the following relations,

$$\left\{\left((1-\phi)\frac{\eta}{\gamma}d - b\eta\right)k^2 + i\omega\right\}\hat{h} - \gamma\hat{R} = 0, \quad (2.15)$$

$$\left[\left((1-\phi)\eta b - (1-\phi)\frac{\eta}{\gamma}d - s(1-\phi)\frac{\eta}{\gamma}\right)k^2 + \kappa(1-\phi)\frac{\eta}{\gamma}k^4\right]\hat{h} + \left(i\omega + \gamma + Dk^2\right)\hat{R} = 0. \quad (2.16)$$

The process of linearization is described in detail in Appendix B.

To obtain non-trivial solutions, the determinant of the coefficients should vanish, which gives,

$$\left(iw+\gamma+Dk^2\right)\left\{iw-\left(D_1-(1-\phi)D_2\right)k^2\right\}+\gamma(1-\phi)\left[\left(D_1-D_2-s_1\right)k^2+K_1k^4\right]=0, \quad (2.17)$$

where, $s_1=\eta s/\gamma$, $K_1=\eta K/\gamma$, $D_1=\eta b$, $D_2=\eta d/\gamma$. Instability is related to the imaginary part of ω because negative values of the imaginary part correspond to the wave that increase with time. Figure 2.16(a) shows the graph of the imaginary part of ω that is found from the solution of Equation(2.17). The wavelength corresponding to the largest negative number of the imaginary part is the wave length of the fastest growing wave, which is predicted to 27.3 nm from the relation of $\lambda=2\pi/k$. This prediction is close to the wavelength of 27.7 nm in the numerical simulation shown at Figure 2.16(b).

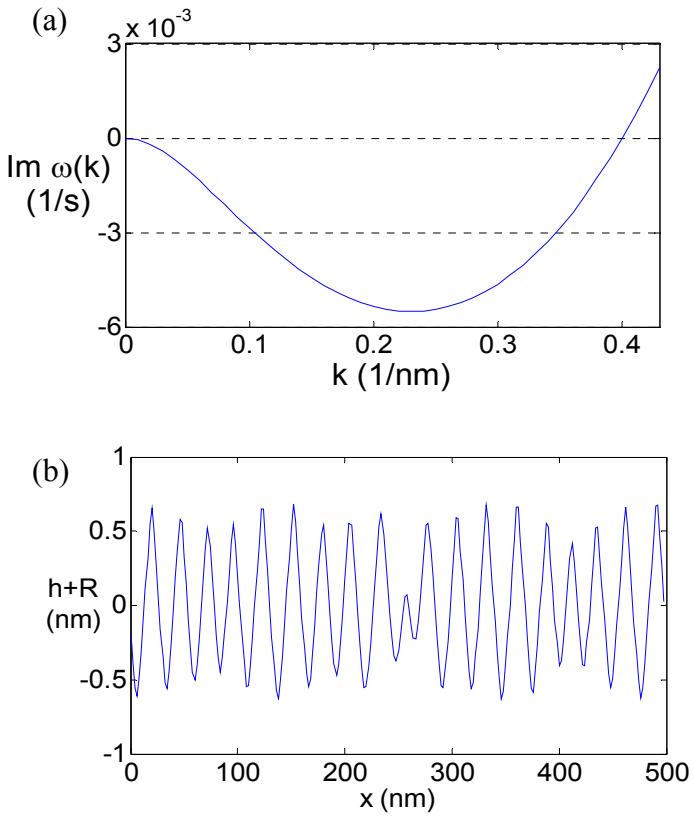

Figure 2.16 (a) Graph of the imaginary part of ω as a function of k. The minimum of the negative imaginary part happens at $k=0.23$, which is $\lambda=27.3$. (b) 2D simulation result at t=6000. The wavelength shown in the graph is about 27.7, which matches the wavelength expected from (a); The parameters are $\eta=0.003$, $b_x=5$, $\gamma=0.005$, $d_x=0.1$, , $\kappa=1$, $D=0.1$, $s=0.4$, $\alpha=10$ and $\phi=0.00001$.

Figure 2.17 shows the behavior of wave growth as a function of time. W represents the root mean square of the height combined both the mobile layer and the immobile layer. At the early time of the simulation, waves grow exponentially fast. Linear behavior is dominant at this region. At a certain time the slope of the curve becomes near zero. At this region the waves are saturated and grow slowly because nonlinear terms begin to affect the growth of the surface height.

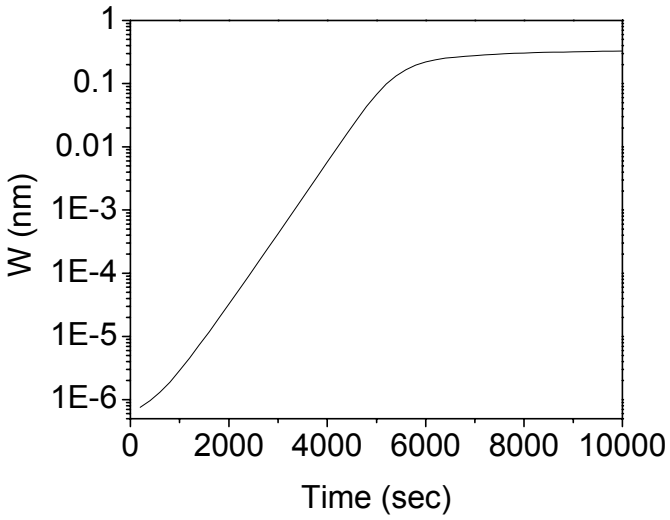

Figure 2.17 Graph of the root mean square of the height (h+R) in the evolution process (log-linear scale).

2.4.3 Numerical Simulations in 3D and Discussion

Full three dimensional calculations of the nonlinear coupled equations of Equations (2.4)-(2.8) were performed using the finite difference method. All simulations were performed in a calculation cell size of 300×300 grids with periodic boundary conditions and random initial conditions. The grid spacing in the *x* and *y* axes was taken

to be $\Delta x = \Delta y = 2$. Euler method was used for the time integration with a time step of 0.1. The simulations started from random initial conditions, i.e. small random height perturbations. To focus on the effect of the incident angle, we fixed other parameters and changed b_y only. The parameters used in our simulations were taken to be $\eta = 0.03$, $b_x = 0.01$, $\gamma = 0.03$, $d_x = 0.1$, $d_y = 0.1$, $\kappa = 3$, $D = 0.5$, $s = 0.4$, and $\alpha = 30$. For normal bombardment, b_y is the same as b_x due to symmetry. The value of b_y is larger than b_x for off-normal bombardment, and the difference increases with the angle according to the □ 넔□ 伀J倀ɳ 儀J愀□ 彀□ □鶇伀J倀ɳ 儀J愀□ □ □ 谕□ 넔□ 伀J倀ɳ 儀J愀□ □ □鶇伀J倀 respectively. Representative results are given in Figures 2.18-2.20.

Figure 2.18 shows the sequence of morphological evolution during normal bombardment. After the evolution starts, short and small ripples quickly agglomerate. Fast growing spots emerge at locations where the hills of ripples meet. A random distribution of small dots become evident at about *t*=2000. The system and bombarding conditions are isotropic so the pattern has no particular preferred orientations. The dots grow exponentially fast at the beginning, but the rate slows down quickly after *t*=4000. The dots do not change much after *t*=5000, suggesting a saturation of the amplitude. There is no sign of any alignment of dots in the simulations.

Figure 2.19 shows the sequence of morphological evolution during off-normal bombardment. Not much difference is observable compared to normal bombardment during the very early stage evolution up to *t*=500. The ripples continue to grow in both size and height over time, and start to demonstrate an orientation preference along the *x* axis at about *t*=1000. Some locations grow faster, where dots start to emerge. At *t*=2000 some dots become very visible. The ripples grow simultaneously so at *t*=3000 the pattern

looks like a mixture of dots connected by ripples. At t=4000 we can observe that the ripples start to break into smaller dots. At t=5000, the dots appear to overall line up in the x axis, thought lots of miss-alignment exists. The size of dots is smaller compared to the size of ripples during normal bombardment.

Figure 2.20 shows the evolution during off-normal bombardment with an incident angle larger than that in Figure 2.19. At t=500, dots emerge at very early stage by the aggregation of small peaks of the random initial perturbations. Ripples start to appear at t=1000 and becomes visible at t=2000. Note that the ripples in Figure 2.20 are more evident than those in Figure 2.19. At t=3000, the ripples begin to break into dots, which appear to locate at the peaks of the ripples. The formation of a dot pattern become evident after t=4000. These dots line up along the x axis, and the alignment is much better than that in Figure 2.19. This is because clear ripples are generated in Figure 2.20. The comparison between Figures 2.19 and 2.20 suggests that larger incident angles cause well developed parallel ripples, and they evolve into better aligned dots in the final stage.

Our simulations have revealed an interesting transition during the dot formation process. When the incident angle is larger, curvature dependent instability becomes more anisotropic. This anisotropy promotes the development of parallel ripples whose wavelength is characterized by the fast growth wavelength. The ripples become saturated when the nonlinear terms become significant. The saturated ripples further experience instability in the longitudinal direction, and break into small dots. This transition appears to play an important role in determining the alignment of dots and their alignment directions. The simulation results have demonstrated the same tendency observed in experiments: At normal bombardment randomly distributed dots are observed. As the

incident angle is increased, ordering of the dots increases and their chains are formed perpendicular to the incident beam direction.

2.4.4 Conclusions

In summary, the evolution of surface morphology during ion beam bombardment is modeled. In this model we consider a two-layer setup, which represent the substrate and diffusion of mobile atoms. Consideration of sputtering, re-deposition and mass transport leads to a set of coupled nonlinear differential equations that are solved numerically with the finite difference method. The effect of the incident angle is considered implicitly by anisotropy of b_x and b_y. The three dimensional simulations reveal rich dynamics, and show that ordered dots can be obtained by controlling the incident angle of the ion beam. The off-normal bombardment produces ripples by anisotropic curvature-dependent instability at the early stage. After the growth of the ripples is saturated, the instability along the ripples provokes the emergence of dots at the later stage. The dots are aligned since they evolve from ripples. Due to the fundamental nature of competing kinetics, the results may be useful to other materials systems as well.

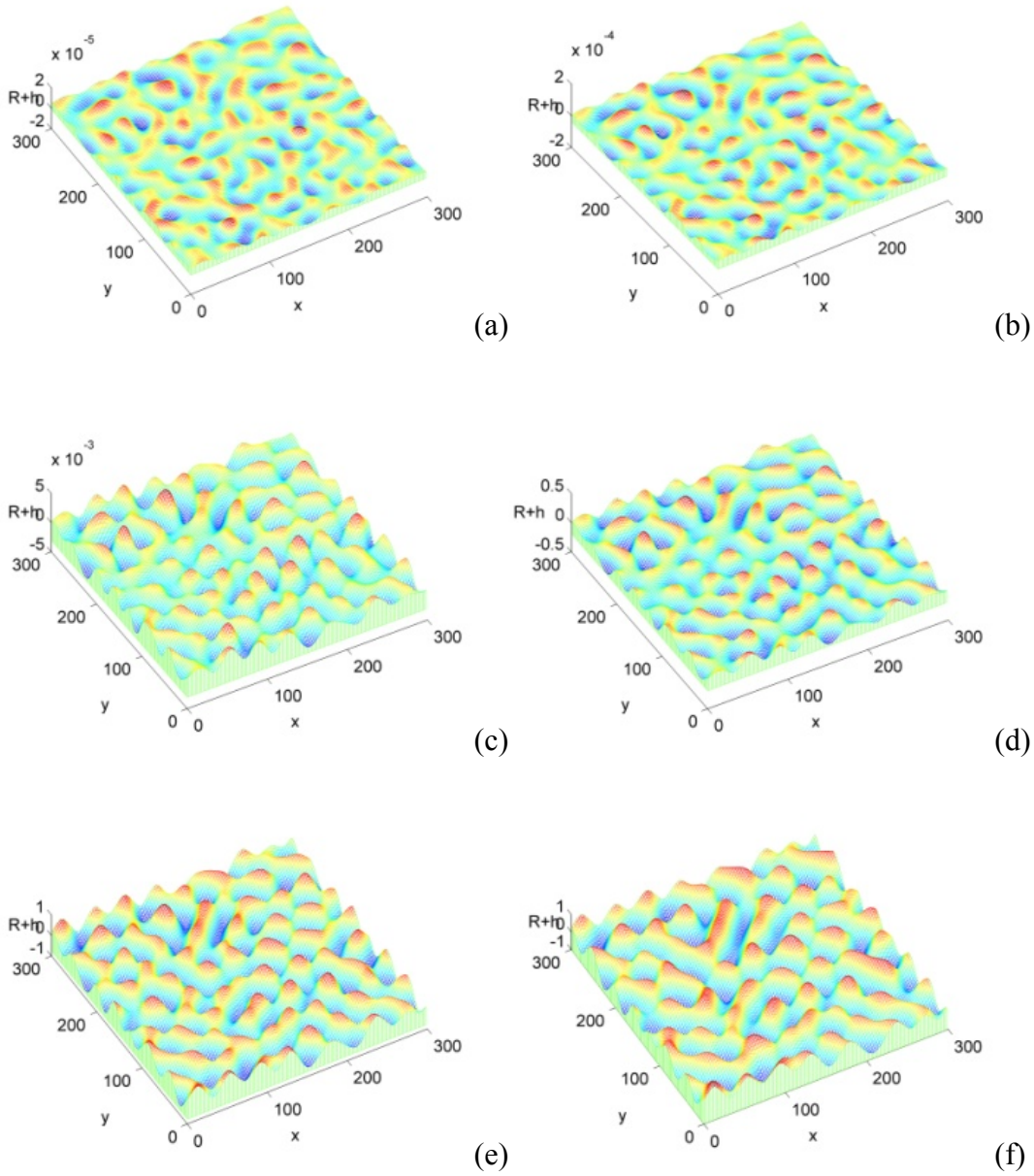

Figure 2.18 Evolution sequence under normal bombardment: (a) t=500, (b) t=1000, (c) t=2000, (d) t=3000, (e) t=4000, and (f) t=5000.

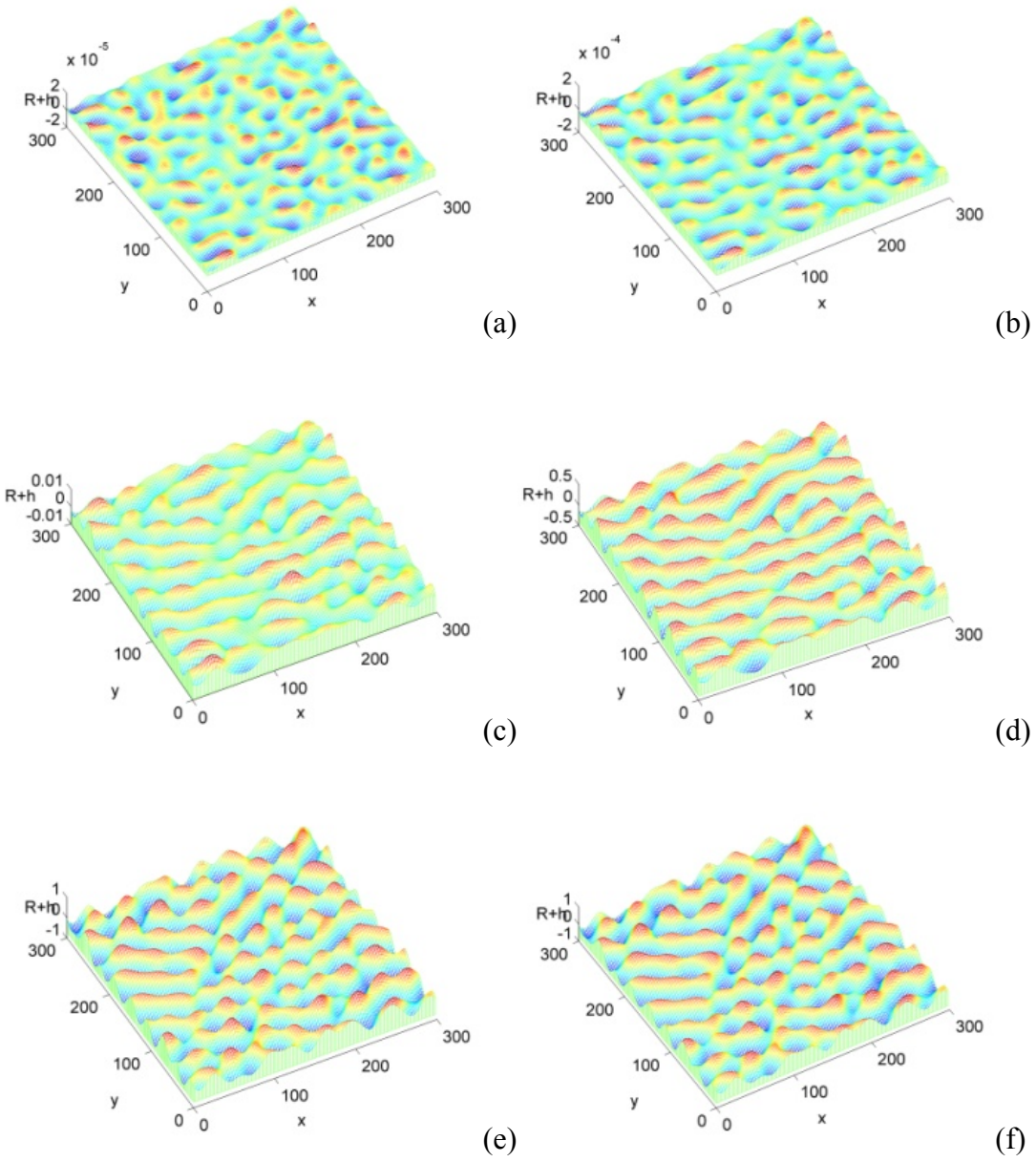

Figure 2.19 Evolution sequence of off-normal bombardment at a small incident angle: (a) t=500, (b) t=1000, (c) t=2000, (d) t=3000, (e) t=4000, and (f) t=5000.

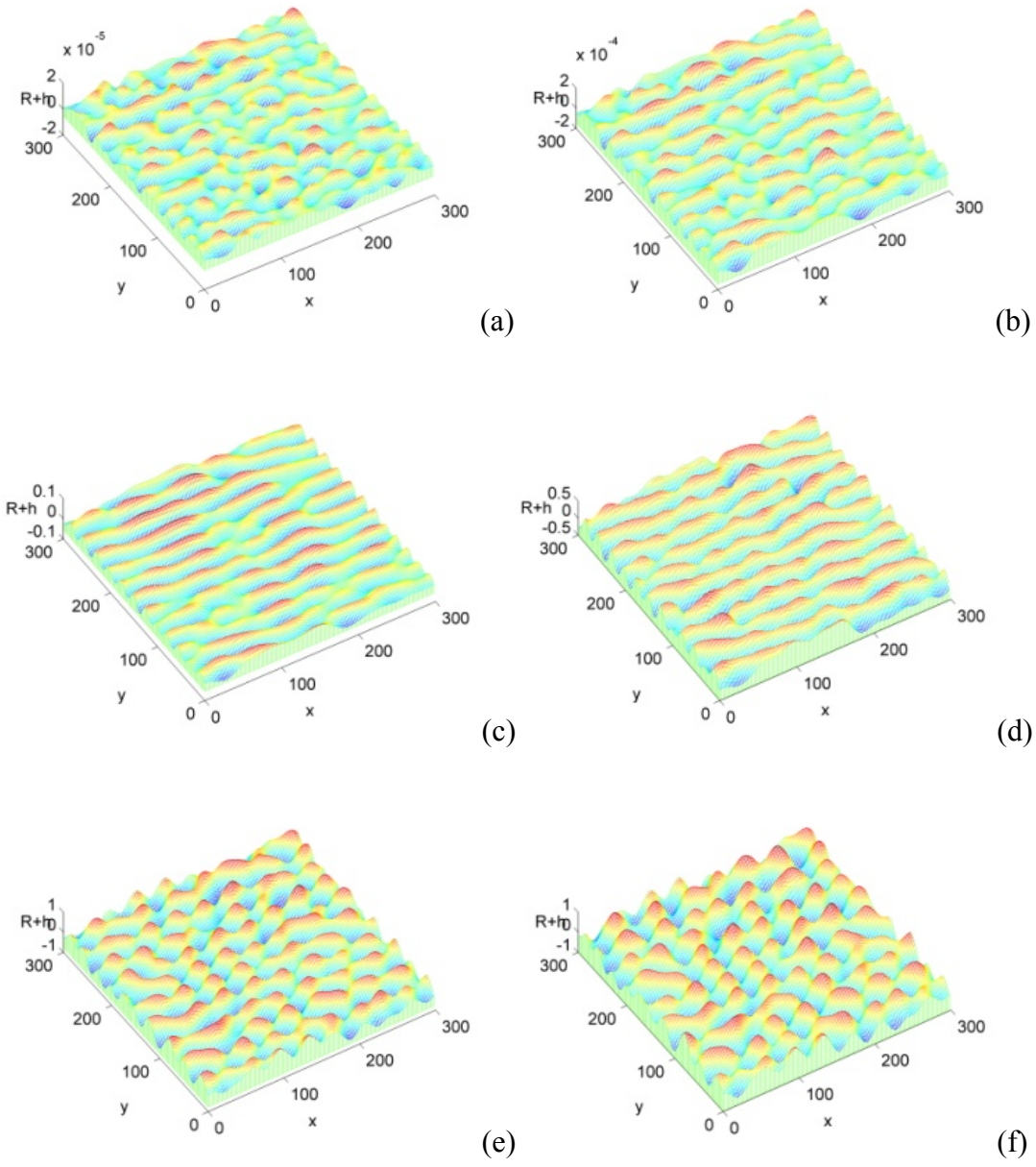

Figure 2.20 Evolution sequence of off-normal bombardment at a large incident angle: (a) t=500, (b) t=1000, (c) t=2000, (d) t=3000, (e) t=4000, and (f) t=5000.

2.5 Modeling II: Self-Organized Chains of Dots by Shadow Effect

The reason for using the two-layer model is that it can express the process of redeposition explicitly. The two-layer model, however, is complicated by having two coupled equations. In this section, a one equation model is described. In addition, a new term describing the shadow effect is considered.

2.5.1 Model

We represent the surface with a spatially continuous and time dependent function, $h(x, y, t)$, where x, y are axes parallel to the substrate surface and t is time. Starting from a flat surface, morphological changes of the surface and the process of evolution are captured by the change of *h* in the z direction. We consider concurrent surface kinetics including diffusion, redeposition and sputtering. The time evolution of the surface is given by

$$\frac{\partial h}{\partial t} = -\nabla \cdot \mathbf{J} - \rho h + \beta(\nabla h)^2 . \tag{2.18}$$

The first term represents mass conservation, where $\mathbf{J}$ is the diffusion flux of Ga on the surface. The second term, ρh, accounts for redeposition of sputtered atoms, which settle on the surface after traveling in air[51]. The coefficient ρ describes the rate of redeposition. For a fixed coordinate, this term should be formulated as $-\rho(h - \bar{h})$, where $\bar{h}$ is the spatial average of the surface height[51] . This term describes a phenomenon that atoms above the average height tend to be sputtered while atoms redeposit below the average height. Here if we use a moving coordinate such that the zero height coincides with the surface average, the $\bar{h}$ term can be dropped. We focus on morphological

changes in our study, thus changes in the average height due to sputtering or redeposition is less significant. The third term $\beta(\nabla h)^2$ describes the tilt-dependent sputtering yield, which affects the saturation of growth[48]. The sputtering rate β is dependent on the flux and the energy of the beam. Using a flat surface ($\nabla h = 0$) as a reference, the sputtering yield decreases with the slope; thus, those regions with larger slopes tend to increase heights relative to flat regions.

The diffusion flux $\mathbf{J}$ can cause either surface roughening or smoothing. The roughening mechanism in ion beam bombardment is usually modeled by Bradley and Harper (BH) theory. It postulates that the surface instability is caused by a curvature-dependent dispersion of the energy, which happens by the removal of atoms on the surface through etching or a similar mechanism. In this case, materials of induced nanostructures such as ripples or islands are same as those of the substrate. The islands in our experiment, however, are composed of a different material, suggesting etching is not the process of roughening. We consider diffusion causes roughening of the surface. In the experiment, Ga atoms are enriched on the surface due to preferential sputtering of As as well as deposition of the Ga ions from the Ga beam. Enriched Ga atoms are nucleated and grow as islands while they diffuse.

The nanostructures formulated by diffusion behave like droplets or bubbles[42, 43]. In addition, they are amorphous and have a hemi-spherical shape. They are different from the nanostructures shown in experiments of ion beam bombardment, which are partially amorphous and cone-shaped[29, 65]. Droplets formed by diffusion are usually observed at relatively high energies of an ion beam over 10 keV. Higher energies promote preferential sputtering and high mobility of diffusing atoms. The ripples induced

by diffusion are hardly observed because highly mobile atoms tend to form in droplets rather than longish ripples. Ripple structures are usually generated by sputtering, and the mechanism of the ripple formation can be explained by the BH model [1, 10, 19, 22].

The islands, however, can be grown by either diffusion or sputtering. Both experiments of Reference [65] and Reference [38] showed dots, but the former showed more highly packed dots than the latter, which means the dots in Reference [65] are generated by sputtering and can be modeled on the base of the BH instability. The Reference [38] showed both ripples and islands at a specific dose of the ion beam, and small islands are formed on top of the relatively large ripples. The ripples appeared in reference [38] are generated by sputtering; on the other hand, the formation of the dots can be explained by agglomeration induced by diffusion.

We describe the growth of islands as an uphill flow along the slope, which is $\alpha\nabla h$, where α is the growth rate that can be affected by the diffusing velocity of atoms and sputtering yield. Although atoms actually do not move upward along slopes in experiments, this term properly captures the instability that is described by the growth of islands due to the supply of atoms from the perimeter of islands. This term is isotropic because atoms are supplied in all directions. And, because the supply of atoms is not related to the angle of incident beams, ripples do not appear in our model even at off-normal bombardment, which is consistent with experimental observations.

Smoothening due to surface energy is considered in the following way. The chemical potential of atoms on the surface can be expressed by $\mu = K\gamma\Omega$ [66], where K is the surface curvature, γ is the surface energy per unit area, and Ω is the atomic volume. The curvature can be expressed by the second derivative of the surface height. With a

small slope assumption, we have $K = -\nabla^2 h$. The atoms on the surface tend to move to regions with a lower chemical potential, giving a diffusion flux of $-D_T \nabla \mu$, where D_T is the diffusion coefficient. Denoting $\lambda = D_T \gamma \Omega$, we get a diffusion flux of $\lambda \nabla(\nabla^2 h)$.

Next, we consider the shadow effect. In the shadow zone, where the ion beam is blocked by islands during off-normal bombardment, sputtering becomes weakened. The stronger sputtering on the top of islands ($\nabla^2 h < 0$) drives mass diffusion towards shadowed valleys ($\nabla^2 h > 0$). The diffusing direction follows the gradient, which is $\nabla(\nabla^2 h)$. We represent the shadow effect by adding a new term, which is similar to the term for surface energy, but modified in two aspects. First, the shadow effect happens only along the direction of the incident beam. We assume that the beam is within the *x*-*z* plane. Then, the shadow effect only happens along the *x* direction. Second, a higher surface gets more sputtering, and deeper in the valley gets less sputtering. To the first order approximation, we assume that the smoothening flux is proportional to *h*. Following the form of surface energy, the corresponding mass flux can be written by $\eta \left\{ \mathbf{i} \cdot h \nabla(\nabla^2 h) \right\} \mathbf{i}$, where $\mathbf{i}$ is the unit vector in the *x* direction, and η is a coefficient. Note that the *h* before the gradient operator makes this term nonlinear, which becomes important only after the surface has developed sufficient roughness. Otherwise, this term would affect the early stage of simulations, whose anisotropic smoothening effect generates ripples, which are not observed in experiment. The magnitude of η will depend on the incident angle, θ, between the incident beam and the *z* axis.

Consideration of all the contributions gives the following diffusion flux,

$$\mathbf{J} = \alpha \nabla h + \lambda \nabla(\nabla^2 h) + \eta \left\{ \mathbf{i} \cdot h \nabla(\nabla^2 h) \right\} \mathbf{i} \ . \qquad (2.19)$$

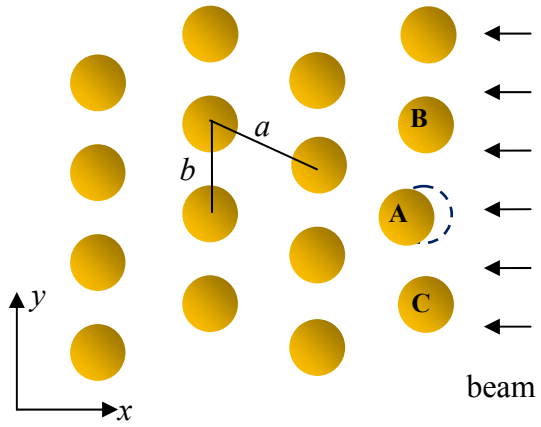

Figure 2.21 Schematic of a hexagonal pattern of dots lined up along the *y* axis, perpendicular to the direction of the incident beam. Dot A would be partially shadowed by B and C if it shifts to the left, when mass accumulation at its front would bring it back to line up with B and C. Anisotropic smoothing causes the different distance between dots, i.e. $a>b$.

Now we discuss how the shadow effect causes dots to line-up into chains. Consider a hexagonal pattern of dots as shown in Figure 2.21. These dots line up into chains along the *y* axis. Dot A would be partially shadowed by B and C if it shifts to the left, when mass accumulation at its front would bring it back to line up with B and C. Similarly, dot A would be exposed to more sputtering if it shifts to the right, and would gradually move back to be in-line with B and C. The anisotropic smoothing given by the third term in Equation (2.19) causes the wavelength in the *x* direction to be larger than that in the *y* direction. As a result, the distance between dots is not isotropic, i.e. $a>b$. This behavior is consistent with experimental observations[41].

2.5.2 Numerical Simulations

To facilitate numerical simulations, Equations (2.18) and (2.19) can be expressed into dimensionless forms with *h, x, y* normalized by a length scale l_0, and *t* normalized by a time scale t_0. The parameters ρ, β, α, λ, η are normalized by $1/t_0$, l_0/t_0, l_0^2/t_0, l_0^4/t_0, l_0^3/t_0, respectively. The dimensionless equations appear the same as Equations (2.18) and (2.19), except that now the symbols represent the corresponding normalized values, such as *h* represents h/l_0. Below we always refer to the normalized quantities.

The finite difference method was used for numerical simulations with its dimensionless form. The calculation domain size was taken to be 200×200. Periodic boundary condition was applied. The grid spacing and time step were taken to be $\Delta x=\Delta y=0.5$ and $\Delta t=0.01$. The initial surface morphology was constructed by adding to a flat surface with a small random perturbation with magnitudes between 0 and 10^{-5}.

Representative results are shown in Figure 2.22 and 2.23. The following normalized parameters were chosen: $\rho=0.24$, $\beta=1$, $\alpha=1$, $\lambda=1$ [67]. Figure 2.22 shows a sequence of evolution for $\eta=1.0$ from t=0 to t=10000. Figure 2.22 (a) shows the initial substrate surface at t=0. After a short time of bombardment, small peaks quickly emerge and form a wavy chain pattern, as shown in Figure 2.22 (b). Linear terms are dominant during the early stage of evolution. The nonlinear term representing the shadow effect does not reflect itself significantly in the result. Dots start to emerge and grow quickly after t=1000, as shown in Figure 2.22 (c) for t=1400. As of now, the dots are randomly distributed without showing any particular order. The growth of dot height slows down after t=2000, when the nonlinear term starts to affect growth. Figure 2.22 (d) and Figure 2.22 (e) show that the dots start to line up and form short chains. Overall,

these short chains appear to orientate along the y axis, though the orientation of a single chain is less definite. During this stage the dominating behavior is the change of the location of dots, while their heights remain almost constant. Overtime the chains become more ordered. Figure 2.22 (f) shows that at t=10000 the chains are clearly aligned along the y axis, which is perpendicular to the incident beam direction. The dots form a hexagonal pattern and their sizes are uniform. These simulation results are consistent with experimental observations[41].

Figure 2.23 shows simulation results at t=10000 for different values of η, revealing how the strength of the shadow effect affects patterns. Figure 2.23(a) shows that no chain is formed when there is no shadow effect, or $\eta=0$. The dots simply form a hexagonal pattern. Figure 2.23(b) shows that with $\eta=0.5$, chains appear to form but are not perfectly aligned. The comparison with Figure 2.22 (f) clearly shows that a stronger shadow effect leads to well aligned chains perpendicular to the beam direction.

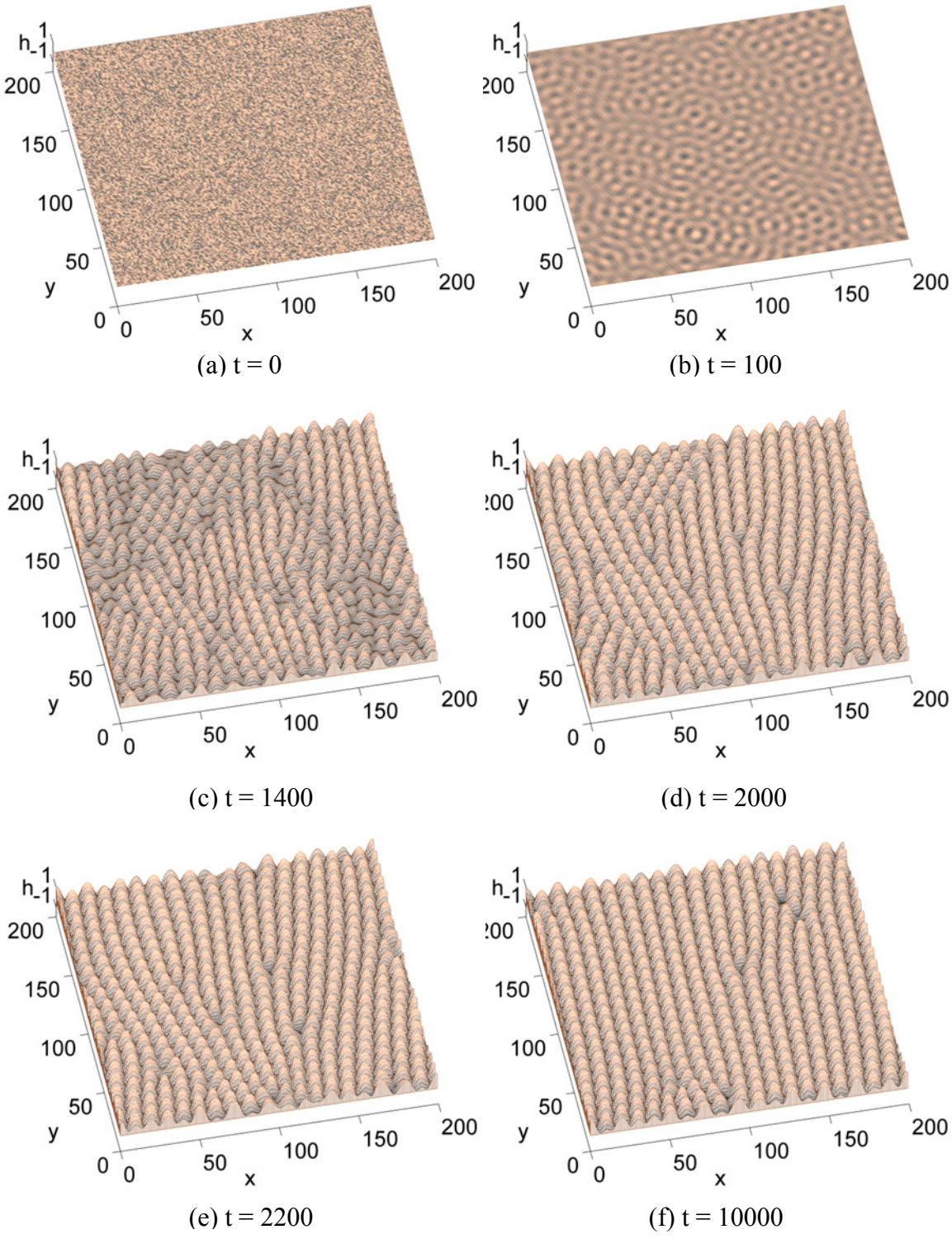

(a) t = 0 (b) t = 100

(c) t = 1400 (d) t = 2000

(e) t = 2200 (f) t = 10000

Figure 2.22 Evolution sequence showing self-assembled dots emerge, line up and form chains.

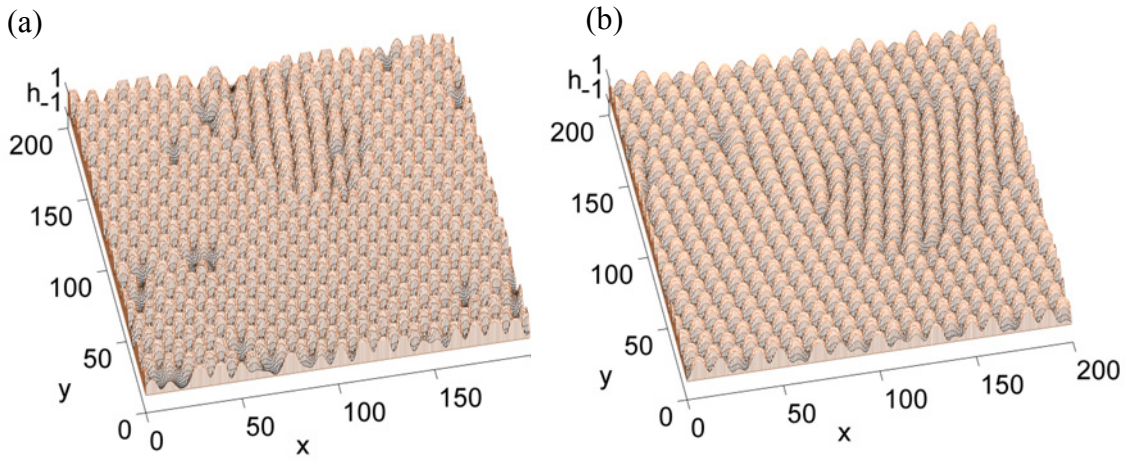

Figure 2.23 Simulation results at t=10000 for different values of η, revealing how the strength of the shadow effect affects patterns: (a) no shadow effect (η=0), and (b) weak shadow effect (η=0.5).

2.5.3 Conclusions

Our model and simulations have revealed how self-assembled dots emerge, line up and form chains during ion beam bombardment. In the simulations, after the height of the dots is saturated, they spontaneously line up due to the diffusion induced by weakened sputtering in the shadow zone. The intensity of the shadow effect is considered by controlling η, which is a function of the incident angle. These simulations show the importance of the shadow effect, which happens only during off-normal bombardment and leads to chains perpendicular to the incident beam direction. In addition, it is shown that the chains of dots are not formed by an initial ripple generation along y followed by a subsequent process to break up these ripples into dots. Instead, the dots emerge at the early state of evolution, and then gradually rearrange to form chains.

2.6 Modeling III: A Hexagonal Formation of Nanodroplets

In the previous simulations, we have shown the chains can be formed by the shadow effect. However, the morphology of the simulation results is somewhat different from what has been shown in the motivated experiment. For example, islands are highly packed in the simulations although they are separated with a certain distance in the experiment. And the islands in the simulations have an oval shape rather than a hemi-spherical shape. This is because the surface was modeled as a smooth curve, resulting in difficulty distinguishing the boundary between the islands and the substrate. Below, we suggest an improved model, which shows morphologies more consistent with experiment, by considering wetting energy.

2.6.1 Model

We represent the substrate surface with a spatially continuous and time dependent function, $h(x, y, t)$, where x, y are axes parallel to the substrate surface and t is time. Starting from an initially flat surface, the formation of surface morphology and its evolution is captured by the change of *h* in the z direction. We consider concurrent surface kinetics including diffusion, sputtering and the supply of atoms from preferential sputtering. The time evolution of the surface is given by

$$\frac{\partial h}{\partial t} = -\nabla \cdot \mathbf{J} - \beta(\nabla h)^2 + \eta \quad . \tag{2.20}$$

The first term represents mass conservation, where $\mathbf{J}$ is the diffusion flux of Ga on the surface.

The second term, $\beta(\nabla h)^2$, describes the tilt-dependent sputtering. We assume that the sputtering of Ga atoms happens more likely from islands ($\nabla h \neq 0$) than from the substrate ($\nabla h = 0$). At the substrate surface, Ga atoms are supplied due to preferential sputtering of As. On the other hands, at the Ga rich islands, sputtering of Ga happens more actively because no preferential sputtering occurs. Although sputtering may happen directionally at off-normal bombardment, we assume that sputtering is isotropic because islands in the experiment behave like droplets. The atoms in the island are highly mobile, so the island tends to quickly recover and keep the hemi-spherical shape although atoms are removed in a certain direction by sputtering.

The third term represents the supply of Ga atoms. The Ga atoms are supplied from the substrate due to preferential sputtering of As as well as the deposition of the Ga ions from the beam.

We consider the diffusion flux $\mathbf{J}$ can be affected by roughening, surface energy and wetting energy. Roughening represents the growth of islands. The islands are generated by nucleation and aggregation of diffusing atoms on the surface. In the model, the growth of islands is described as an up-hill flow along the slope, $\alpha\nabla h$, where α is the growing rate, which can be affected by the mobility of atoms and sputtering yield. Although atoms are not actually moving upward in islands, the height of islands comes to increase when atoms are absorbed from the circumference of the islands as droplets grow by absorbing surrounded molecules.

On the contrary to a roughening flux, there is a smoothening flux to decrease the chemical potential μ. We consider the total chemical potential as a sum of surface energy μ_γ and wetting energy μ_w, $\mu = \mu_\gamma + \mu_w$. Atoms tend to move toward a low

chemical potential. We assume that this driving force is proportional to the diffusion flux, thus we have $\mathbf{J} = -M\nabla\mu$, where M is the mobility of atoms.

The chemical potential due to surface energy can be expressed by $\mu_\gamma = K\gamma\Omega$ [66], where K is a surface curvature, γ is a surface energy per unit area, and Ω is an atomic volume. The curvature can be expressed by the second derivative of the surface height, so $K = -\nabla^2 h$.

Wetting energy is considered in the evolution of thin films. When films are very thin, the free surface energy of substrates can affect morphological changes in the films. In the model, we assume Ga atoms diffusing on the surface as a Ga layer like a thin film. There should be wetting interactions between two different materials of the Ga layer and the GaAs substrate. Wetting energy is expressed as an exponentially decaying function of h with a singularity at $h \to 0$, which is[68]

$$\mu_w = -w_0 \left(\frac{h}{\delta_w}\right)^{-\alpha_w} \exp\left(-\frac{h}{\delta_w}\right), \tag{2.21}$$

where δ_w is a characteristic wetting length, w_o represents the intensity of wetting interactions, and α_w characterizes a singularity of the wetting potential.

Consideration of all the contributions gives the following diffusion flux

$$\mathbf{J} = \alpha\nabla h + M\Omega\gamma\nabla(\nabla^2 h) + M\nabla\mu_w . \tag{2.22}$$

Rescaling the in-plane distances by $l_0 = \left(M\Omega\gamma/\alpha\right)^{1/2}$, the normal distances by $l_1 = \alpha/\beta$, the time by $t_0 = M\Omega\gamma/\alpha^2$, and the supply by $\eta_0 = M\Omega\gamma\beta/\alpha^3$, and letting $\omega = M\beta w_0/\alpha^2$ and $\delta = l_1\delta_w$, gives

$$\frac{\partial h}{\partial t} = -\nabla^2 h - \nabla^4 h + \omega \nabla^2 \overline{\mu_w} - (\nabla h)^2 + \eta \,, \tag{2.23}$$

where $\overline{\mu}_w = -\left(h/\delta\right)^{-\alpha_w} \exp\left(-h/\delta\right)$.

2.6.2 Numerical Simulations and Discussion

A Hexagonal Formation

The finite difference method was used to solve Equations (2.23). The size of domain was taken to be 100×100. A periodic boundary condition was applied. The grid spacing and the time step were taken to be Δx=Δy=2 and Δt=0.1. The initial surface morphology was constructed by adding a small random perturbation with magnitudes between 0 and 10^{-1} to a flat surface. We assume a Ga layer with an initial thickness of 0.5. At every time step, random numbers (to mimic the statistic nature) with the order of 10^{-4} are added to supply of Ga atoms on the surface.

Representative results are shown in Figure 2.24. The parameters used in the simulation are $\omega = 1$, $\delta = 1$, and $\alpha_w = 1$. Figure 2.24 (a) shows the initial stage with random numbers. At t=1000 small peaks are aggregated, and form small mounds. Yet, they look like a chained pattern due to small heights. At t=1300, small islands begin to appear and grow. At t=2000, the growing rate of islands becomes moderate. Some islands still continue to be generated and find the position to be settled down while they slightly move around. At t=5000, uniform islands are arranged hexagonally. After t=5000, the size and the location of the islands do not change, and show the same formation at t=10000, which represents the system reaching a steady state. The results show that

wetting energy can suppress coarsening and play an important role in the formation of regular nanostructures.

Here, the reason for the hexagonal formation is discussed. The hexagonal formation is the most optimized formation in the competition between the supply and the sputtering of atoms. The movement of islands is caused by the directional supply of atoms, which is explained in Figure 2.25. The island supplied by atoms from the left will be expanded to the left. If the amount of sputtered atoms is same as that of supplied atoms, the island will keep a uniform size. When the volume decreases by sputtering, the decrease is isotropic. Although directional sputtering may happen, the droplet-like island quickly recovers the hemi-spherical shape, and the decrease of its size looks as happening in all directions.

Newly generated atoms on the surface will diffuse and be absorbed to islands, eventually contributing to the movement of the islands. Considering directional supply contributes to the movement of islands, the most stable and efficient formation will be triangular. This is because each island in the triangular formation has a circular denuded zone, where Ga atoms are generated and absorbed to islands. Having a circular denuded zone represents no directional supply. This can be interpreted as all the distances between islands should be same (Figure 2.26 (a)).

In the case of a rectangular formation, the distance between neighboring islands is shorter than that of diagonally placed islands, which means the supply of atoms cannot be equal from all directions around the island (Figure 2.26 (b)). Although the supply can be balanced, if a periodic condition is considered, the most efficient and the smallest unit is a triangular formation. Figure 2.26 (c) shows that a periodic formation of the triangular

formation is a hexagonal formation, which is same as the result of the simulation. Any island in the hexagonal formation has the same distances with all neighboring islands. All of them are supplied equally with Ga atoms from the surface.

Shadow Effect

In the experiment, the islands are arranged hexagonally, and form chains, whose directions are perpendicular to that of the incident beam at off-normal bombardment. In the previous simulations, we have shown that the shadow effect is the reason for chain formation.

In the model we implemented the shadow effect by limiting the supply of atoms in the shadow area behind the droplets. Consider an incident beam coming from the positive x direction. A point on the back surface of a droplet has a normal with a negative projection in x. At each time step we examine the normal at each grid point to determine the cross-section outline of the droplets facing the beam. We then project this outline to get those grids within the shadow area. The direction of the incident beam is fixed so the shadow area increases as the droplet grows. We do not add random numbers which mimic the mass supply to the grids in the shadow area. This calculation is performed in each time step. Thus when an area moves in a shadow, it stops having any mass source η since that moment, until it moves out of the shadow.

All the initial conditions and parameters used are the same as those used in the previous simulation. Figure 2.27 shows representative results. At t=1000, small peaks are aggregated and form small mounds that look as patterns on the surface due to small heights. At t=3000, the islands are generated, showing no tendency of a regular

arrangement. Some are still on the process of formation. The connected mounds are evolved into individual islands and lined up at t=4000. Although the alignment along the y-axis begins to show, a few are off the line. At t=5000 the islands that was misaligned at t=4000 perfectly lined up as adjusting the position, which is indicated by a dashed line. As time passes, a regular arrangement is more clearly seen, and finally, nicely ordered islands are formed at t=10000. They show a hexagonal formation aligned perfectly perpendicular to the x axis. The result is comparable with the previous simulation, which shows a hexagonal formation with a random orientation.

Figure 2.28 shows a top view of the result at t=10000 and corresponding shadow zones. At Fig 2.28 (a), the distance a is longer than the distance b. This is a different result, compared to the previous result showing all neighboring islands are separated with the same distance. The reason is that the supply of atoms becomes anisotropic due to the shadow effect. The island moves to the opposite direction against the shadow zone in order to equilibrate the supply from the both sides after the supply of atoms is limited from the direction of the shadow zone. As a result of the movement to the right, the islands are lined up, and the hexagonal formation is elongated along the beam direction.

2.6.3 Conclusions

In conclusion, we have revealed a mechanism of hexagonally ordered droplet formation during preferential sputtering, and developed a model that incorporates the essential kinetics. We show that a competition between the mass supply and sputtering determines the stable size of the droplet, while the anisotropic mass flux drives the motion of the droplet. The balance of the flux leads to a hexagonal pattern. The shadow

effect causes the chains of the droplets to line up perpendicular to the incident beam and a lattice elongation along the projection of the beam direction. The fundamental mechanism may be applicable to other material systems, or motivate thoughts in other physical processes such as thin film growth to form ordered nanoscale features by self-assembly.

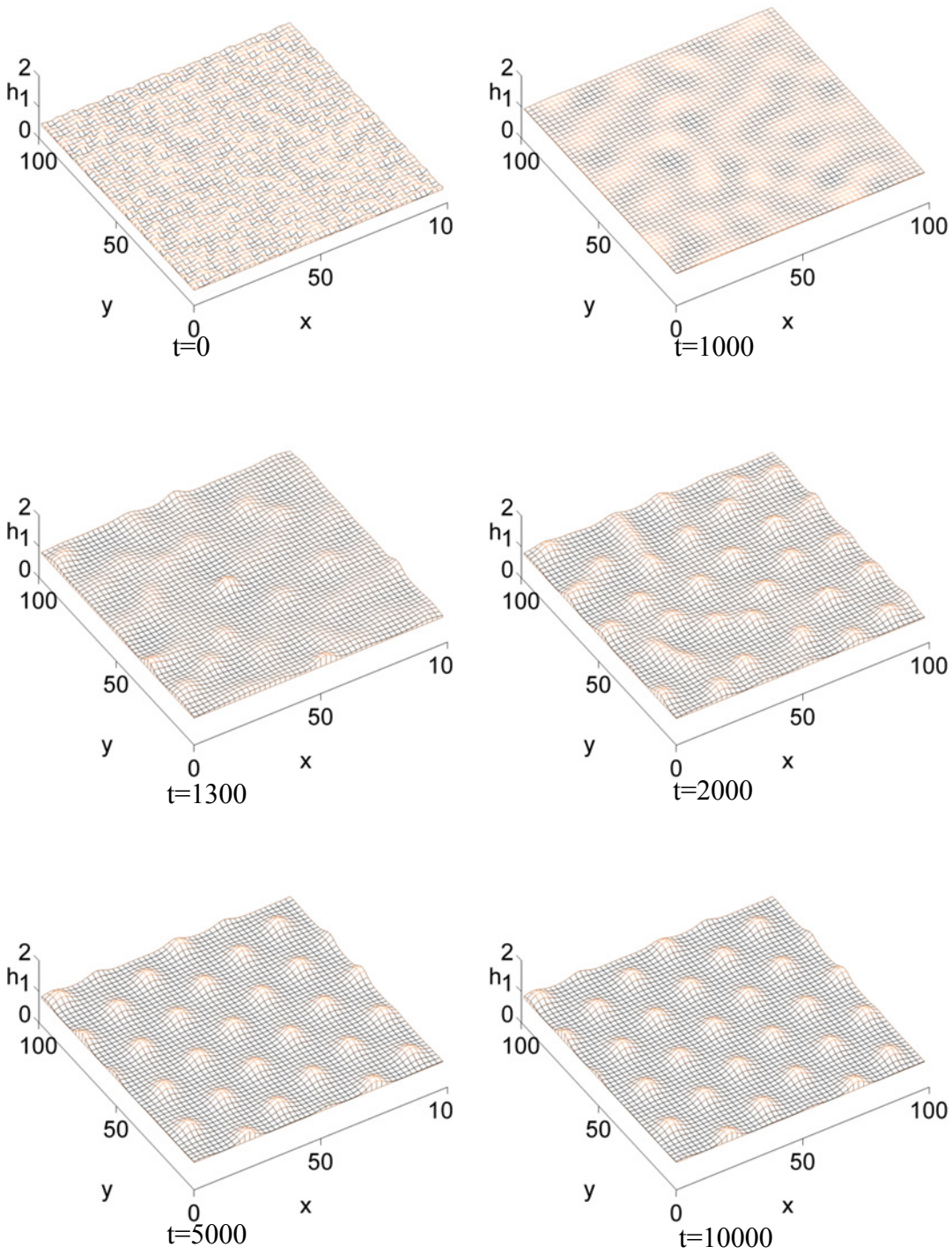

Figure 2.24 Evolution sequence showing self-assembled islands, which are perfectly arranged at a hexagonal formation.

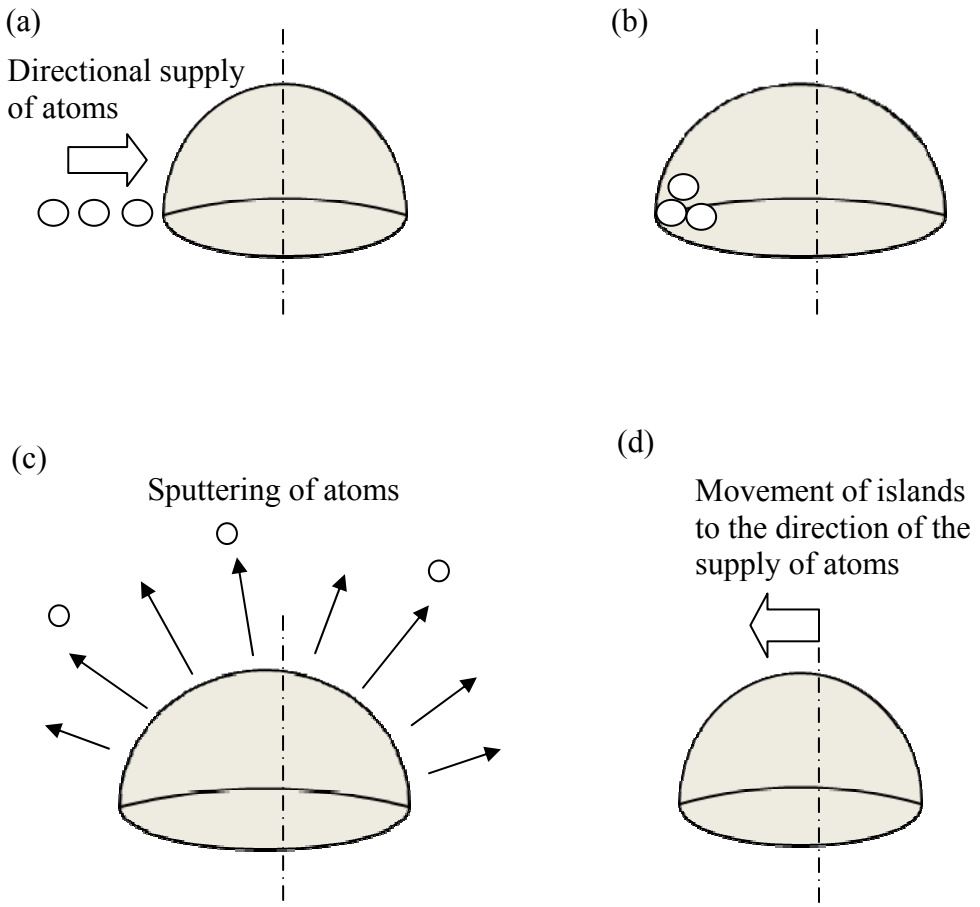

Figure 2.25 Schematic of moving mechanism of an island due to directional supply of atoms. (a) directional supply of atoms from the left side at the perimeter of the island. (b) The volume is increased to the left where atoms are absorbed. (c) Sputtering happens all around so the decrease of the size is symmetric. (d) The center of the island has moved to the left as a result of directional supply.

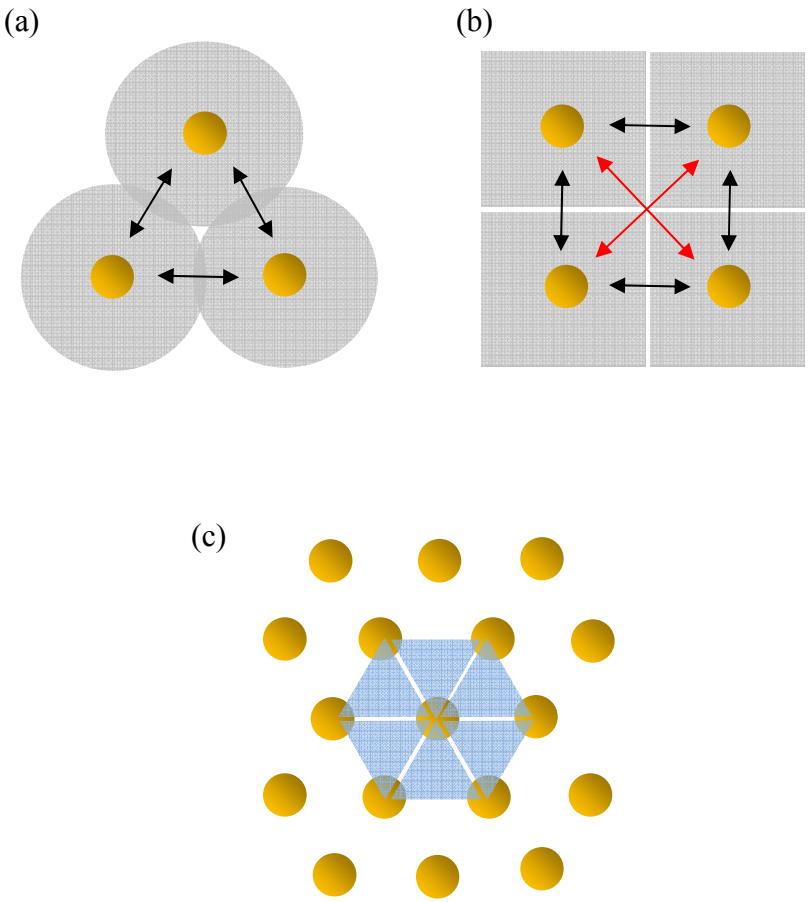

Figure 2.26 (a) Triangular formation: denuded zone (gray) is a circle, which means uniform supply all around.(b) Square formation: denuded zone is a square, which has a larger supply from the diagonal direction. (c) Periodic arrangement of the triangular formation gives hexagonal arrangement.

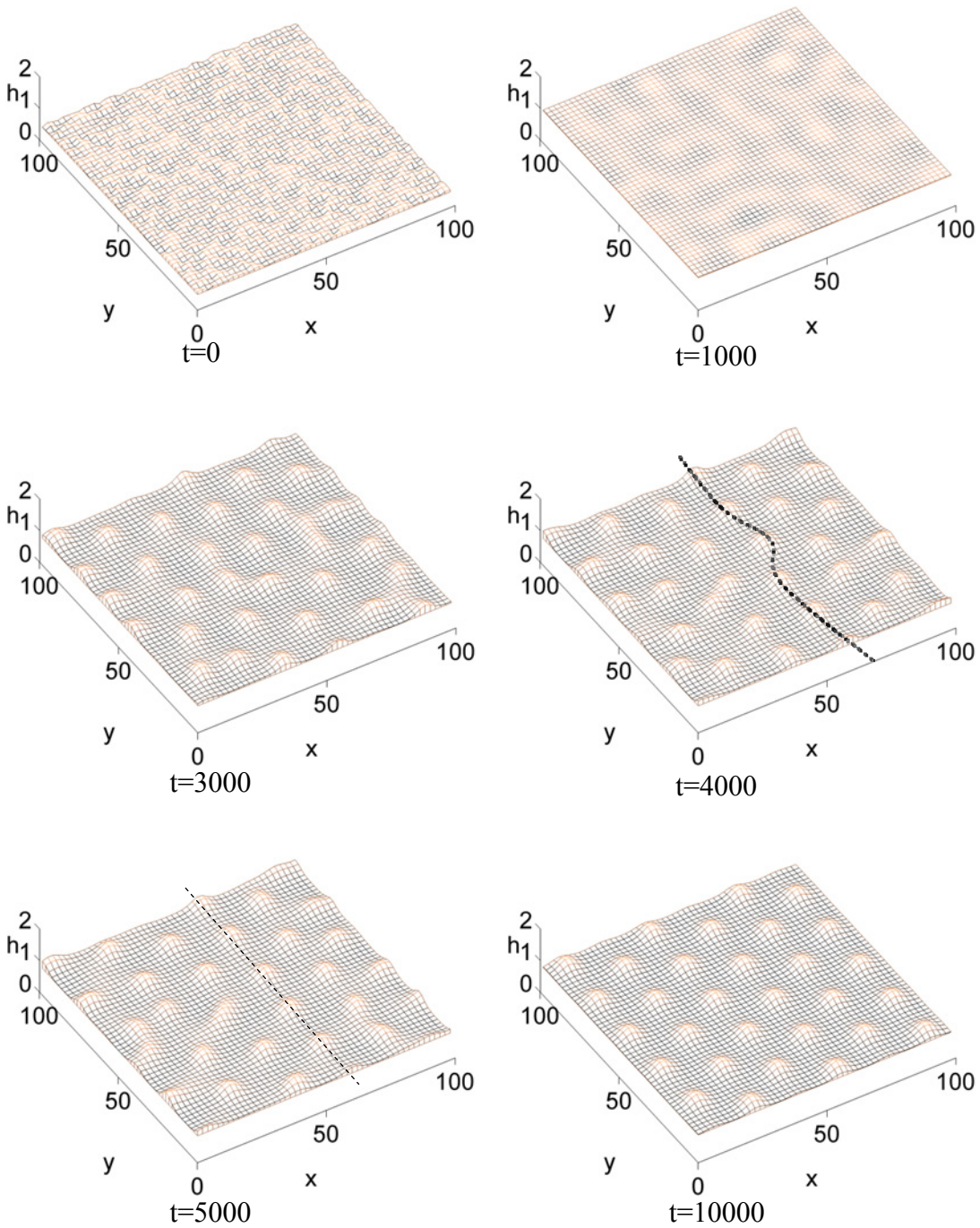

Figure 2.27 Evolution sequence when the shadow effect is considered. It shows that self-assembled islands are hexagonally arranged as well as form chains perpendicular to the incident beam from the positive x axis.

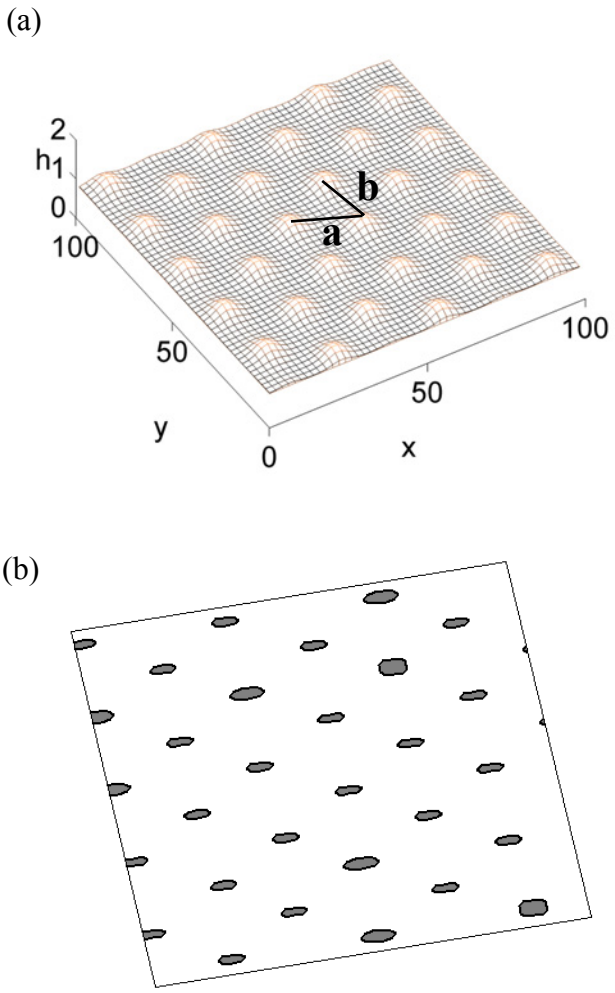

Figure 2.28 (a) A top view of the simulation result at t=1000. The distance a is longer than b which is a result of the shadow effect. (b) The shadow zone is shown just behind the islands to the left.

CHAPTER 3

Performance of Molecular Machines under Constrained or Load Conditions

3.1 Introduction

3.1.1 Background

Artificial molecular motors and machines have recently attracted considerable interest in the field of nanoscience [69-74]. Different kinds of molecular motors such as molecular shuttles[75], valves[76] and elevators[77] have been designed and studied. Among the molecular machines, rotaxane has gathered a large amount of attention because it can be a basic unit to build up complex molecular machines.

A rotaxane is a mechanically-interlocked molecular architecture. Figure 3.1 shows a schematic of a rotaxane. A cycling macromolecule encircles a dumbbell-like structure. The heavy molecular groups at the ends of the structure prevent disassociation. The dumbbell structure has two recognition sites where the energy state is stable when the ring structure is positioned on them. The ring structure is initially positively charged. It is known that π interaction between the ring and the recognition sites is the reason for stabilization[78]. π interaction is a non-covalent interaction, which is related to electron interactions[79]. If the recognition site is positively charged by external stimulus, which can be electrochemical[80, 81], light[82-84] or pH[76, 85], the ring moves to the other

site due to the electrostatic repulsion between the ring and the oxidized site. When the oxidized site is reduced, the ring moves back to the original site. These two sites where the ring switches back and forth are called stations.

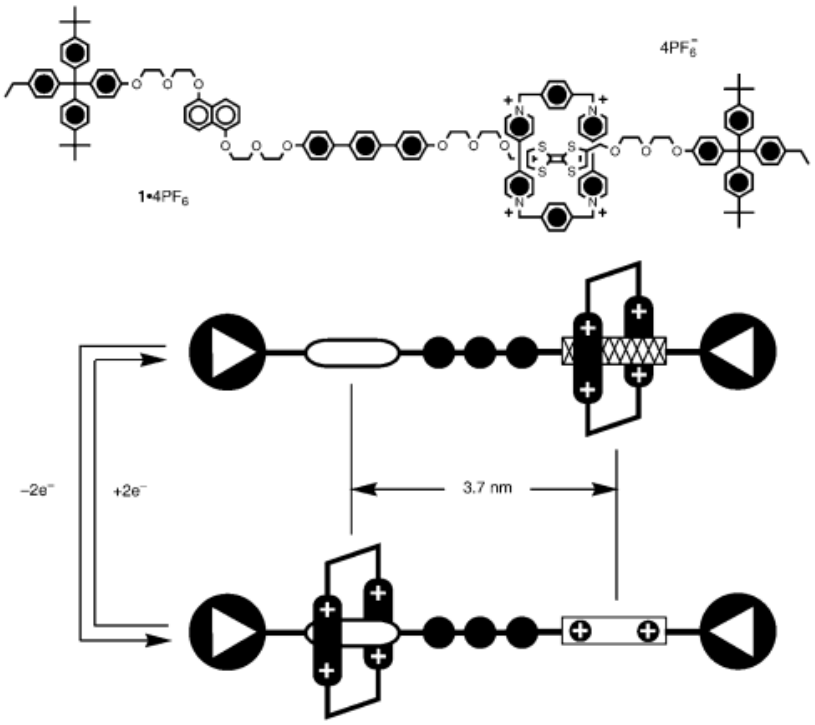

Figure 3.1 An example of a rotaxane with the TTF (hatched) and DNP (open) recognition units. Mechanically interlocked ring structure cannot escape due to heavy molecule groups at the ends. There are two stable stations (TTF and DNP) and the ring switches back and forth by oxidation and reduction [86].

The rotaxane will be more useful when it is combined with nano/micro systems rather than by itself. The switching process of the rotaxane can be used either electronically or mechanically. First, it has been shown that the electric current through the rotaxane is different depending on the location of the ring, suggesting that rotaxanes can be used for an electric on-off switch. For example, Figure 3.2 shows the concept of incorporating rotaxanes between metallic electrodes[87]. In addition, 64-bit molecular

crossbar circuits incorporating rotaxanes at the junctions were experimented, and the ability of writing ASCII characters has been demonstrated [88, 89].

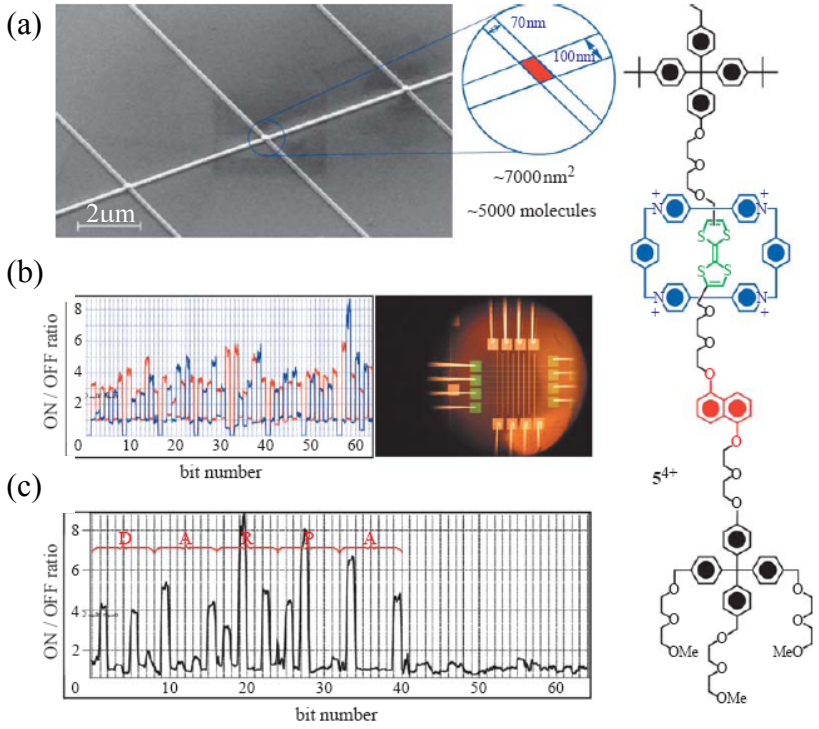

Figure 3.2 (a) A SEM image of the nanowire crossbars fabricated by e-beam lithography. The bistable rotaxane shown on the right is assembled at the junctions between horizontal and vertical wires. (b) 56th of the 64 bits in the array gave 2:1 ratios for ON/OFF. (c) The acronym 'DARPA' was stored in ASCII within the memory [87].

Second, the switching process of the ring enables rotaxane to produce mechanical work. It can be used for shuttling or a linear switching motion. For these processes, larger molecules are synthesized by connecting two rotaxanes in a series or a chain. For example, artificial molecular muscles produced by connecting two rotaxanes were coated on the micro-cantilevers, and beam bending was demonstrated, which was repeated by a cycle of chemical oxidation and reduction [90, 91].

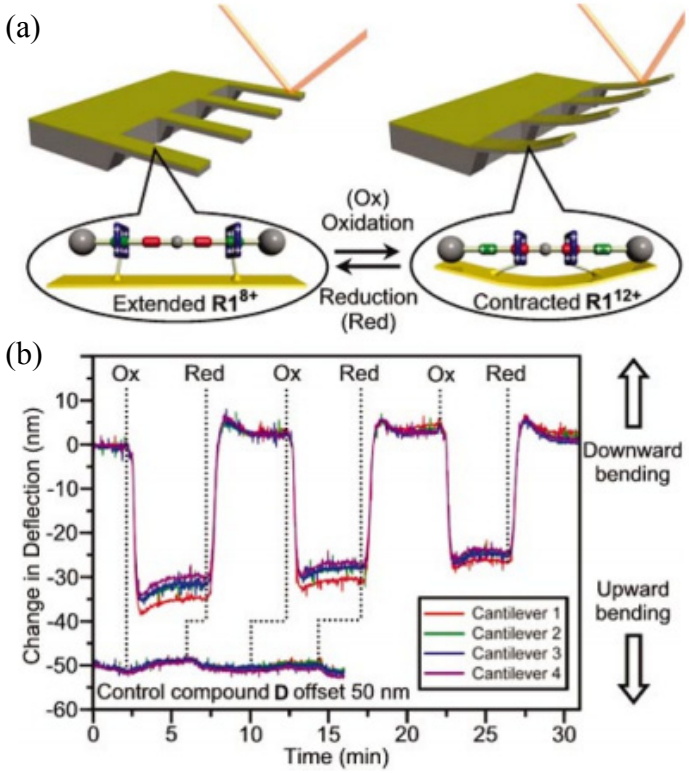

Figure 3.3 (a) Schematic of the mechanism of the device operation. (b) The graph shows bending of the four cantilever beams that are coated with a series of rotaxanes as the aqueous oxidant (Ox) and reductant (Red) solutions are delivered to the sample cell. Negative deflection corresponds to upward bending [90].

In addition to experimental investigations, theoretical studies have been performed to reveal physical characteristics of rotaxanes. Jang *et al* investigated the structural characteristics of self-assembled monolayers (SAMs) of bistable rotaxanes on Au surfaces[92]. They studied the effect of features including the stress, tilt angles and thickness of the SAM. The simulations showed that these features are related to the coverage density, and suggested the optimal packing density of SAM. Jaime and collaborators investigated the influence of water and acetonitrile solvent as well as the presence of counterions on the energetic and structural characteristics of the rotaxane that incorporates two recognition sites, benzidine and 4,4'-biphenol using molecular

dynamics (MD) [93, 94]. Briquet *et al* studied the equilibrium position of α-CDs, ring component, along the azobenzene typed chain at the experimental temperature of 330K, and calculated the energy profile with molecular mechanics (MM) method[95].

3.1.2 Motivation

As mentioned before, molecular motors and machines will be incorporated into micro systems for applications. While they are bonded to surfaces, they should undergo external loadings from the attached surface. In this situation, questions can be raised: what is the influence of external loads on the performance or designed work output, such as displacement and response time? Are the molecular machines strong enough to withstand the loading? Is there a limit of operation under various loading situations? The response of nano and molecular structures are subjected under loading raises interesting questions.

To simulate molecular structures, the MD method will be used. Before examining the influence of loading, a dynamic switching process should be implemented in the simulation because it is a key process that produces work output. After the switching process is enabled, we can then apply forces to the structure and examine the process.

First, we focus on the switching process of a rotaxane as a basic unit of a motor. So far, the dynamic switching process has not been systematically considered, although there are many theoretical efforts enlightened structural characteristics of rotaxane [96-98]. In this section, we will study the energetic and structural characteristics of the dynamic switching process of oxidized [2]rotaxane using MD simulations. While it is generally believed that the charge repulsion between the ring and the station drives ring

motion, it is not clear quantitatively whether this repulsion is strong enough for motion to happen, and how motion happens. Through molecular simulations, we identify the structural configuration during the switching process in detail. In addition, the simulations provide quantitative information such as the switching time, displacement and time evolution of energy, which are hard to measure in experiments. These quantitative results are valuable for the design and the application of molecular motors.

Next, the influence of forces will be examined. When external forces are applied to the structure, changes in performance are expected; for example, displacement is shortened and response time is delayed under increased load.

3.2 Methods of Molecular Dynamics (MD) Simulations

MD calculations in this work were performed with LAMMPS[99] developed at Sandia National Lab. A time step of 1fs was used for all simulations. Cutoff distances of 8Å and 50Å were used for the pair potential energy and electrostatic energy, respectively. Because the total length of the structure is about 47Å, electrostatic interactions were considered directly by setting a cutoff range of 50Å. The Verlet algorithm[100] was used to integrate the equations of motion. The canonical ensemble was used to control the temperature, which was set at 300 K with a Nose-Hoover thermostat [101, 102] (relaxation time of 0.1ps). The initial velocity was randomly generated in accordance with the system temperature of 300K.

To describe all the interactions between atoms, the Dreiding force field[103], which has been well tested in computational modeling of bistable [2]rotaxane[92, 96, 97], was employed in this simulation. The total potential energy is given by

$$E_{total} = E_{vdw} + E_Q + E_{bond} + E_{angle} + E_{torsion}, \quad (3.1)$$

where $E_{vdw}, E_Q, E_{bond}, E_{angle}, E_{torsion}$ are the total, the van der Waals, electrostatic, bond stretching, angle bending and torsion energies, respectively. Although the force fields provided by LAMMPS are not identical to those of the Dreiding force field, simple modifications allowed the use of the Dreiding force field in LAMMPS. The simulations use the Buckingham potential for van der Waals pair potential, harmonic bond style for bond stretching, cosine/squared angle style for angle bending, and harmonic dihedral style for torsion. These equations are summarized in Table 3.1. Parameters and methods for heterogeneous atomic pair interactions followed those in ref[103].

To calculate the electrostatic energy, the atomic partial charges were obtained from quantum mechanical calculations (QM) using Gaussian software[104]. We used B3LYP, which is widely used in chemistry, of density functional theory with 6-31G basis set. The partial charges of the ring and dumbbell structure were calculated separately. In the QM calculation the total charge of the ring was set to +4 electron charges and that of the dumbbell was set to neutral. After the partial charges were calculated, the results were fit to each atom in the input file of LAMMPS. To simulate the dynamics of the ring movement we also calculated the atomic partial charges when the TTF station was positively charged. The calculated partial charges of the TTF station are shown in Figure 3.4.

Table 3.1 The force field used in MD simulations.

	Dreiding force field	LAMMPS	Modified Constants used in LAMMPS
Van der Waals	$D_0\left\{\left(\frac{6}{\xi-6}\right)e^{\xi\left(1-\frac{r}{r_0}\right)}-\left(\frac{\xi}{\xi-6}\right)\left(\frac{r}{r_0}\right)^{-6}\right\}$	$Ae^{-\frac{r}{\rho}}-Cr^{-6}$	$A=D_0\left(\frac{6}{\xi-6}\right)e^{\xi}$, $\rho=\frac{r_0}{\xi}$ $C=D_0\left(\frac{\xi}{\xi-6}\right)r_0^6$
Electrostatic interaction	$C\frac{q_iq_j}{\varepsilon r}$	$C\frac{q_iq_j}{\varepsilon r}$	same
Bond stretching	$\frac{1}{2}K_R(r-r_0)^2$	$K(r-r_0)^2$	$K=\frac{1}{2}K_R$
Angle bending	$\frac{1}{2}\frac{K_\theta}{\sin^2\theta_0}(\cos\theta-\cos\theta_0)^2$	$K(\cos\theta-\cos\theta_0)^2$	$K=\frac{1}{2}\frac{K_\theta}{\sin^2\theta_0}$
Torsion	‼ EMBED Equation.DSMT4 $1-\cos(n(\phi-\phi_0))$	$K(1+d\cos(n\phi))$	same as ref [18]

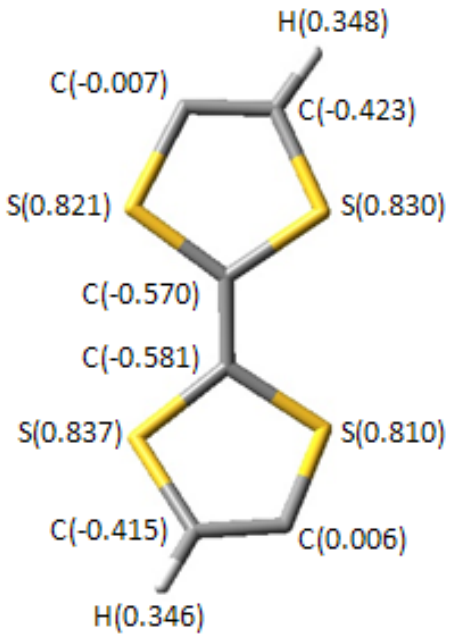

Figure 3.4 Atomic partial charges of the +2e charged TTF station, calculated with Gaussian.

3.3 The Switching Process of Constrained Molecular Motors

As a model for the study, we consider bistable [2]rotaxanes that have two recognition sites and the ring. Two sites are tetrathiafulvalene (TTF) and hydroquinone (HQ), which are π-electron rich components. The ring is cyclobis (paraquat-p-phenylene) ($CBPQT^{4+}$), which is π-electron deficient component (Figure. 3.5(a)). Figure 3.5(b) shows the model used in our simulations which is built with Gaussview. Considering the rotaxane is attached to the surface, free and constrained situations are investigated for both the neutral and oxidized structure.

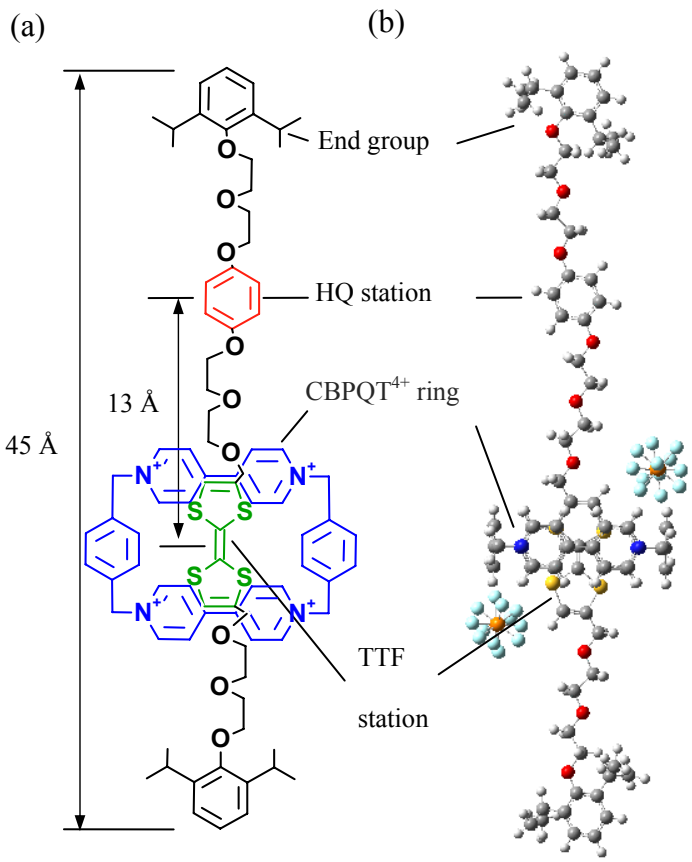

Figure 3.5 Bistable rotaxane studied in this paper: (a) schematic of atomic structure (TTF:green, HQ: red, $CBPQT^{4+}$:blue), and (b) computational model made by Gaussview and used in the simulations.

3.3.1 MD Simulations at the Neutral State

We first performed MD simulations for the neutral structure to determine whether the Dreiding force field can describe the characteristics of bistable rotaxane well. The simulation should capture the equilibrium state when the ring is positioned at the TTF station, which is known to be the most stable state. In all simulations, the ring was initially positioned at the TTF station. The partial atomic charges of the station were obtained from QM calculations by setting the entire dumbbell structure as neutral. The snapshots of the MD simulation of a free non-constraint motor are shown in Figure 3.6.

From the initial configuration to 1000fs the ring changes from the vertical position against the dumbbell to the 45˚ angle. Then, the ends of the structure start to fold and head toward the opposite directions: the left end heads upward and the right end heads downward. At time 2500fs the structure shows a curved morphology. The ends of the structure tend to line up, which causes the structure to twist as shown for time 5000fs. Eventually the structure appears folded. During the simulation the ring stays within the TTF station and does not move out of the station. This result confirms that the ring positioned at the TTF station is stable. The simulations suggest that a free motor may fold spontaneously so that the movement of the ring is not linear. For practical applications, the chain should be bonded to a substrate or other load-bearing structures, and subjected to tension. The constraint can suppress the tendency of chain folding, and provide a smooth path for the ring movement.

The evolution of energy is shown at Figure 3.7. The black, red and green lines represent the total potential energy, nonvalence energy (van der Waals energy + electrostatic energy), and valence energy (bond stretching + angle bending + torsion) respectively. After about 15000fs, the total potential energy converges, which means the system is equilibrated. The structure at time 50000fs has not changed much, compared with 15000fs. The curve of the nonvalence energy follows that of the total potential energy, suggesting that it plays a key role in the equilibrium process. The large decrease of the nonvalence energy is related to folding of the structure. Figure 3.8 shows a distance between two ending structures. Folding starts from the beginning of the simulation, and after 10000fs the structure is folded entirely. A slight increase after

80000fs is caused by changes of orientation of the ending structures, which corresponds to the decrease of non-valence energy.

Now consider the case where the two ends of a bistable motor are fixed, such as attached to a substrate. This was achieved by constraining the positions of hydrogen atoms at the end of the structure. In the simulation we set the velocity of these atoms to zero so that their positions did not change. Figure 3.9 shows the result. The ring adjusts its position and angle until it reaches about 45˚. Similar to the unconstrained situation, the TTF station is the stable location for the ring. Compared to Figure 3.8, Figure 3.10 shows smaller decrease of the nonvalence energy due to the non-folding situation. These results show that the ring is stable at the TTF station regardless of structural folding or whether the structure is attached to a substrate.

The location of the TTF station is compared as a function of time at Figure 11. The TTF for the free case stays almost at the same location, indicating zero displacement; on the contrary, the TTF for the constrained case has moved about 2.5 Å. This movement does not suggest the ring is off the station. The ring is within the range of the station as seen Figure 3.9, and the system seems to achieve a lower energy state by moving the ring instead of folding the structure, which is prevented by constraints.

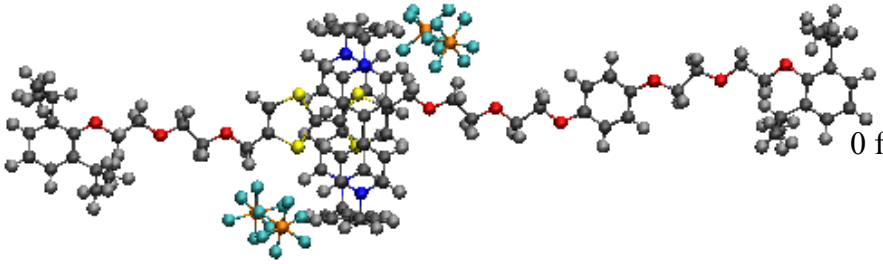

0 fs

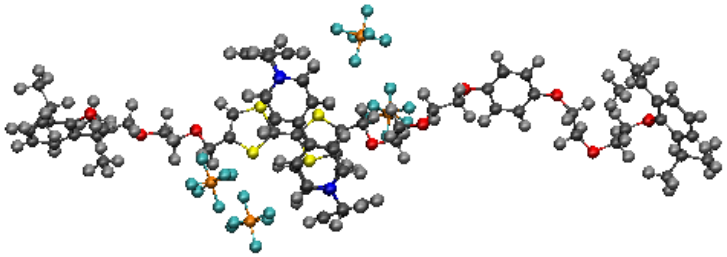

1000 fs

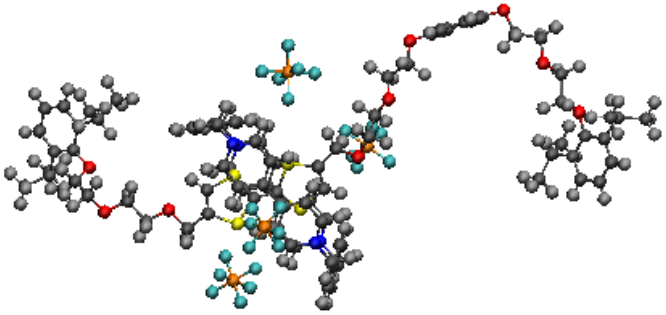

2500 fs

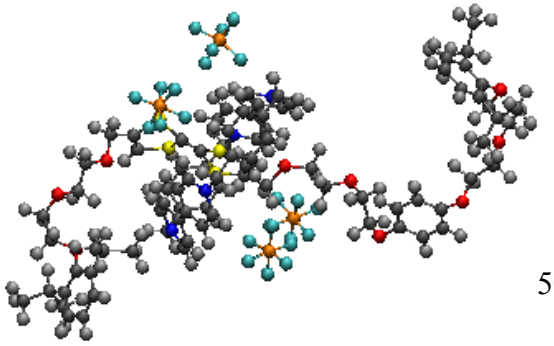

5000 fs

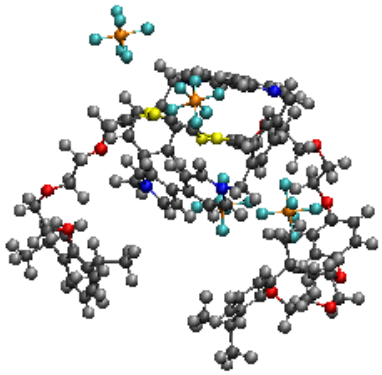

10000 fs

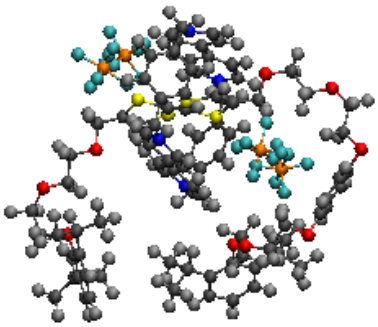

15000 fs

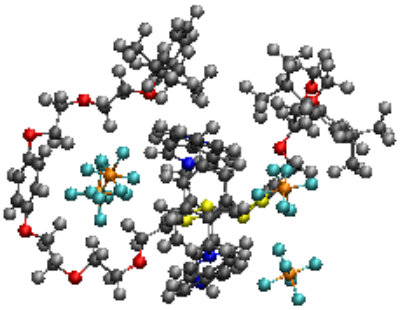

100000 fs

Figure 3.6 Conformational evolution of the neutral and unconstrained rotaxane.

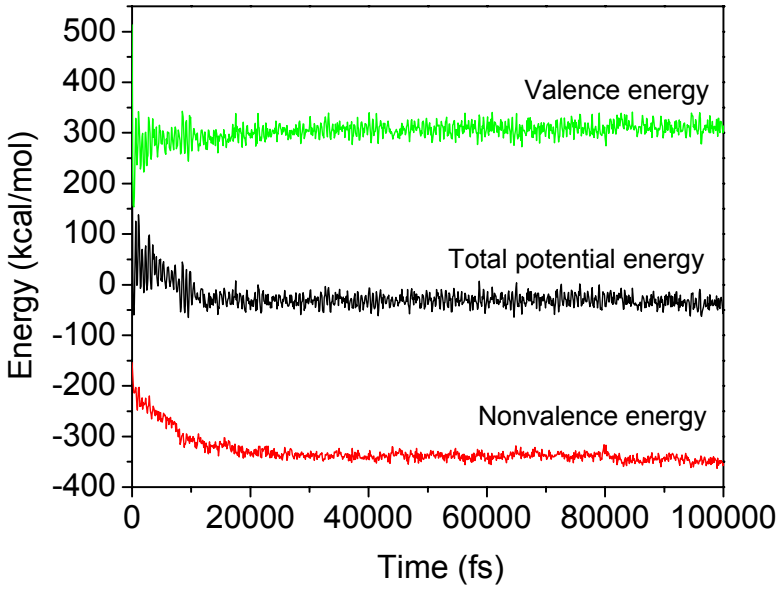

Figure 3.7 Evolution of energy for the neutral and unconstrained rotaxane.

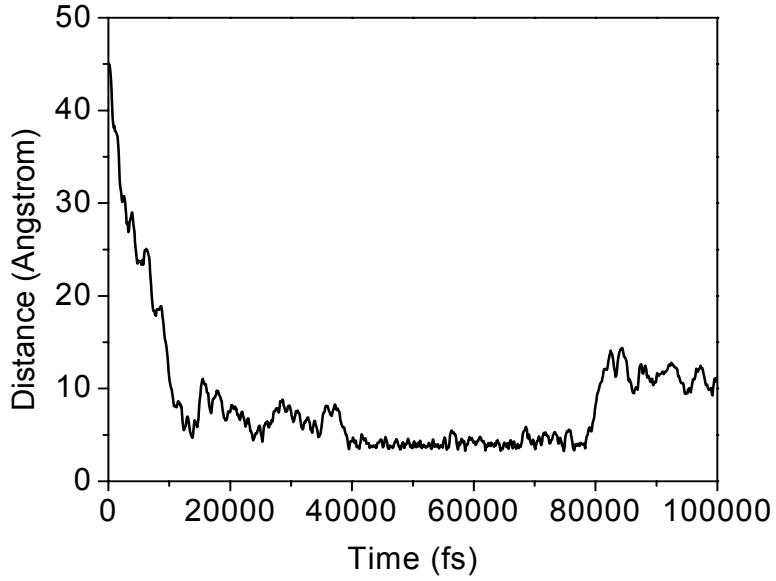

Figure 3.8 Distance between two stoppers.

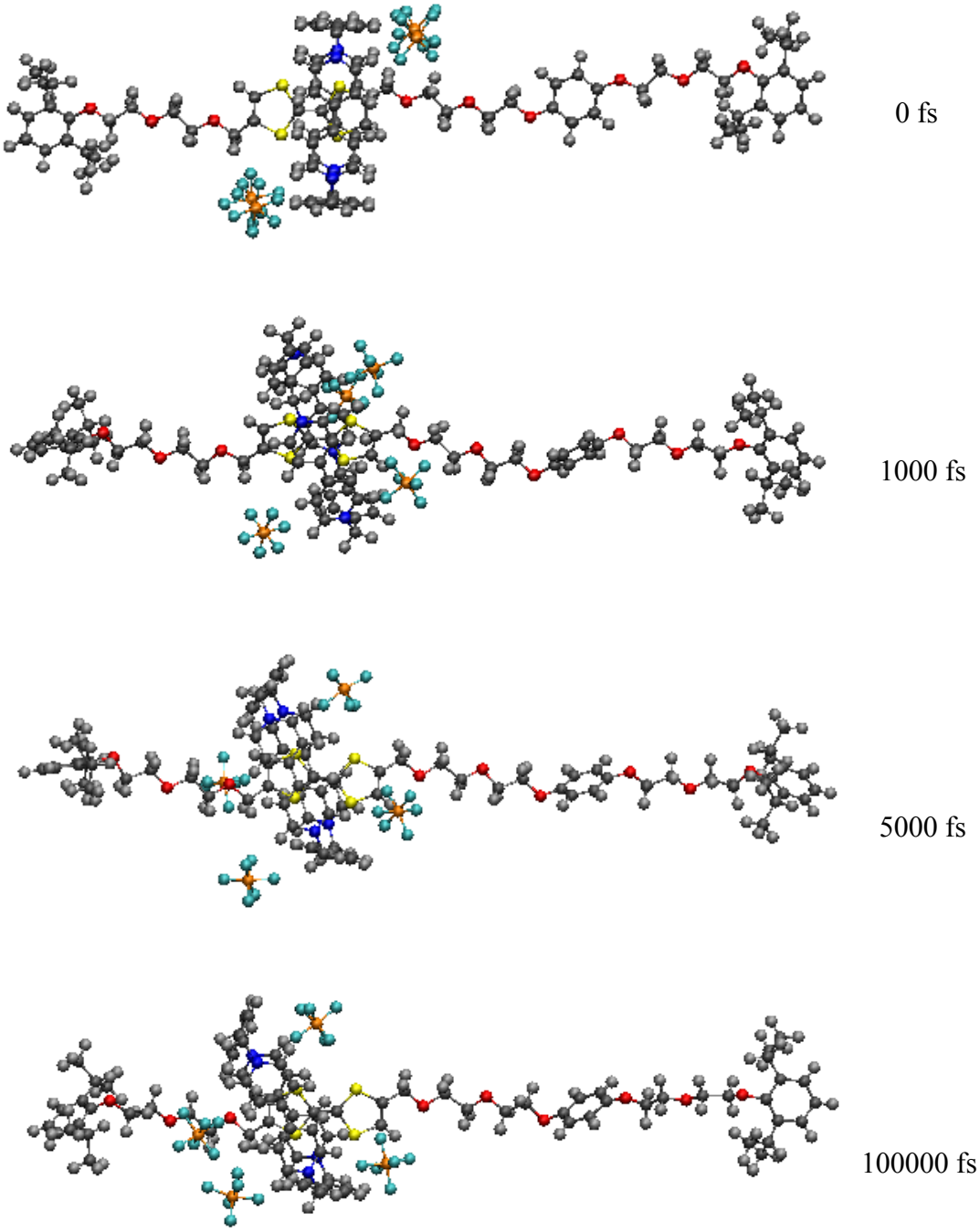

Figure 3.9 Conformational evolution of the neutral and constrained rotaxane.

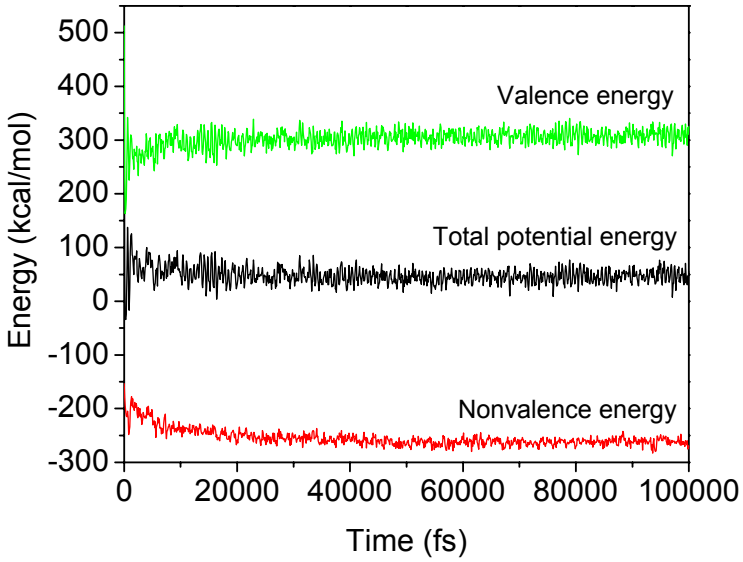

Figure 3.10 Evolution of energy for the neutral and constrained rotaxane.

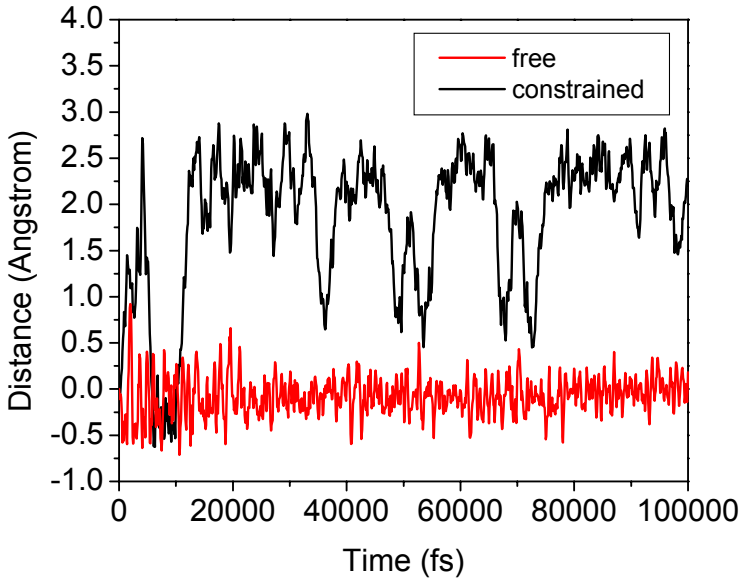

Figure 3.11 Graph of distance between the TTF station and the center of the ring component as a function of time (red line: neutral and unconstrained rotaxane, black line: neutral and constrained rotaxane).

3.3.2 MD Simulations at the Oxidized State

We then investigated the dynamic switching process. When one TTF station is oxidized, it carries positive charge. The electrostatic repulsion between the ring and the TTF station drives the ring to move to the other station. First, we considered the case where the two ends are not fixed. Figure 3.12 shows representative results. The ring is originally positioned at the TTF station. Under repulsion, the ring leaves its original location, and moves rapidly along the chain. At time 1500fs the ring passes through the middle of the structure. The backbone structure is slightly curved, although the deformation is not large as much as shown in the neutral case. The ring arrives at the HQ station at about 4000fs. After the ring arrives at the HQ station, it does not move out of the station and settles down. As the ring is positioned at the HQ station, the structure starts to fold, and it is totally folded at 14000fs. Figure 3.13 shows the evolution of energy. At around 5000fs a relatively big drop is seen in the non-valence energy. This drop is caused by the arrival of the ring to the other station, representing a stable state. The continuous decrease in energy is due to the folding of the structure. Figure 3.14 shows the distance between the center of the ring and the TTF station as a function of time. We can see overshooting of the ring and a subsequent process to equilibration. The stable position of the ring is about 9 Å from the TTF position. Our calculation shows the switching happens in about 10ps at a speed of 9 Å /10ps= 90m/s, suggesting its capability for fast response applications. The slight increase of the distance after 30000fs is caused by the change in the angle of the ring.

Next we studied the case where the two ends are fixed. Figure 3.15 shows representative results. Because of the fixed two ends, the chain structure does not show

much deformation. The ring shows tilting and morphological changes when moving to the HQ station, but maintains an integrated structure. Before reaching the HQ station, the ring moves back and then quickly settles down in middle of the structure. No significant change in the location of the ring was observed between 15000fs and 100000fs. Figure 3.16 shows evolution of corresponding energies. The non-valence energy decreases continuously, and does not show much difference after 10000fs, when the ring reaches the farthest point in the middle of the structure. Different than the free case, a sudden decrease in the non-valence energy is not seen because the ring does not reach to the other station. Figure 3.17 shows the distance between the center of the ring and the TTF station as a function of time. We can see overshooting is larger than the free case. The displacement of the ring at the stable position is about 5.5 Å, which is less than the displacement of the free case.

3.3.3 Discussion

Here we have an interesting result. We had 9 Å of displacement when the ends are free. This is shorter than the original distance between two stations, which is about 13 Å. We postulate that the short displacement is due to folding of the structure although the ring actually moves from the TTF station to the HQ station. We expected that a larger displacement would be obtained if the ends are fixed, because folding can be prevented. However, the displacement was shorter than the free ends, which is 5.5 Å. The ring did not arrive at the HQ station and settles down in the middle of the structure.

This result suggests that structural deformation plays an important role in the switching process. If the structure is stretched and fixed to prevent any deformation, the

ring cannot overcome the energy barrier between the two stations and will get stuck during the process. The different configurations are clearly compared in Figure 3.18. The snapshots when the ring is in the middle of the structure are compared. We can see the dumbbell structure is curved in the case of the free ends; on the contrary, the structure is straight in the case of the fixed ends.

Molecular motors are usually attached to a solid surface in many applications. It should be cautioned that a fully stretched motor may not function as desired. For optimal operation, flexibility of the backbone should be allowed when the ends of the motors are bonded to the surface.

3.3.4 Conclusions

In summary, we have presented the structural and energetic analysis of a bistable molecular motor when the TTF station is neutral or charged, and the dynamic ring switching process when the station is oxidized by MD simulations. For the neutral structure the ring component stays at the TTF station in both the free and constrained situations. The dynamic switching process happens in about 10ns. The simulation also shows the importance of structural deformation during the switching process. The bistable [2]rotaxanes may be assembled into active materials for various actuator applications. They may also connect in serial, the ring of one rotaxane attached to the end group of the other, to form a daisy-chain molecular muscle, which can generate a large displacement upon actuation.

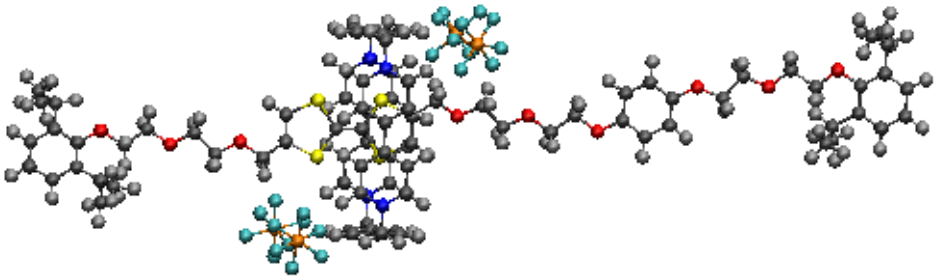

0 fs

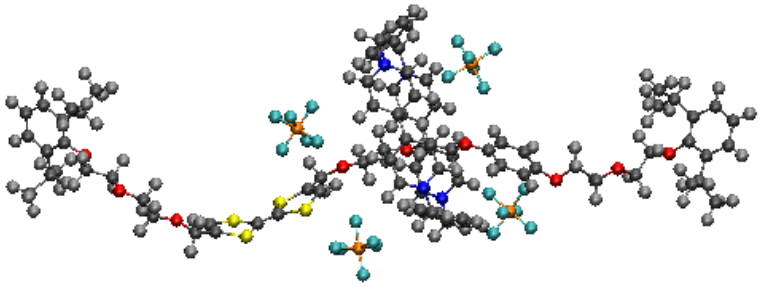

1500 fs

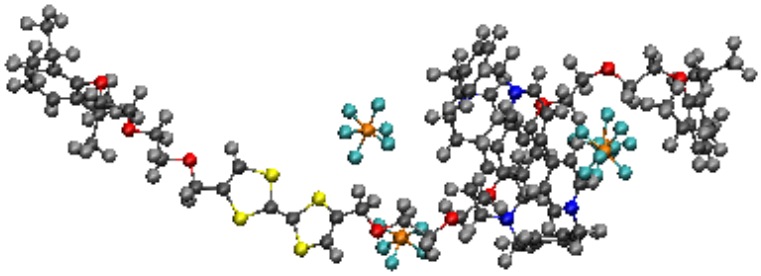

4000 fs

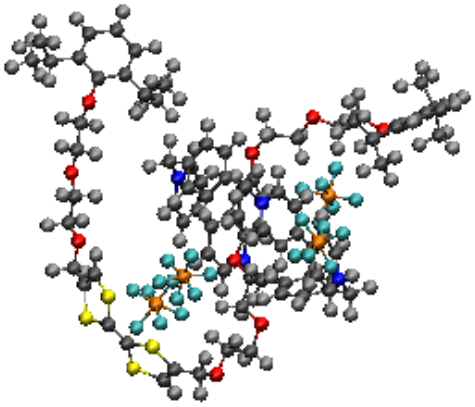

6000 fs

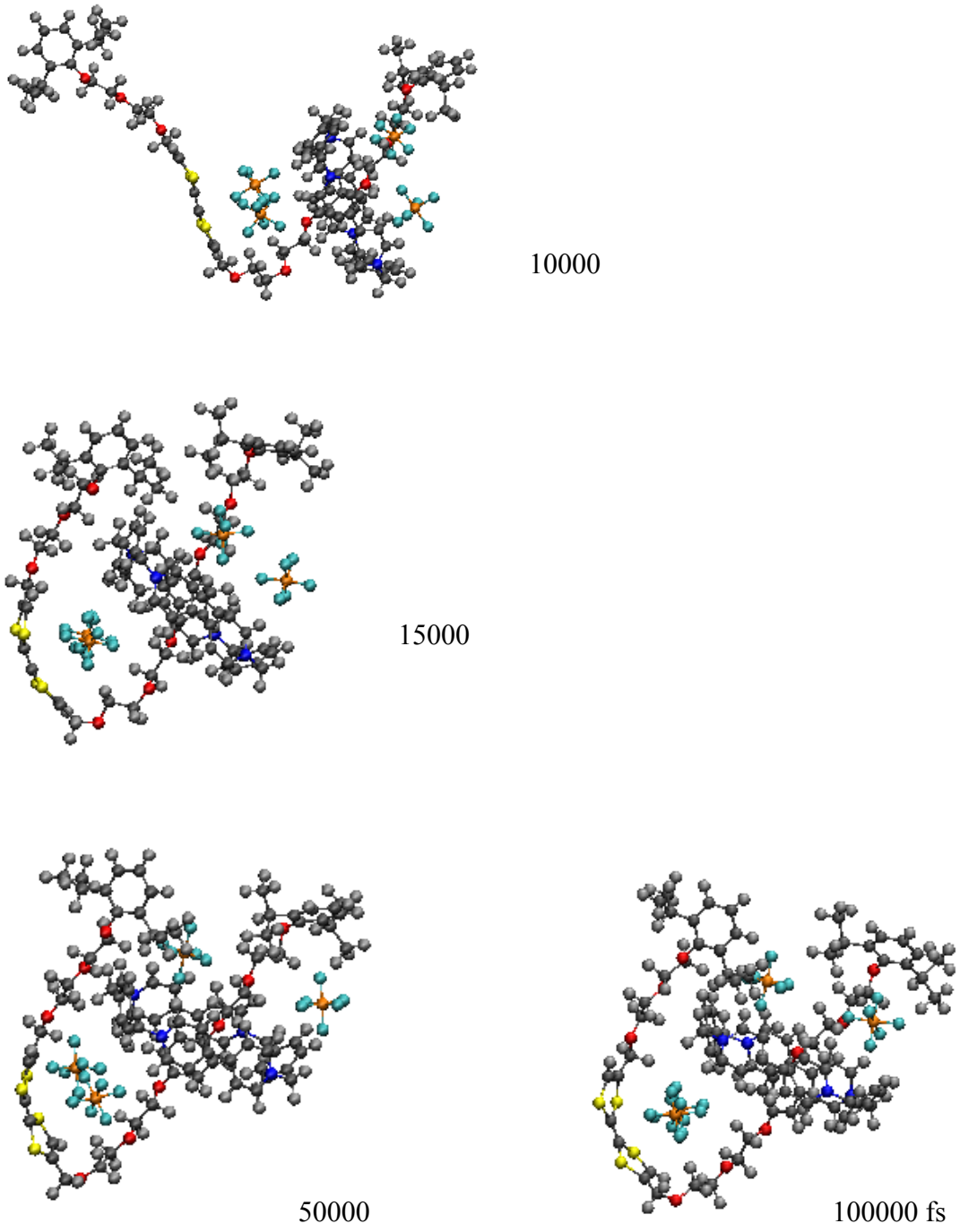

Figure 3.12 Conformational evolution of the oxidized and unconstrained rotaxane.

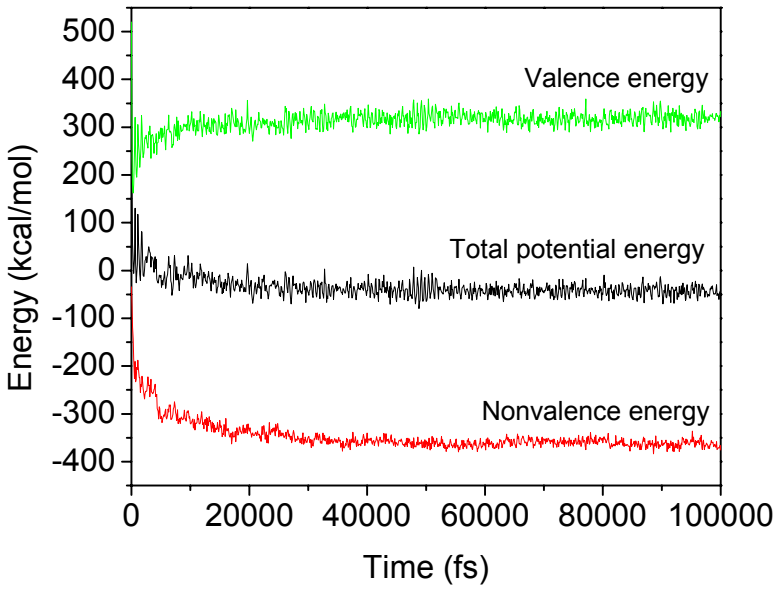

Figure 3.13 Evolution of energy for the oxidized and unconstrained rotaxane.

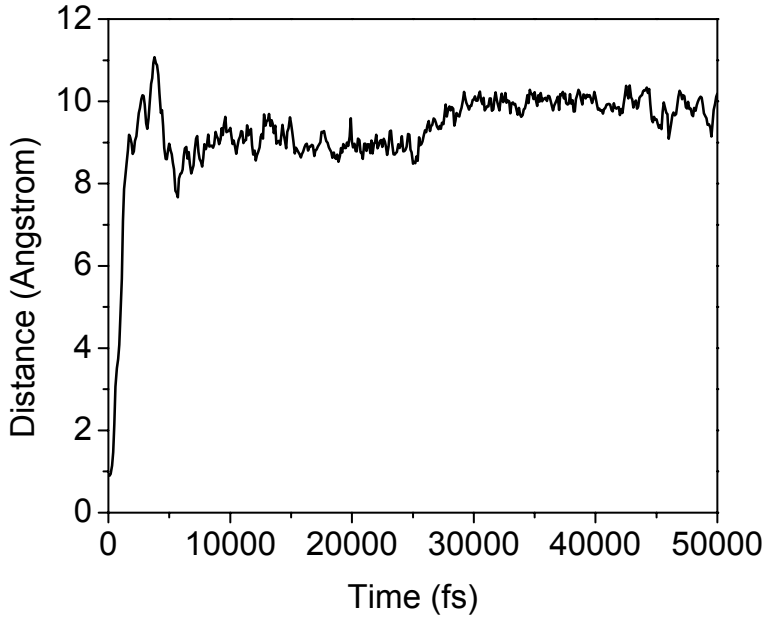

Figure 3.14 Graph of distance between the ring and the TTF station for the oxidized and unconstrained rotaxane as a function of time.

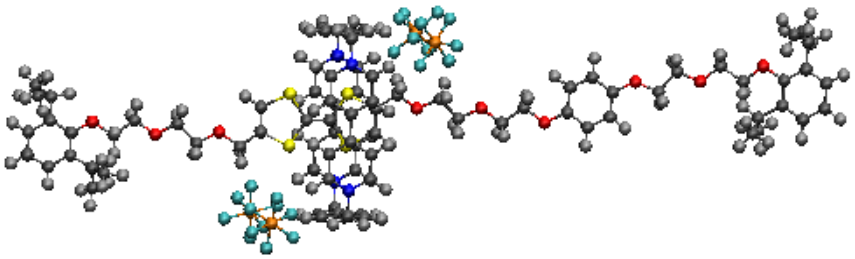

0 fs

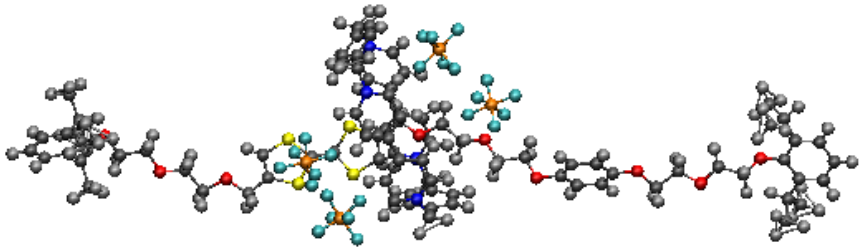

1000 fs

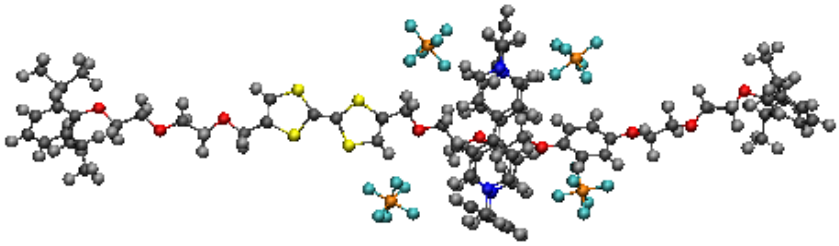

3000 fs

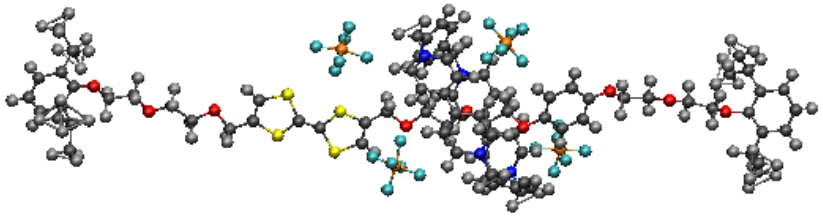

5000 fs

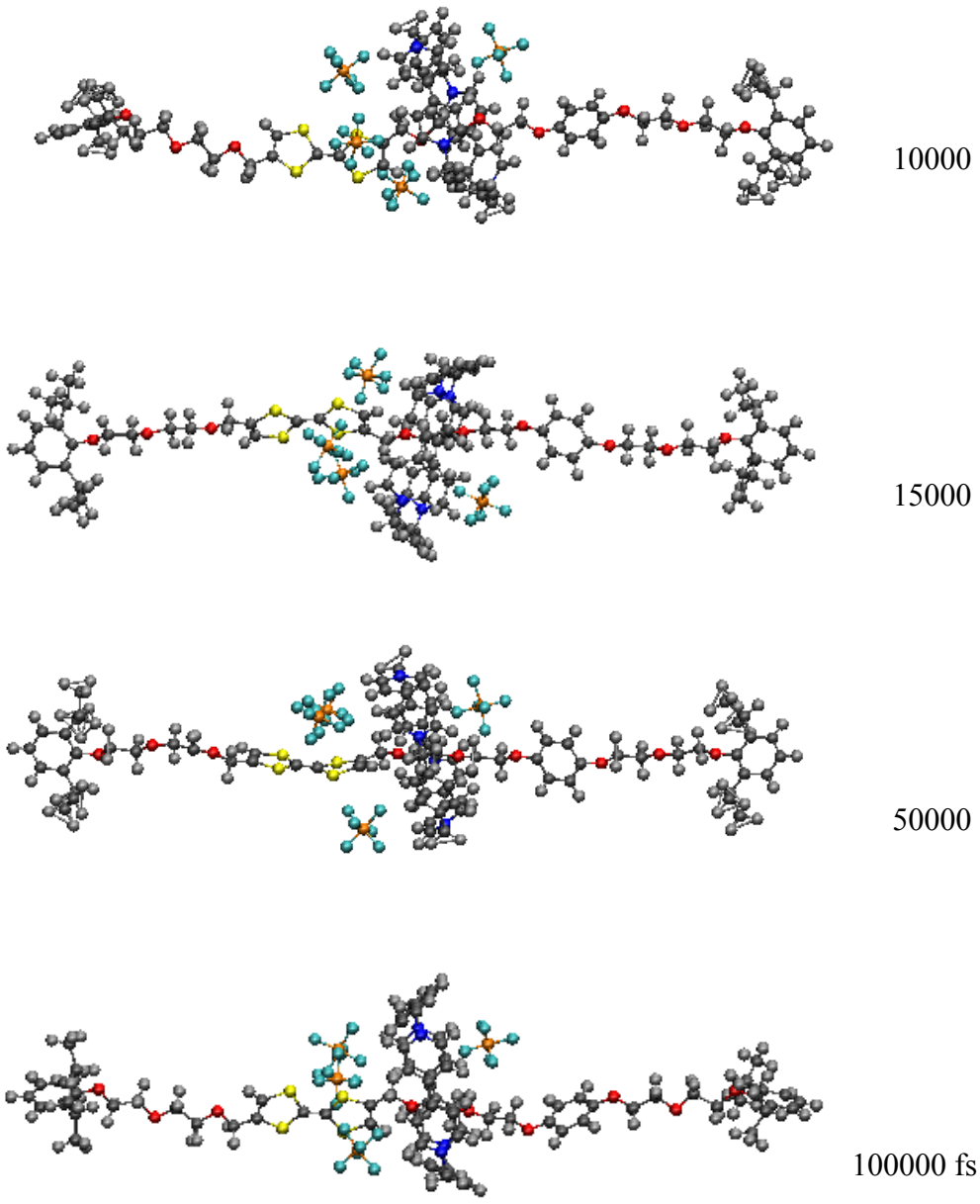

Figure 3.15 Conformational evolution of the oxidized and constrained rotaxane.

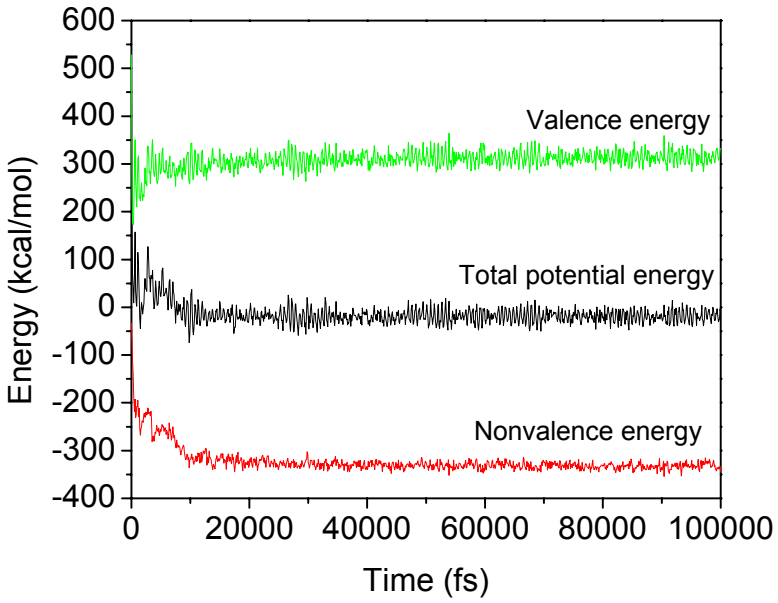

Figure 3.16 Evolution of energy for the oxidized and constrained rotaxane.

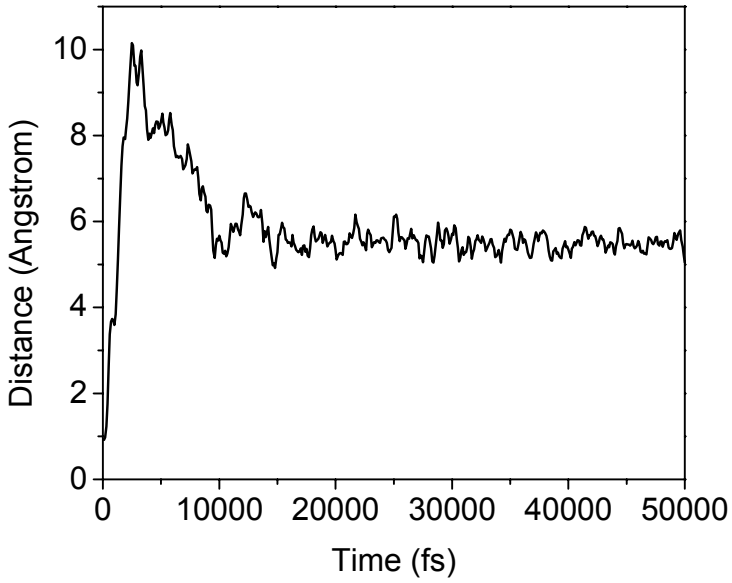

Figure 3.17 Graph of distance between the ring and the TTF station for the oxidized and constrained rotaxane as a function of time.

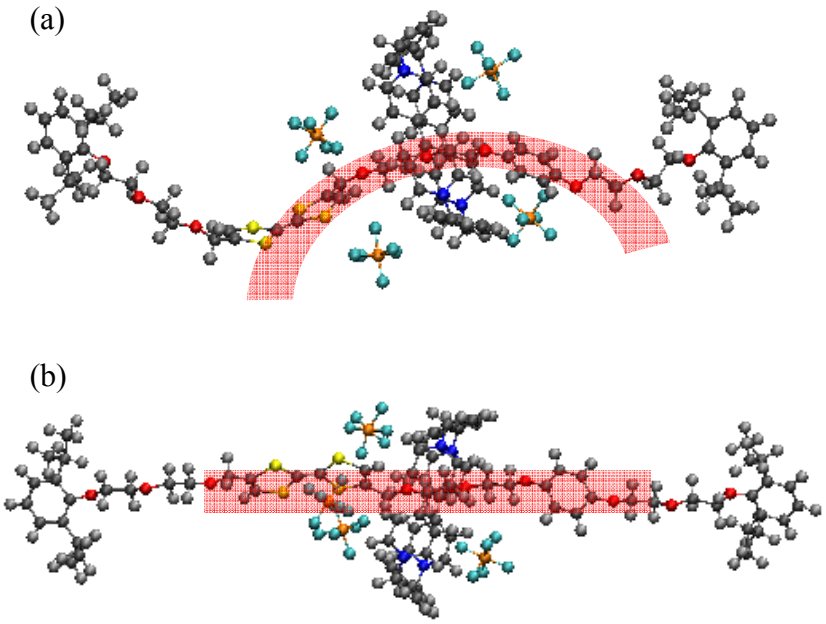

Figure 3.18 Comparison of configurations for the free and constrained case during the switching process. (a) the backbone structure is curved for the free ends (1500fs). (b) the structure is straight without distortion for the constrained ends (15000fs).

3.4 Artificial Molecular Muscle under Load Conditions

3.4.1 Introduction

As an effort to use the ability of rotaxanes, which can produce mechanical work, people synthesized a molecular muscle based on rotaxanes, which reminds of the biological skeletal muscle within human bodies. The capability of the molecular muscle has been verified by experiment. In experiment, micro-cantilevers that are coated with molecular muscles are bent and restored repeatedly by oxidation and reduction [90, 91]. This experiment promised a high possibility of the realization of engineering systems at a molecular level.

Because the functional molecules assembled with MEMS devices should be bonded to a surface, it is necessary to characterize the influence of mechanical loading transmitted from the surface during operation. A large amount of mechanical loadings may reduce shuttling time or totally prevent the switching motion. The question is thus how large force can affect the shuttling operation. In this section, we will study the relationship between mechanical loading and shuttling of an artificial molecular muscle using MD simulations. The MD simulations are performed on the oxidized molecular muscle as increasing the forces applied at the ends of the structure.

Figure 3.19 shows the model studied in this report. It is a daisy-chain molecular muscle that is composed of two linear bistable rotaxanes mechanically interlocked each other. Each bistable rotaxane has two recognition sites of tetrathiafulvalene (TTF) and hydroquinone (HQ), and the ring component is cyclobis (paraquat-p-phenylene) (CBPQT4+). No counterions are considered.

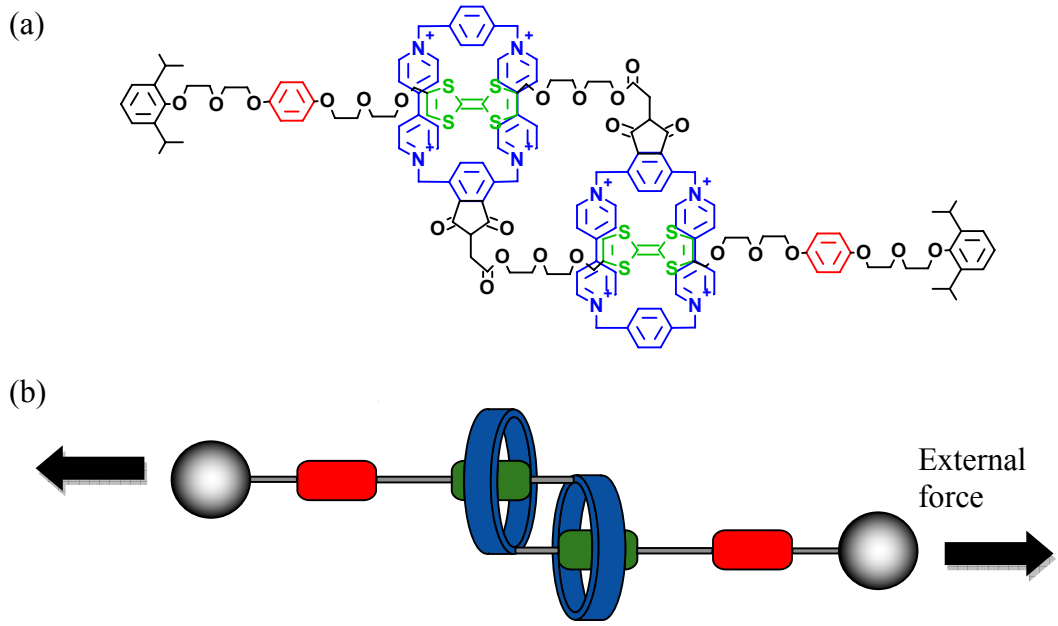

Figure 3.19 (a) Structural formula of the daisy-chain type of the artificial molecular muscle studied in this report, and (b) schematic representation of the model.

3.4.2 MD Simulations and Discussion

To see the influence of external forces, extra forces are added to one of the hydrogen atoms at the stoppers at the end of the structure. The forces are varied from 1pN to 30pN with the increment of 1pN. To show the results of the simulations, the relative distance between two ring components are measured. Representative graphs for the measured distances are shown in Figure 3.20 and Figure 3.21. The y-axis represents a relative distance between two rings and the x-axis represents time. The zero in the y-axis indicates the initial position where each ring is located at the TTF station. The positive distance is defined as the direction that two rings become apart, and negative values represent two rings become closer. For example, if no external force is applied to the structure, the measured distance between two rings will show positive values because the

rings are pushed toward the stoppers due to the electrostatic repulsion; the entire structure would be shortened. Over a certain force, however, the structure will be elongated as applied forces defeat electrostatic repulsion. The representative snapshots of the MD simulations are shown in Figure 3.22 for the applied forces of 15 pN and 28 pN.

Figure 3.20 shows the curves obtained with the applied forces less than 20pN. The first peak appears around at 2ps, and the time that the peak appears is gradually delayed with the increase of the external force. The results are reasonable because the increasing forces act opposite to the direction of the movement, and gradually prevent the repulsive movement.

Looking at the curve of 1pN, the distance repeats up and down, representing the rings to be closer and farther. At first the ring is pushed to the end of the structure due to repulsion between the ring and the TTF station, but further movement is restricted by stoppers. Then, repulsion between two TTF stations begins. As a result, the elongated structure becomes round, and the two rings become closer. When the rings become closer, however, repulsion between the rings increases again, pushing the two rings apart. The structure repeats these vibration-like motions as a result of a competition between the repulsion of two charged TTFs and that of the two rings. As the applied force increases, the period and the amplitude of the vibration decrease. The applied force plays a role to make the structure to act as a stiffer spring.

Figure 3.23 shows a sequence of the simulation every 1ps for a representative case of the force of 15 pN. The figure shows vibrating motions as explained above. Differently to the case of 1pN, which has two bumps, three bumps are seen in Figure 3.20. The increase of vibrating frequency is due to the increase of the applied force. For 15 pN,

we can see bumps at 2 ps, 5 ps and 8 ps. The corresponding configuration at these times is for the entire structure to be stretched, so the distance between two rings is farthest. On the contrary, a round structure is observed at 3 ps, 7ps and 10 ps. This is shown as valleys in the graph. At these moments, the TTF stations tend to be separated due to repulsion between two stations, so the rings are pulled closely.

The curve for 20pN, however, shows a different pattern. It has a lower overshooting about 17Å, and is stabilized quickly although the frequency of vibration increased as expected. In this case, the ring does not move to the stoppers and finds the position around in the middle where equilibrium between the external force and the electrostatic repulsion has reached.

Figure 3.21 shows curves obtained with the force between 21pN and 30pN. After 20pN, the maximum distance that the ring can be apart decreases to be less than 20Å. Before showing a totally different pattern at 28pN, the displacement converges to 13-14Å. This convergence happens because the external force is large enough to restrain the repulsive movement between the two charged TTF stations. The reason showing a depression just after 1.5ps in the curve for 26pN is tinting of the ring caused by the large force transmitted from the end of the structure. Differently from this case, the ring at the case of 21pN escapes smoothly, reaching the maximum position, because the force is not large enough to make the ring tilt.

Over the external force of 28pN, the pattern shows a sudden change; the curves end up with negative values, representing the two rings becoming closer. In this range over 28pN, the electrostatic repulsion cannot compete against the applied force anymore; therefore, the rings are pulled in the direction of the external forces. In the situation,

molecular muscles cannot produce any designed work output, losing their ability to operate. We can see the effect of the force is not shown right after the simulation begins. A bump is shown at 1ps. Although the rings move in the direction of being apart at the initial stage, they are eventually pushed closely as the influence of the force begins to be transmitted to them.

As a representative result for the large force, the sequence of the case for 28pN is shown in Figure 3.24. The conformational evolution is snapshot every 1ps. We can see that the rings are pushed in opposite directions at 1ps. The distortion of the structure, however, is shown due to the forces at 2ps. At 3ps, the rings are pulled inward, rather outward where the rings are expected to move. The rings gather closely, and the structure does not show any significant motion after 4ps. Finally, the applied force surpasses the electrostatic repulsion, which is the source for the switching process, suggesting it cannot produce work outputs anymore.

3.4.3 Conclusions

The study revealed the operation of the artificial molecular muscle that is composed by two rotaxanes can be limited by the external loadings of more than 28pN. The study also showed that the external force less than 20pN gradually delays responding time for the ring component to reach the maximum position as the force increases. The results can be used for predicting the performance and developing the design of nano/micro systems activated by artificial molecular muscles.

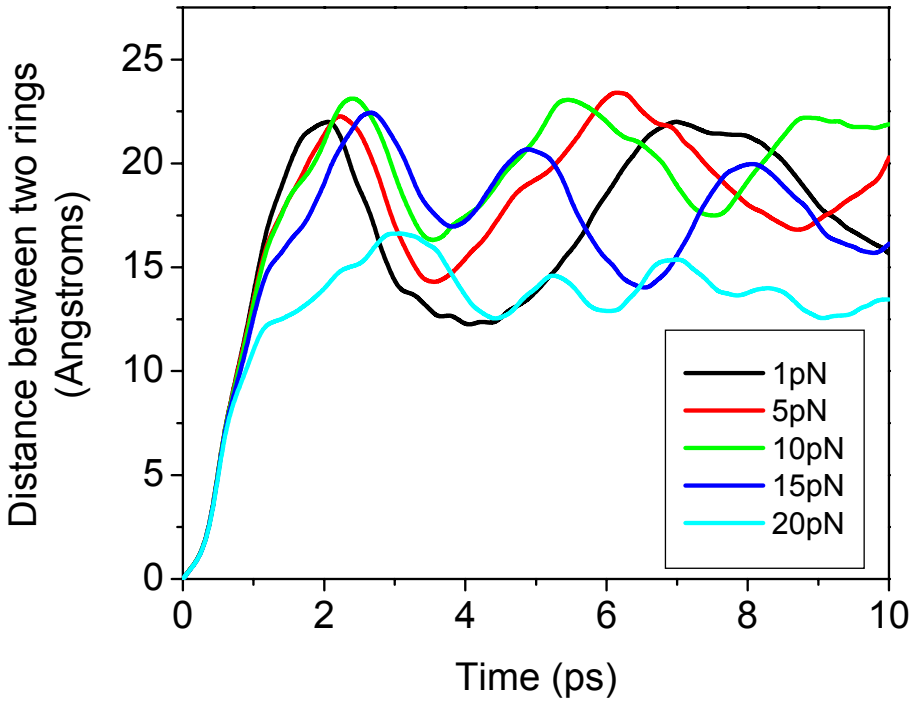

Figure 3.20 Graph of distance between two rings as a function of time; the force applied at the ends is in the range of less than 20pN.

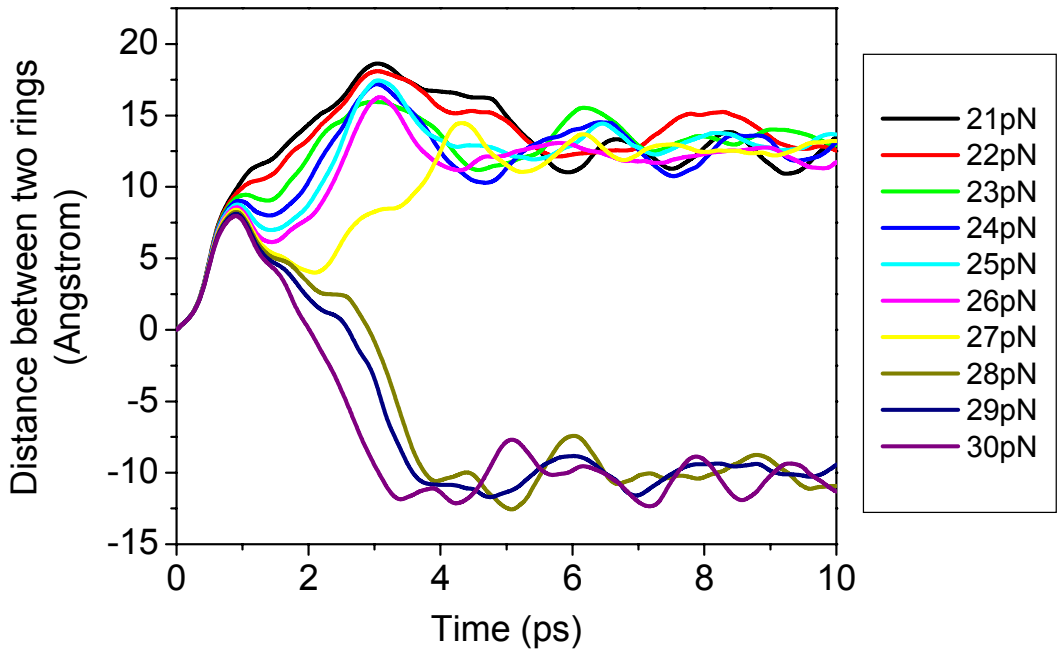

Figure 3.21 Graph of distance between two rings as a function of time; the applied force is in the range between 21pN and 30pN. The zero distance represents the distance where the two rings are initially positioned at the TTF stations. Positive distance means two rings come apart and negative distance means they come closer.

(a)

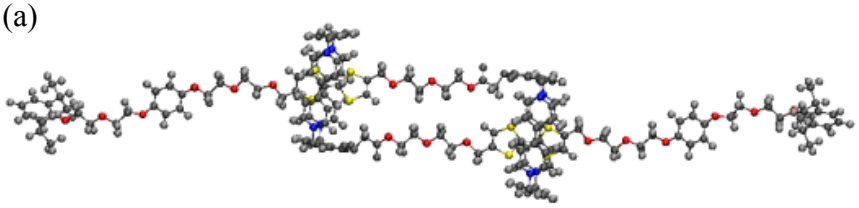

(b)

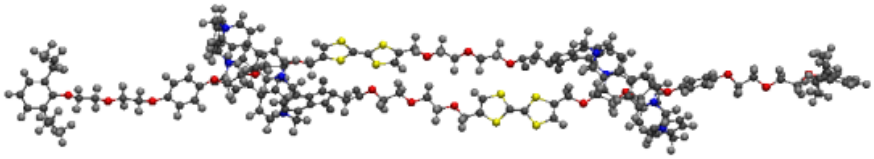

(c)

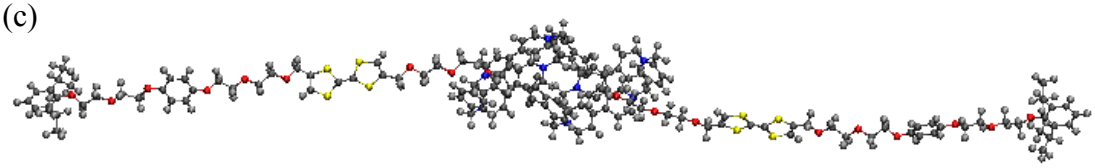

Figure 3.22 Representative results of the MD simulations: (a) initial configuration for all simulations, (b) t=10ps with 21pN: the rings are pushed away due to electrostatic repulsion between the TTF stations and the rings, and (c) t=10ps with 30pN: the rings are pulled to be closer because the effect of the applied force is much larger than the electrostatic repulsion.

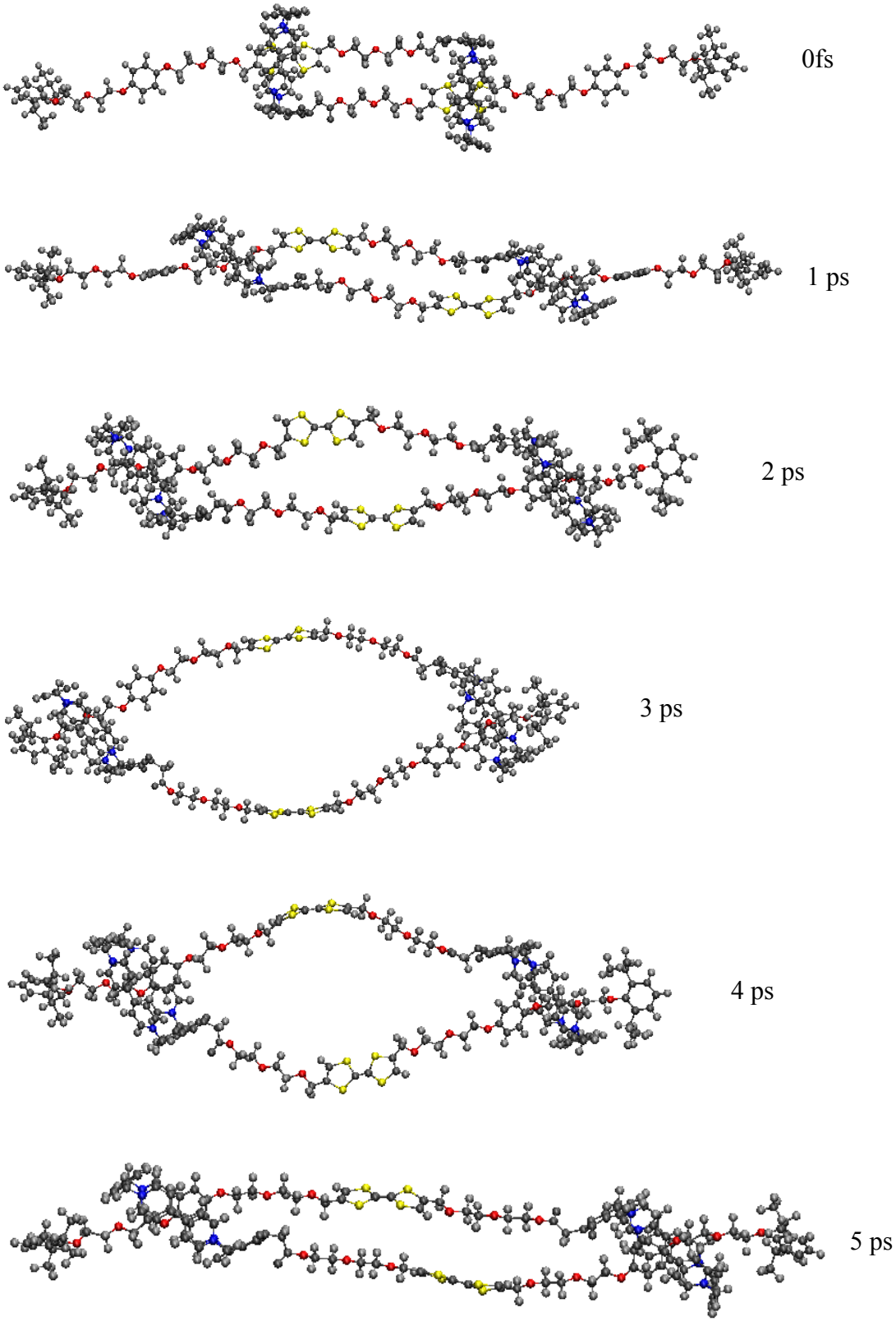
0fs
1 ps
2 ps
3 ps
4 ps
5 ps

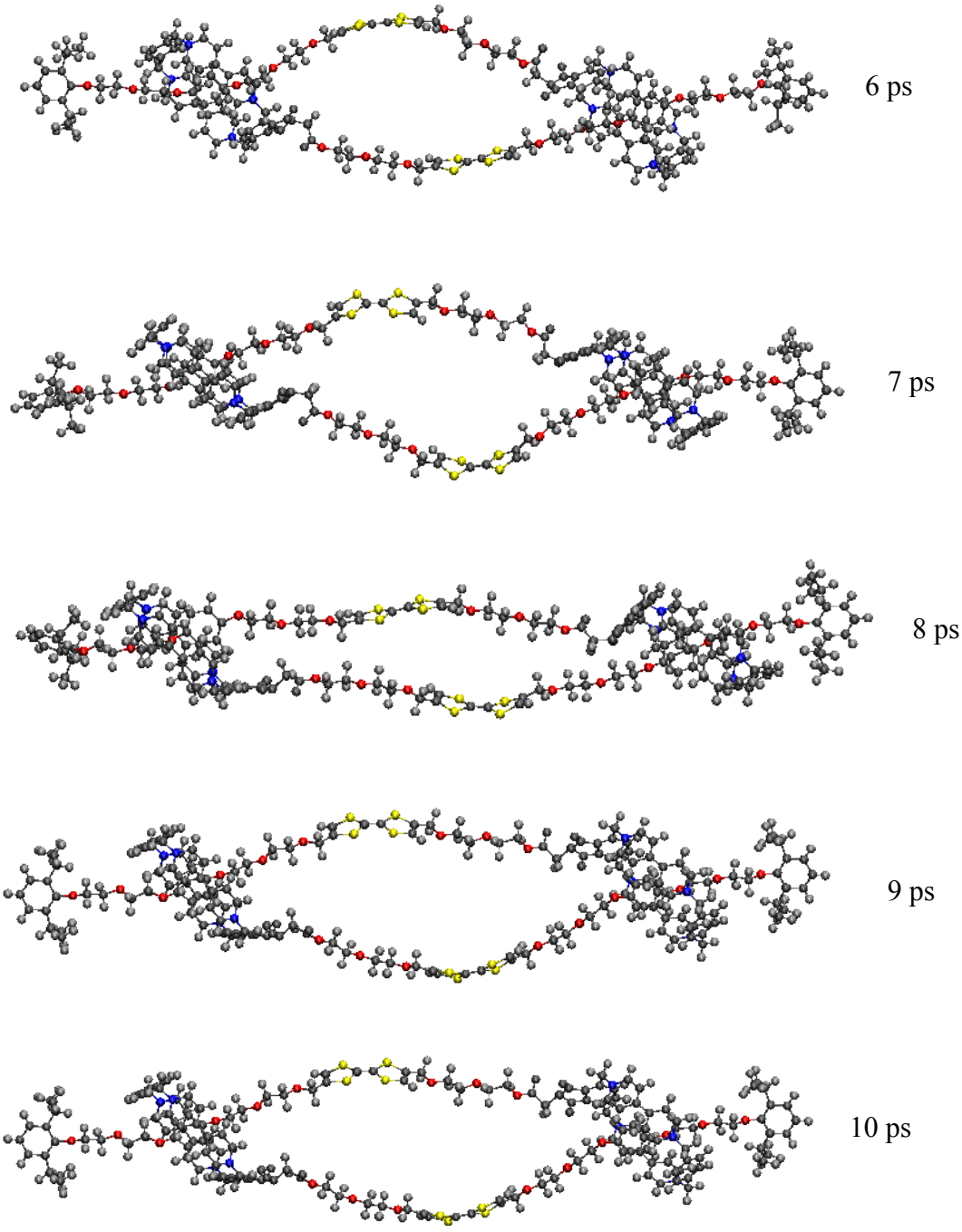

Figure 3.23 Evolution sequence at the applied force 15 pN. Even with the applied force of 15 pN, the rings are switched to the other stations and operated properly.

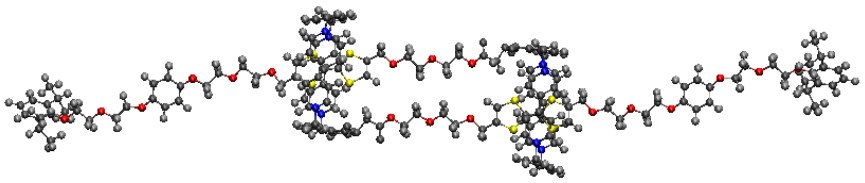

0fs

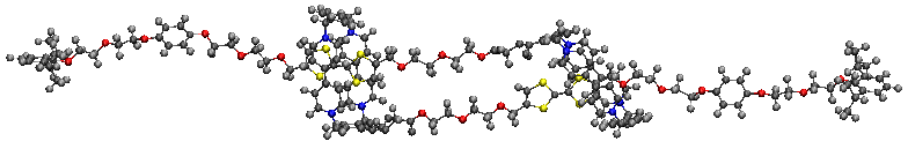

1 ps

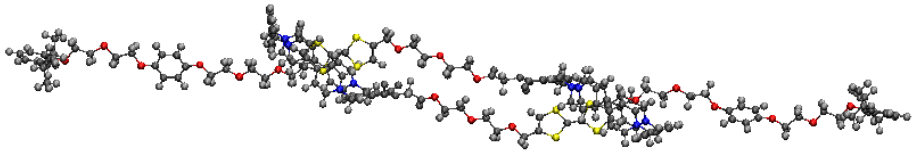

2 ps

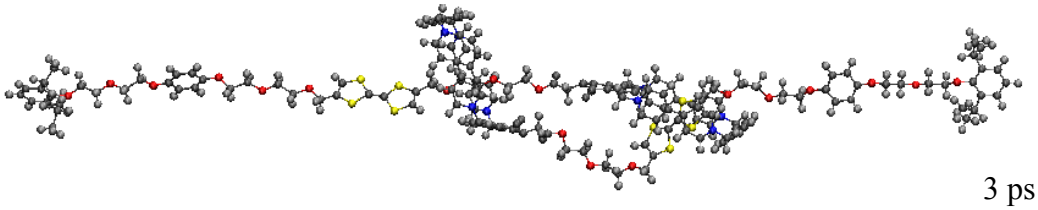

3 ps

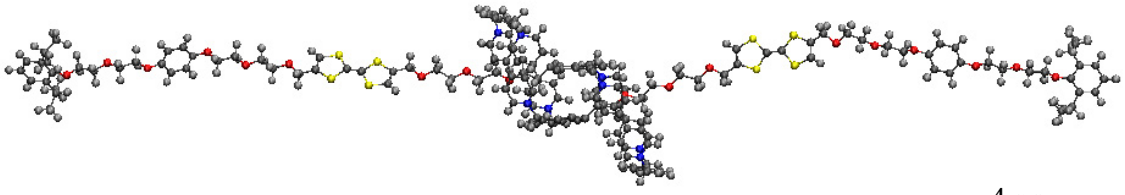

4 ps

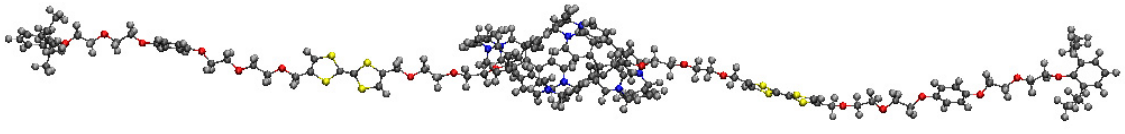

5 ps

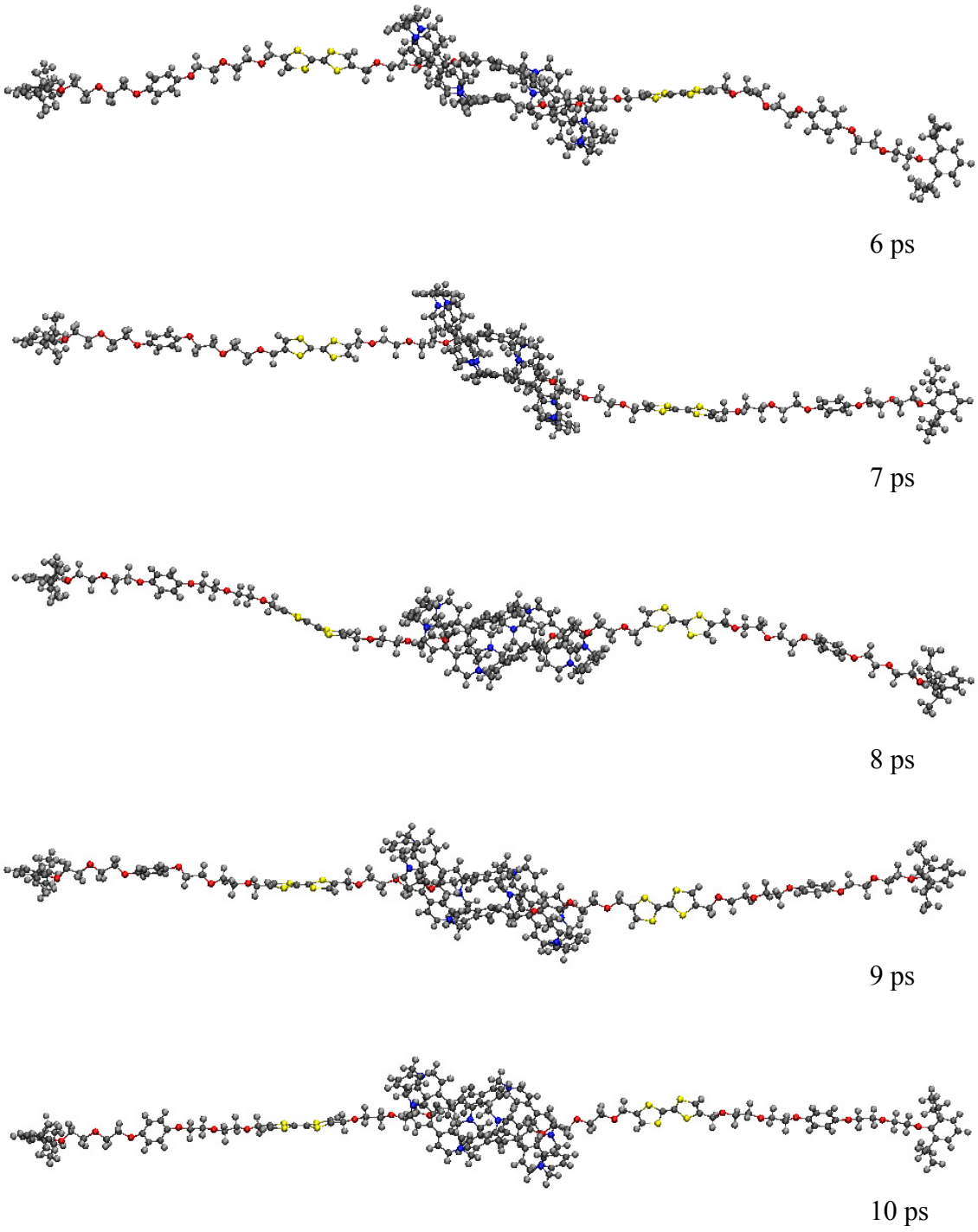

Figure 3.24 Evolution sequence at the applied force 28pN. The structure is supposed to be shortened by the movement of the rings to the other stations, but they are stretched because of the strong external force.

CHAPTER 4

Light Scattering of Healthy and Malaria-Infected Red Blood Cells

4.1 Background

4.1.1 Red blood cells

Red blood cells, or erythrocytes, are main micro-organism of delivering oxygen to the body tissue. They have biconcave and disk-like shape. A typical diameter is about 8 μm and thickness of around 2 μm. They lack a nucleus and are rich in hemoglobin, which are iron-containing biomolecules able to combine oxygen and responsible for their deep red color. Their flat shape makes the hemoglobin molecules closer to the membrane, enabling efficient transfer of oxygen. They are found at a concentration of 5×10^6 cells per microliter of blood and live for an about 100 -120 days in the body.

4.1.2. Malaria

General Information

Malaria is a serious and sometimes fatal disease caused by a parasite that commonly infects mosquitoes which feed on humans. People who get malaria are typically very sick with high fevers, shaking chills, and flu-like illness.

Here are facts about Malaria reported by CDC[105].

- 89% of the malaria deaths worldwide occur in Africa.
- Malaria is the 5th cause of death from infectious diseases worldwide after respiratory infections, HIV/AIDS, diarrheal diseases, and tuberculosis.
- WHO estimates that in 2008 malaria caused 190 - 311 million clinical episodes, and 708,000 - 1,003,000 deaths.
- About 1,500 cases of malaria are diagnosed in the United States each year. The vast majority of cases in the United States are in travelers and immigrants returning from countries where malaria transmission occurs (Figure 4.1).

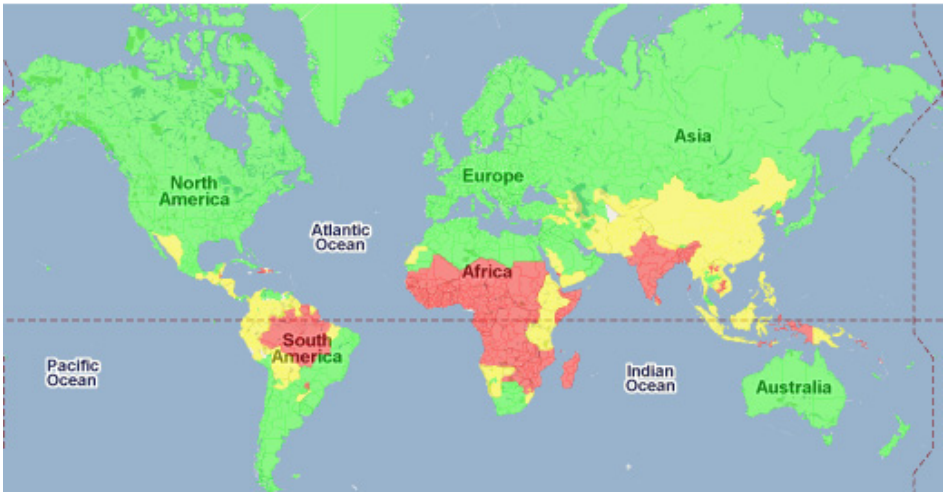

Figure 4.1 Schematic of worldwide occurrence of malaria(red: malaria everywhere, yellow: malaria local by local, green: no known malaria)[106].

Malaria parasites are members of the *genus Plasmodium* (*phylum Apicomplexa*). In humans malaria is caused by *P. falciparum, P. malariae,P. ovale, P. vivax* and *P. knowlesi*. *P. falciparum* is the most common cause of infection and is responsible for about 80% of all malaria cases, and is also responsible for about 90% of the deaths from malaria.

Life Cycle

There are two hosts contributing to the ecology of malaria: humans and female *Anopheles* mosquitoes [107]. In humans, the parasites grow in the liver and invade red blood cells. Inside red blood cells, they release daughter parasites, destroying the cell. The released parasites continue the cycle of invading other red blood cells. When the infected red blood cells are picked up by a female *Anopheles* mosquito during a blood meal, another cycle starts in the mosquito. It takes about 10-18 days for the parasites to be found in the salivary glands of the mosquito. While the mosquito takes a blood meal on humans, the parasites are injected to another human and another cycle restarts. Interestingly, the mosquito does not suffer from carrying the parasites as humans do.

Current Examining Methods

The Giemsa stain is currently the most popular method to identify malaria parasites. Prior to examination, the specimen is stained for a distinctive appearance of the parasites(Figure 4.2). Stained blood is dropped on a microscope slide and spread out by blood smear. Confirmation of malaria is made under microscope observation. It depends on the quality of reagent and the experience of examiners.

Figure 4.2 Microscopic picture of blood smear stained with Giemsa. It shows a white blood cell (on left side) and two red blood cells infected by *Plasmodium falciparum* (on right side) [108].

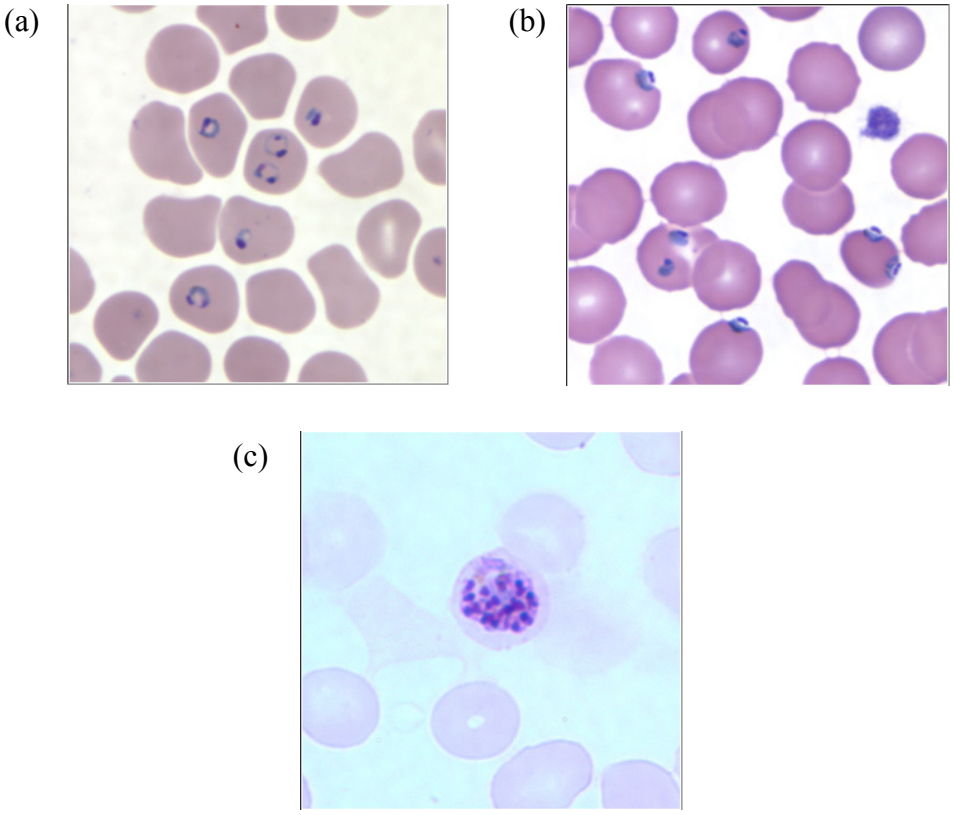

Figure 4.3 Microscopic pictures at different stages of the infected red blood cells: (a) ring stage form trophozoites of *P. falciparum*, (b) Trophozoites of *P.falciparum*, and (c) Schizonts of *P.falciparum* [109].

Progressive Stages of Infected Red Blood Cells

Figure 4.4 (a) shows the life cycle of malaria parasite after invasion. Invaded red blood cells have three stages: ring, trophozoite and schizont. Within the erythrocytes the merozoite grow first to a ring-shaped form, and then to a larger trophozoite form. In the schizont stage, the parasite divides several times to produce new merozoites, which leave the red blood cells and travel within the bloodstream to invade new red blood cells. Figure 4.3 shows microscopic pictures of stained red blood cells at different stages of infection.

While living insid the host red blood cells, the parasite exports its protein (Figure 4.4(b)). The exported protein moves out and is stored as knob structure on the membrane of the red blood cells. The interaction of exported protein and cell membrane is considered as the loss of deformability of malaria infected red blood cells.

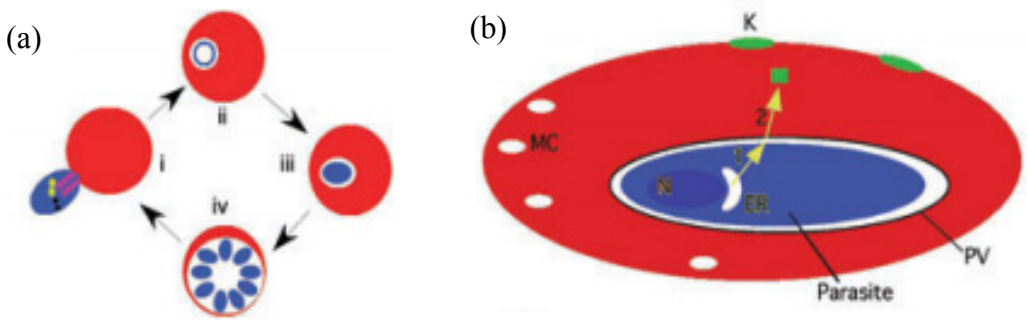

Figure 4.4 (a) Schematic of the life cycle of an invaded parasite shown in blue: (PV:white, red blood cell:red) (i) invision of parasite, (ii) ring stage, (iii) trophozoite stage, and (iv) schizont stage. (b) A schematic drawing of infected erythrocyte. The parasite is shown in blue inside the parasitophorous vacuole (PV). The exported protein (green) and knob structures are shown[110].

Changes of Red Blood Cells by Infection

In the report by Park et al[111] the permanent loss of deformability was observed after fever episode (increase of temperature) and was explained by accelerating parasite protein exportation to the membrane. In this paper they measured thermal fluctuations of the membrane for healthy and infected red blood cells by diffraction phase microscopy (DPM). DPM is operated by the mechanism of laser interferometry, and the device they used in the experiment has nanometer and millisecond resolution. They observed the decrease of fluctuation and increase of shear rigidity for the infected red blood cell.

4.2 Motivation

Malaria is a serious and fatal disease transmitted by infected *Anopheles* mosquitoes that feed on humans. Approximately 350 to 500 million cases of malaria are reported and more than one million people die from malaria annually, mostly occurring in Africa[112]. Conventional diagnosis of malaria relies on microscopic examination of Giemsa-stained blood smears, which is commonly used in the field. Unfortunately, the method requires invasive acquisition of blood samples and this usually comes at the price of high cost, patient annoyance, and significant training for health workers. The processing of blood samples also demands a complex logistics chain and increased time delay in diagnosis. Therefore, the development of methods that come with low cost and ease of use is crucial. A non-invasive method is considered as an innovative solution to overcome disadvantages of the conventional methods.

For the non-invasive diagnosis, different spectroscopic methods can be considered such as infrared, raman and elastic scattering spectroscopy. However, infrared

spectroscopy would be limited for application of non-invasive diagnosis in living bodies because of strong absorption in water. Raman spectroscopy could be an alternative, but it is mainly used for the analysis of chemical change in infected red blood cells[113] and might have a limit in application due to a very weak signal. In this chapter, we measure the signal using elastic scattering light and examine whether it can distinguish the healthy and *Plasmodium falciparum* malaria parasite invaded red blood cells.

Elastic light scattering is based on the different scattering pattern of photons due to the discontinuities of the refractive index. Therefore, it can be used to distinguish particles that have different structure or material characteristics such as size, morphology and chemical composition. For example, particles were able to be differentiated according to their size by elastic light scattering[114].

Light scattering is a common phenomenon in nature around us. The closest examples may be that the sky looks blue because the wavelength of blue is scattered more by particles in air, and that the sky at sunset is red because the blue wavelengths are scattered, thus only the red wavelength is seen. Recently there are many efforts to bring light scattering to use in biomedical researches. The applications range the detection of diseases[115], optical biopsy[116], and imaging of tissue[117] or blood[118]. The study about diagnosis of breast cancer using elastic light scattering has been performed[119], and the study has shown that elastic light scattering can monitor the biological process that accompanies biochemical and morphological changes[120].

The red blood cells invaded by the *P.falciparum* malaria parasite experience significant modification in the structural, mechanical and biochemical properties [111, 121-124]: morphological changes from biconcave shape, reducing membrane fluctuations

and elasticity, and decrease of hemoglobin (Hb) concentration. We considered elastic light scattering is capable of detecting these changes and studied whether it can potentially be used as a diagnostic tool for the malaria infection.

Light scattering of red blood cells has been widely studied in experiments [125-127] and numerical simulations [128-130]. Recently light scattering of malaria parasite invaded red blood cells has been reported. Serebrennikova's group studied UV-visible light spectroscopy for the different stages of *P.falciparum* red blood cells with the zero forward direction of the incident light[131]. Park's group studied light scattering of individual *P. falciparum* red blood cell with the combination of experiment and numerical calculation[122]. With the intention of non-invasive diagnosis in mind, we focused on a comparison of light scattering for healthy and *P.falciparum* parasitezed ring stage red blood cells, because ring stage *P.falciparum* red blood cells possibly can be detected on blood vessels near human skin. We studied light scattering at different angles in the forward direction as well as in the backward direction.

4.3. Experimental Setup and Sample Preparation

4.3.1 Instrumentation Design

The optical setup consists of a lamp, a spectrometer, a lens, optical fibers, and a variable aperture (Figure 4.5). The optic components are aligned vertically. The advantage of vertical setup over horizontal setup is that a flat side of the container for the liquid sample is able to be used. In case of horizontal setup, a cylindrical test tube is used to contain the liquid sample, and the incoming and outgoing beam should pass through the curved side of the tube, whereas the round shape can easily affect the results. For

example, it is hard to obtain symmetric data for both positive and negative angles unless the test tube is precisely positioned at the center of the zero beam direction. On the other hand, the vertical setup allows the sample container to be placed freely on the x-y plane.

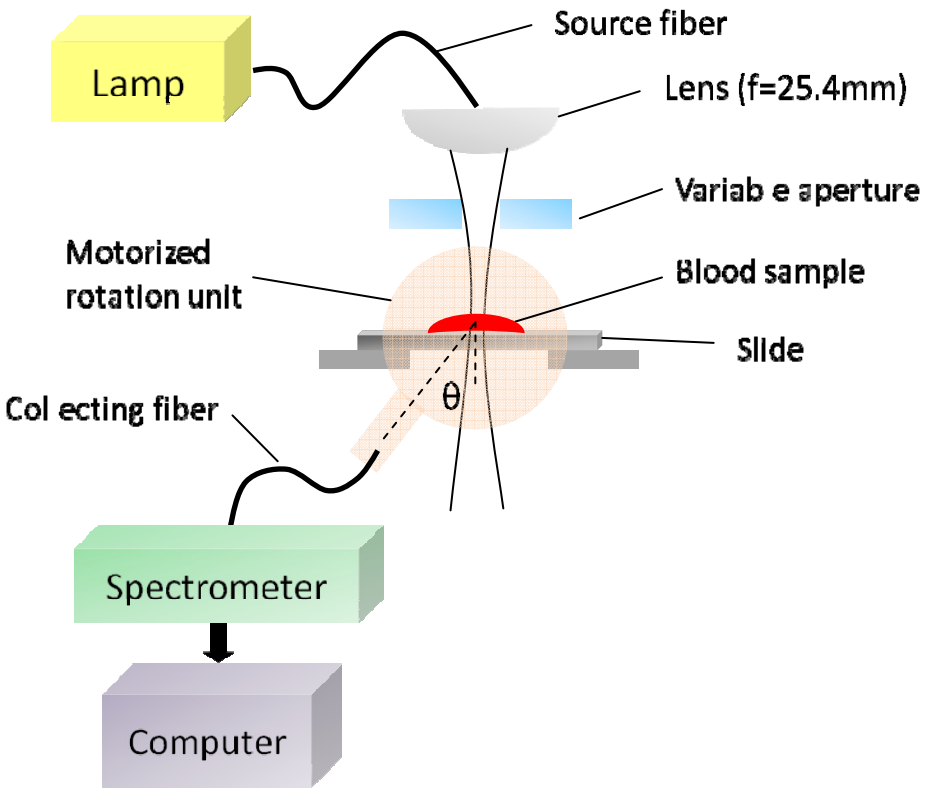

Figure 4.5 Schematic of optical setup.

A broadband light source delivered through the 400 μm optic fiber is imaged on the test space by a plano-convex lens (f=25.4mm). A variable aperture is used to control the diameter and the intensity of light. The variable aperture is adjusted so that the source of light passed through the test space is not directly illuminated into the collecting fiber. The lens is located about 70 mm away from the test space, where the beam is focused on

the test plane. The collecting fiber is attached to a motorized rotator, whose angles are controlled by computer. By changing the angle of the collecting fiber, the scattered light from the test space is measured at various angles. The collecting fiber is connected to a spectrometer.

The glass slide on which the blood sample is dropped is placed on the beam waist, where the beam is focused. The vertical position of the glass slide should be at the center of the rotation unit so that the scattering angle can be measured correctly and the symmetric data can be obtained for both the positive and negative angles. To place the slide at the correct position, the light beam is attached to the rotation unit and it is ensured the beam does not move as the angle changes.

4.3.2 Data Collection

The scattering intensity of particles in the test space is calculated by

$$I_{particle} = \frac{I_{sample} - I_{backgraound}}{I_{reference}} . \quad (4.1)$$

$I_{reference}$ is measured with the detector aligned at the zero degree to measure the spectrum of the source light. $I_{background}$ is measured at each angle including all the components such as the medium and the container except the particles or the sample. I_{sample} is obtained with the particles or the sample at each angle. The calculated intensity is normalized by the area under the curve in order to remove the effect of the number of particles.

4.3.3 System Verification with Polystyrene Particles and Mie Theory

To verify the operation of the system, the scattering pattern of polystyrene spheres (n=1.59) is compared to numerical calculations from Mie theory. In the Mie theory, the scattered intensity of particles is derived from Maxwell's equations about a spherical particle subjected to an electromagnetic field, and is reviewed in Appendix C. Validation is performed by comparison of patterns with the calculations of Mie theory about spherical particles of which the size and the refractive index are known.

The mean diameter of polystyrene spheres 7.9 μm is chosen considering the diameter of red blood cells is about 8 μm. The size distribution of the particles is assumed with a 5% Gaussian variation on the base of the data from the manufacturer. The particles are diluted with water and the concentration is made into about 0.0006% solution in order to ensure the single-scattering event. Data is collected at angle of 12˚ and 14˚. Figure 4.6 shows the experimental data (blue line) and the Mie calculations (red line). From the figure, we can see the experimental results and the Mie calculations match well. At 12˚, there exists a valley in both lines at the wavelength of 650 nm. When the angle is increased to 14˚, the valley moves to 615nm. The results show the valley and the peak are shifted as the angle is changed, suggesting the system is able to detect scattered light from particles.

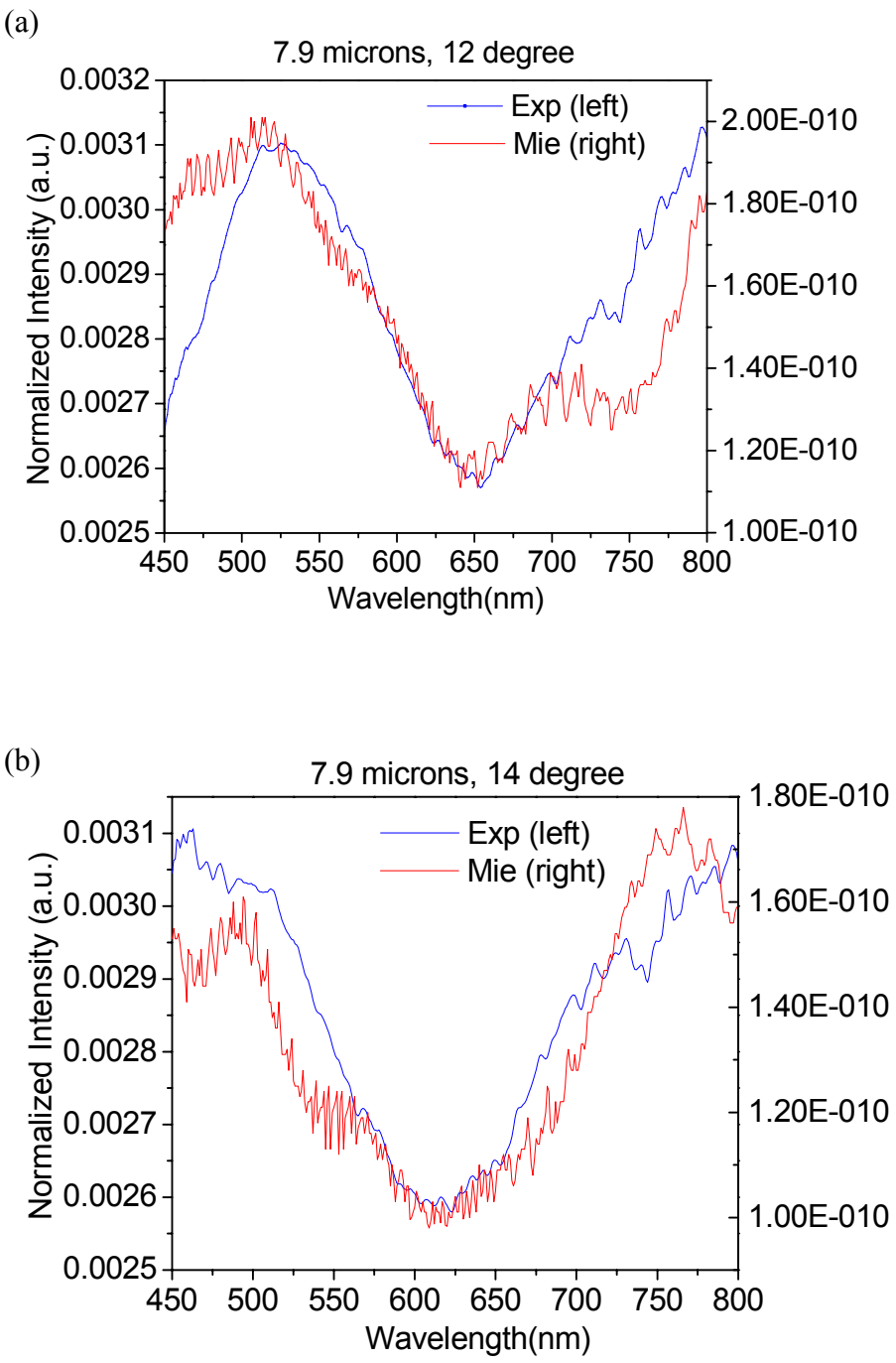

Figure 4.6 Graph of light scattering of polystyrene spheres as a function of wavelength.

4.3.4 Preparation of Blood Samples

Preparation of the healthy and parasitized red blood cell samples were conducted at Malaria Branch, Centers for Disease Control and Prevention, Atlanta. The laboratory-adapted W2 strain of *P. falciparum* was used in this study. The blood-stage parasites were cultured as described in the reference[132] in RPMI 1640 medium supplemented with 10% heat inactivated O+ human serum, 1 mg/ml of gentamicin, 36 mM hypoxanthine, 31 mM HEPES, and 25 mM sodium bicarbonate. The parasite cultures were adjusted to 2% parasitemia with predominant ring stage parasite and 50% hematocrit and the healthy red blood cells used as a negative control were also adjusted to 50% hematocrit. The samples with the 50% hematocrit and the samples further diluted with PBS were used for testing.

4.4 Experimental Results and Discussion

4.4.1 Forward Light Scattering

First, forward scattering from blood samples was measured. It is known that the intensity of forward scattering is much stronger than backward scattering. We tested for the diluted samples with PBS (phosphate buffered saline) and the samples without dilution. Figure 4.7 shows representative results of the scattering pattern from diluted healthy and ring stage *P.falciparum* blood samples at different angles. From Figure 4.7(a) the difference in the signal between healthy and ring stage samples is clearly evident. Although the pattern is similar at all observed angles, the intensity of ring stage blood sample is weaker below the range of about 600 nm and stronger above 600 nm. The difference of the intensity becomes larger as the wavelength of light increases or

decreases. The doublet at 540 nm and 575 nm, which is a well-known characteristic of oxy-hemoglobin[133], is clearly shown in the figure. Figure 4.7(b) shows the change of the intensity according to the change of the angle for each normal and ring state. We can see the difference in scattering pattern of blood samples as the angle varies. A larger change in intensity is observed for the ring stage blood cells and the difference is more clearly seen at the range of 450-500 nm and over 700 nm. Although the shift of peaks or valleys is not seen at the spectra, the pattern can be clearly differentiated. The different pattern can be explained by the change of the chemical composition due to the increase of the digestive wastes of the parasite with consumption of hemoglobin.

Figure 4.8 shows representative results of the scattering pattern from blood samples without dilution. From Fig. 4.8(a) we still can see the difference between normal and ring state blood sample even without dilution, suggesting the possibility of in-vivo detection using light scattering. In Fig. 4.8(b), spectra at the different angles are shown for normal and ring stage blood cells. The cases do not show much difference according to the different angles. The spectrum is affected by absorption and scattering from particles. The effect of scattering seems weakened due to multi-scattering from a larger number of red blood cells when the sample is not diluted.

4.4.2 Backward Light Scattering

Backward scattering is useful for non-invasive diagnosis because the source and the detector can be placed on the same side when the technique is applied on human skin. We performed experiments that measure the scattering spectrum at the same side of the incident light. The intensity of scattered light is strong as the angle decreases at both

forward and backward directions. Unlike forward scattering, there is a limit in decreasing the angle of the detector near the zero degree because the detecting fiber should be placed not to block the incident light. The angle 17˚ is the smallest angle for the measurement of backward scattering in the setup.

Figure 4.9 shows the results of backward scattering from the blood samples at 17˚. We tested the samples with dilution and without dilution. Fig. 4.9(a) shows the results for the sample diluted with PBS. The different spectrum is seen between healthy and ring stage blood samples. The intensity of the ring stage blood cells is low in the range below about 600 nm, but high above 600 nm. The doublet due to oxi-hemoglobin is shown for both normal and ring blood samples, but it is more clearly seen at the healthy cells. This seems because hemoglobin has been changed to digestive waste of the malaria parasite for the ring stage blood cells. Fig. 4.9(b) is the spectra of the samples without dilution. The intensity of the ring stage blood cells is weaker than that of the normal blood cells below 630nm and above 750nm but stronger between 630nm and 750nm. In addition, the peak is shown at 640nm for the normal blood cells, but at 670nm for the ring stage blood cells. The result showing difference and shift of the peak is promising for the use of elastic scattering spectroscopy as a non-invasive diagnostic tool for the malaria disease.

4.5 Conclusions

We report that healthy and malaria-infected red blood cells show a different spectrum under elastic light scattering in both forward and backward directions. In particular, the result that a different signal is observed from backward scattering without any dilution indicates that elastic light scattering can be a valuable tool in the non-

invasive diagnosis for malaria. In addition, the results suggest that elastic light scattering can be used to detect other red blood cell related diseases through measurement of structural and biochemical changes in red blood cells. Further studies, such as how scattered light interacts with skin tissue or blood vessels, are required to achieve the development of non-invasive diagnosis.

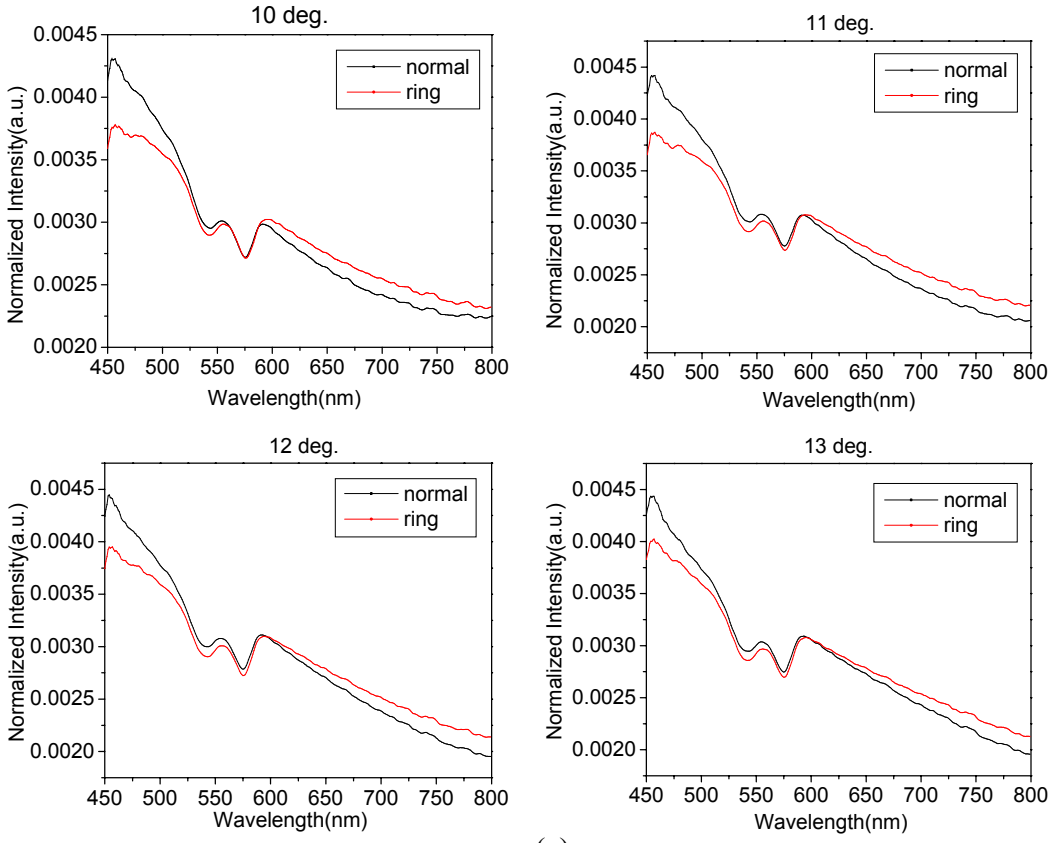

(a)

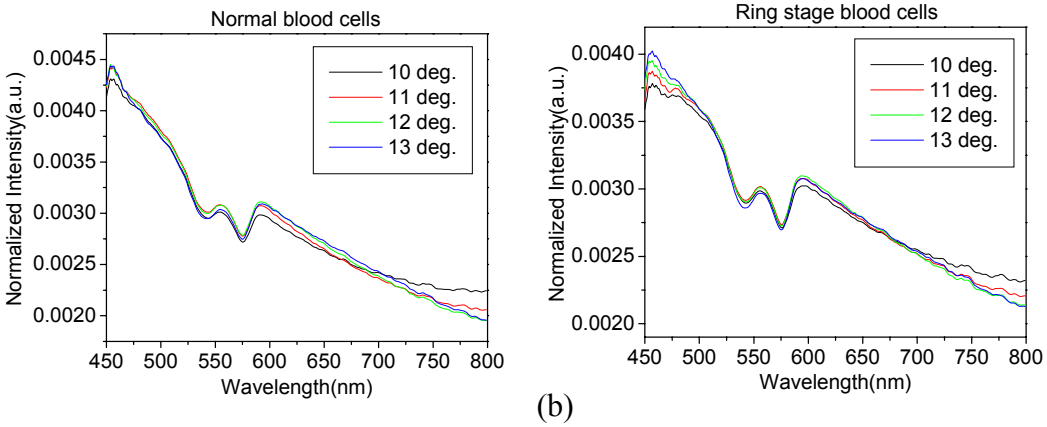

(b)

Figure 4.7 Forward scattering of healthy and ring state red blood cells, which are diluted with PBS. (a) Comparison between healthy and ring stage blood cells at a specific angle. (b) Comparison spectra at different angles.

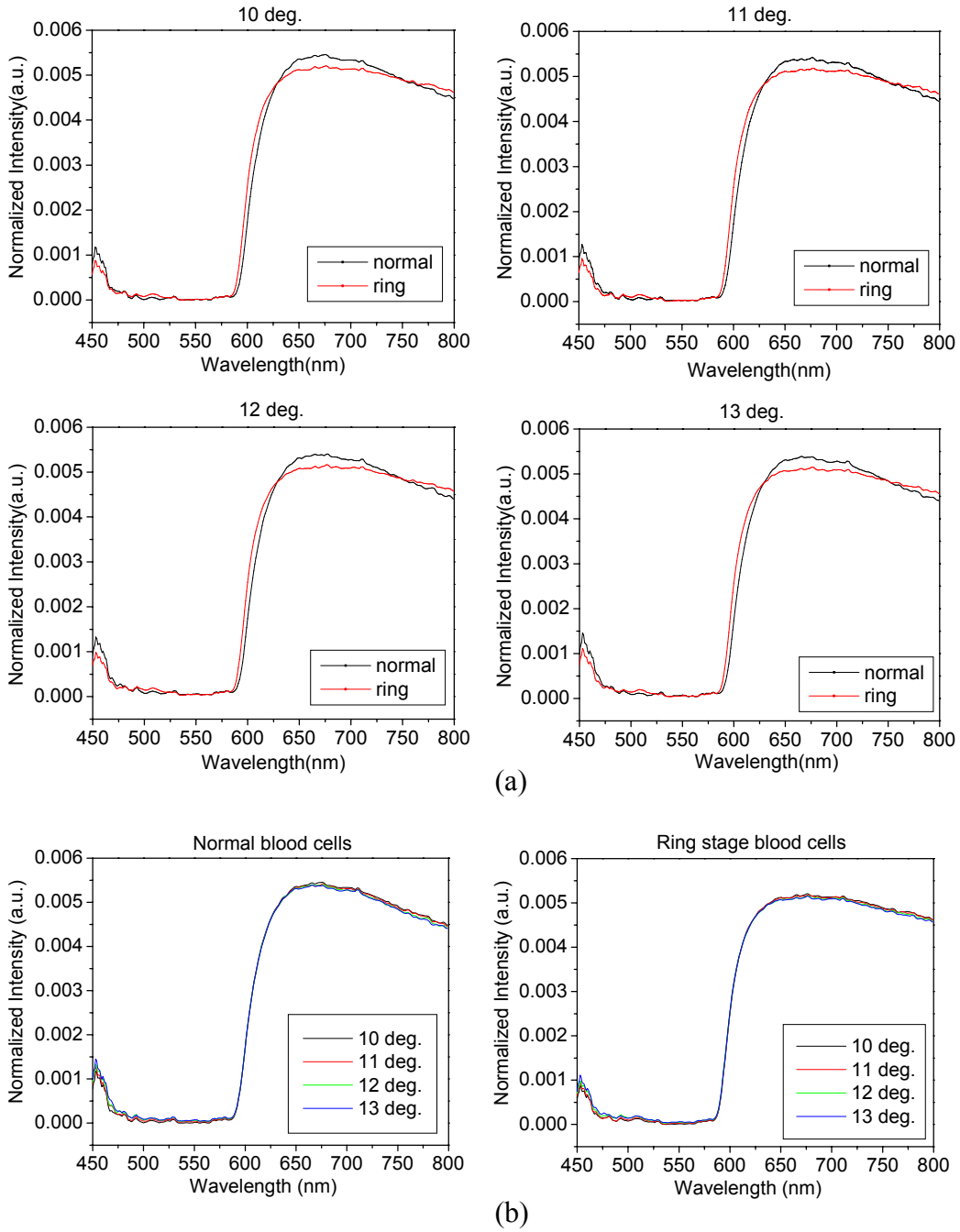

Figure 4.8 Forward scattering of healthy and ring state red blood cells with no dilution. (a) Comparison between healthy and ring stage blood cells at a specific angle. (b) Comparison spectra at different angles.

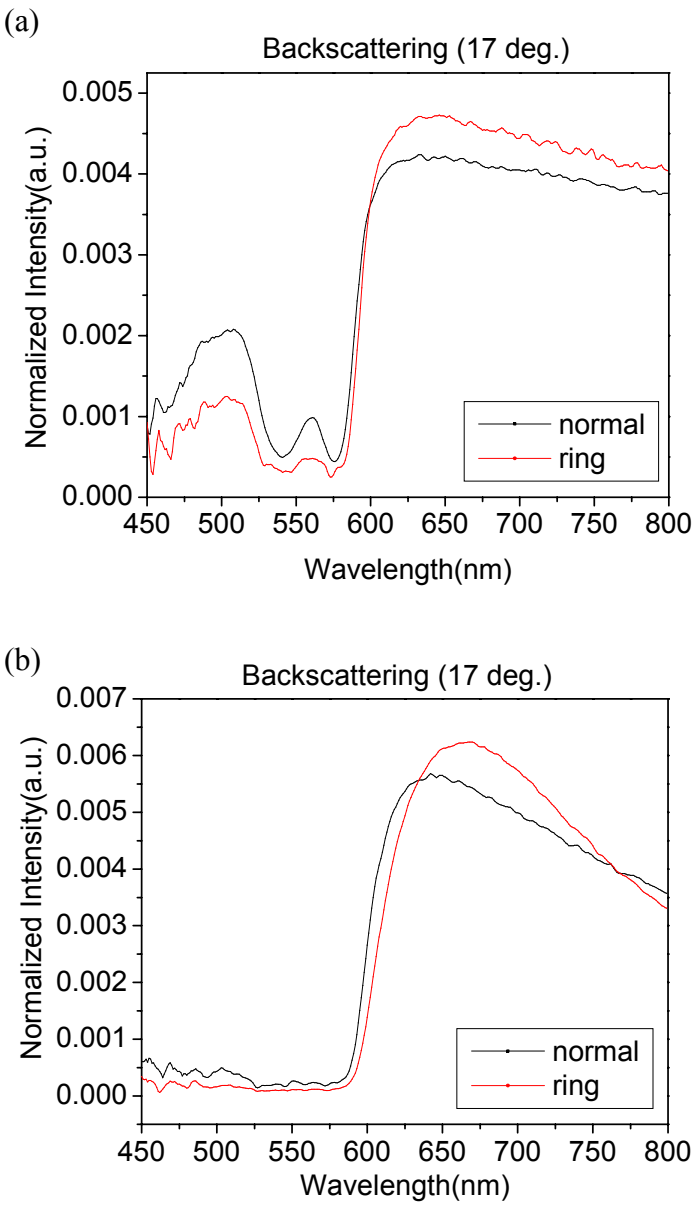

Figure 4.9 Backscattering of healthy and ring state red blood cells: (a) Diluted with PBS, and (b) No dilution.

CHAPTER 5

Conclusions

In the dissertation, the relation of force and micro/nanostructures is focused on the subjects of self-assembled structures on surfaces, functional molecules, and biomaterials. Diffusion of atoms on surfaces is caused by the minimization of energy of the system; changes in energies of the system induce a driving force to move atoms, letting them to formulate a certain pattern on the surface. From the topic of ion beam bombardment, diffusion derived by the minimization of energies such as surface energy and wetting energy plays an important role in the self-assembled structures. For example, directional supplies of diffusing atoms are a key to the hexagonal formation. The mechanism of how self-assembled structures are ordered was studied in detail. Then, how forces can influence the performance of artificial molecular systems was studied. Lastly, the application of changes in mechanical properties was studied in biomaterials; especially, how the phenomenon that the red blood cells infected by malaria become hard can be used for the development of non-invasive diagnostics.

5.1 Achievements and Contributions

The achievements and the contributions of the studies are listed by topics as follows.

Model I about ion bombardment

- Numerical simulations from the model enabled the observation that ripples evolve into dots. As a result, the dots line up and make chains. The transition from ripples to dots suggests a useful mechanism for the formation of ordered structures.

Model II about ion bombardment

- A new term for the shadow effect incorporated in the model describes accelerated smoothening at shadow zones due to weakened sputtering.
- Numerical simulations showed the formation of chains, which are mainly affected by the added shadow effect term. Different from the previous simulations, ordered dots are obtained without the appearance of ripples, which is consistent with experiment.

Model III about ion bombardment

- The unique morphology of separated islands, rather than highly packed, was represented in the numerical simulations by introducing the term of wetting energy. Contrary to the previous models, a flat surface and islands were distinguished. Thus, directional supplies from the surface to the islands were able

to be realized in simulations. As a result, it was revealed that directional supplies are the main mechanism for the appearance of a hexagonal formation in preferential sputtering. In addition, it was revealed that wetting energy plays a role to prevent coarsening of islands.

- In the simulation, the shadow effect was realized by limiting deposition at shadow zones. Owing to shadow effect, the islands moved toward the direction of the incident beam; finally, the orientation of the hexagonal formation was perfectly aligned perpendicular to the incident direction. The result suggests that the mechanism of forming chains is related to the shadow effect.
- The sputtering and deposition terms were included in the model. The sputtering term keeps the size of the islands constant by balancing with supply. Discrete deposition by adding random numbers during the simulation enabled directional supplies of atoms on the surface; the directional supplies were able to be expressed by the combination of discrete deposition and wetting energy. The increased heights by deposition were suppressed by wetting energy, which favors lower heights. Thus, atoms should diffuse randomly and were absorbed into near islands. This mechanism describes the directional supplies well.

Rotaxane-based molecular motor

- The switching process, which is a key mechanism to play as a motor, was modeled at the atomic scale. Multi-scale simulation was used: quantum mechanical calculations for partial atomic charges, and molecular dynamics (MD) simulations for dynamic movements.
- The simulations revealed the ring at the TTF station is stable regardless of free or constrained conditions. It is known that the TTF station is stable by experiments, but verification by MD simulations is meaningful. Although ab initio calculations were successfully used as a simulation tool in other studies, MD simulations allow the simulation time to be shortened and morphological evolution to be observed.
- The simulations also revealed that the molecular motor may not operate properly in a constrained situation. In the simulation, structural deformation played an important role in ring switching. If the structure is constrained not to deform, the ring was not able to switch to the other station. The results suggested caution is required to allow flexibility of the structure in application.

Artificial molecular muscle

- The influence of external forces on a displacement and a responding time was studied, and the simulations revealed the maximum force that the artificial molecular muscle can withstand. Knowledge of the limit of forces will be helpful in the design of functional microsystems operated by molecular muscles. For

example, the simulation can provide the number of molecular muscles needed to achieve a desired displacement.

- In the simulations, the unique motion of vibration in the structure was observed during the switching process, which is difficult to observe in experiment.

Light scattering on red blood cells

- Experiments revealed that white light in the visible range can be used to distinguish normal and malaria-infected red blood cells. Different spectra of light scattering are obtained in both the forward and backward directions.
- The difference in spectra between healthy and malaria infected cells in the backward direction is promising for the development of non-invasive diagnostics, because a future tool can be used on human skin to catch the backward signal.

5.2 Future Works

Models about ion bombardment

- Parametric studies are needed. The parameters include the effect of many variables such as the energy, the fluence, and the incident angles of ion beams. For example, the experiment showed that the size of the islands decreases as the angle of the beam is increased. The influence of the incident angle needs to be defined in the model. After defining the relationship between parameters and environmental variables, one also needs to consider how the parameters in the model can be determined by experiment.

- The equation representing wetting energy needs to be verified. The form of the equation used in the study is reasonable, showing a decrease in energy as the layer thickness is increased. The exact form, however, is not verified; for example, the value of the power α_w, which defines the level of decrease, is not known. One could calculate the distribution profile of wetting energy as a function of the thickness by MD simulations; highly mobile Ga atoms are modeled on the solid GaAs substrate, and then the energy at discrete levels along the height can be calculated.

Molecular motors and machines

- The efficiency of rotaxane is an interesting question. Studies can be focused on how much chemical energy is required to convert the electric states from neutral to charged states, and how much work is produced by the switching process. We have already calculated the change of energy associated with oxidation of the TTF station, which is 127 kcal mol^{-1}, by the following method. We first calculated the potential energy at the stable ring position before oxidation. Then, we used quantum mechanical calculations to get atomic partial charges after oxidation, and calculated the potential energy at the same ring position. Recent experiments have shown that the oxidation energy of similar systems, but in a liquid, is about 65 kcal mol^{-1}[134]. The higher value in our calculation may be attributed to a difference in the molecular structure we studied, and the shielding effect of the liquid, which reduces the measured energy compared to our calculations in a vacuum. We may try simulations including a liquid and compare the result with

the experimental result. The amount of work produced by the switching process can be calculated with a load bearing system.

- Simulations can be done for different kinds of molecular systems. For example, the station can be switched to a different molecule such as DNP (dioxynaphthalene). And, a linearly-chained molecule, different from the daisy-chained type we studied, may be studied using the same technique for comparison of performance under load conditions. Moreover, it would be interesting to study the influence of forces for totally different systems, such as molecular shuttles and molecular elevators.

Light scattering on red blood cells

- Theoretical analysis is needed to interpret the experimental results of light scattering difference in healthy and malaria infected red blood cells. Although theoretical analysis is not easy due to the random orientation in liquid and the anisotropic concave shape of red blood cells, Mie theory will be useful for analysis, assuming red blood cells as a volume equivalent sphere.
- We focused on the visible range of light in the experiments, but the range can be expanded to ultra-violet and near infrared. It is known that the absorption of hemoglobin is strong below 600nm. Absorption can be an obstacle in observing scattering patterns. On the contrary, the pattern itself can indicate changes. For example, after the parasite invades the red blood cell, hemoglobin is consumed, which can largely affect the ultra-violet spectrum.

- Tests of different concentrations and different stages of infected cells would be helpful toward the development of future non-invasive diagnostics. In the experiment, the tested sample was at 10% concentration of infected cells and at the ring stage. Results obtained at different conditions would be helpful to understand the results from the patients who show variance in the level of the infection. Because the technique will be used on human skin, results close to physiological conditions, which can be observed near skin, will be useful.

APPENDIX A

Upward Flux by Erlish-Schwoebel Barrier

While diffusing on the terrace, the atom cannot jump down to a descending step because of an energy barrier at the end of the terrace. On the other hand, the atom that meets an ascending step sticks. Due to the energy barrier, the overall current heads uphill.

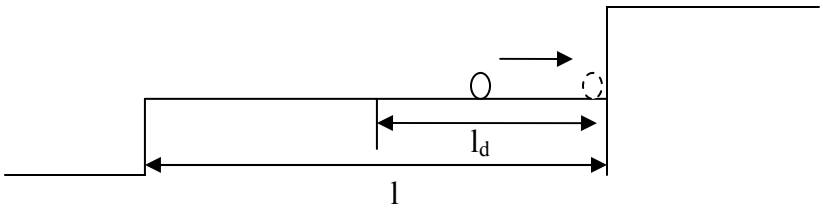

Consider an atom on a terrace in steps of surfaces. l is the length of a terrace. l can be expressed as $1/\nabla h$ if we assume the slope is small. l_d is the length of diffusion of the atom. If the slope is very small, l_d becomes less than l. In this case, only atoms within l_d contribute to a current to uphill (Figure below). We can say probabilistically that an uphill flux is $J \sim (l_d / l) \sim l_d \nabla h$. If the slope is steep, l_d becomes larger than l. In this case, all atoms on the terrace contribute to the uphill current. Therefore,

$J \sim l \sim (1/\nabla h)$. We consider two cases of gentle and steep slopes in the continuum equation. Thus, the current can be found by the harmonic mean,

$$\frac{1}{\mathbf{J}} = \frac{1}{l_d \nabla h} + \frac{1}{\frac{1}{\nabla h}},$$

which is summarized as

$$J = \frac{l_d \nabla h}{1 + l_d \left(\nabla h\right)^2} \sim \frac{\nabla h}{1 + l_d \left(\nabla h\right)^2}.$$

APPENDIX B

Linearization and Fourier Analysis

The 2D partial differential equations of two layers are

$$\frac{\partial h}{\partial t} = -\eta\left(1 + b\frac{\partial^2 h}{\partial x^2}\right) + R\left(\gamma + d\frac{\partial^2 h}{\partial x^2}\right)$$

$$\frac{\partial R}{\partial t} = (1-\phi)\eta\left(1 + b\frac{\partial^2 h}{\partial x^2}\right) - R\left(\gamma + d\frac{\partial^2 h}{\partial x^2}\right)$$
$$-\kappa\frac{\partial}{\partial x}\left\{R\frac{\partial}{\partial x}\left(\frac{\frac{\partial^2 h}{\partial x^2}}{\left(1+\left(\frac{\partial h}{\partial x}\right)^2\right)^{\frac{3}{2}}}\right)\right\} + D\frac{\partial^2 R}{\partial x^2} - s\frac{\partial}{\partial x}\left\{R\frac{\frac{\partial h}{\partial x}}{1 + l_d\left(\frac{\partial h}{\partial x}\right)^2}\right\}.$$

Let $h = h_0 + h_1$, $R = R_0 + R_1$. $h_0 = -\phi\eta t + const.$, $R_0 = (1-\phi)\frac{\eta}{\gamma}$, which are the solutions for the flat surface without perturbation. They are found from the equations $\frac{\partial h}{\partial t} = -\eta + R\gamma$ and $\frac{\partial R}{\partial t} = (1-\phi)\eta - R\gamma = 0$. And $h_1 = \hat{h}_1 \exp(iwt + i\mathbf{kr})$, $R_1 = \hat{R}_1 \exp(iwt + i\mathbf{kr})$.

Now plug $h = h_0 + h_1$ and $R = R_0 + R_1$ into the partial differential equations. The first equation is

$$-\phi\eta+\frac{\partial h_1}{\partial t}=-\eta\left(1+b\frac{\partial^2 h_1}{\partial x^2}\right)+(R_0+R_1)\left(\gamma+d\frac{\partial^2 h_1}{\partial x^2}\right)$$
$$=-\eta-b\eta\frac{\partial^2 h_1}{\partial x^2}+R_0\gamma+R_0 d\frac{\partial^2 h_1}{\partial x^2}+R_1\gamma+R_1 d\frac{\partial^2 h_1}{\partial x^2}$$
$$=R_0\gamma-\eta+\left(R_0 d-b\eta\right)\frac{\partial^2 h_1}{\partial x^2}+R_1\gamma+R_1 d\frac{\partial^2 h_1}{\partial x^2}$$

.

Plug in $R_0=(1-\phi)\frac{\eta}{\gamma}$ and remove nonlinear term,

$$\frac{\partial h_1}{\partial t}=\gamma R_1+\left((1-\phi)\frac{\eta}{\gamma}d-b\eta\right)\frac{\partial^2 h_1}{\partial x^2}$$

The second equation is

$$\frac{\partial R_1}{\partial t}=(1-\phi)\eta\left(1+b\frac{\partial^2 h_1}{\partial x^2}\right)-\left(R_0+R_1\right)\left(\gamma+d\frac{\partial^2 h_1}{\partial x^2}\right)$$
$$-\kappa\frac{\partial}{\partial x}\left\{\left(R_0+R_1\right)\frac{\partial}{\partial x}\left(\frac{\frac{\partial^2 h_1}{\partial x^2}}{\left(1+\left(\frac{\partial h_1}{\partial x}\right)^2\right)^{\frac{3}{2}}}\right)\right\}+D\frac{\partial^2 R_1}{\partial x^2}-s\frac{\partial}{\partial x}\left\{\left(R_0+R_1\right)\left(\frac{\frac{\partial h_1}{\partial x}}{1+l_d\left(\frac{\partial h_1}{\partial x}\right)^2}\right)\right\}$$

Plug in $R_0=(1-\phi)\frac{\eta}{\gamma}$ and remove nonlinear term,

$$\frac{\partial R_1}{\partial t}=(1-\phi)\eta b\frac{\partial^2 h_1}{\partial x^2}-(1-\phi)\frac{\eta}{\gamma}d\frac{\partial^2 h_1}{\partial x^2}-R_1\gamma-\kappa(1-\phi)\frac{\eta}{\gamma}\frac{\partial^4 h_1}{\partial x^4}+D\frac{\partial^2 R_1}{\partial x^2}-s(1-\phi)\frac{\eta}{\gamma}\frac{\partial^2 h_1}{\partial x^2}$$
$$=-R_1\gamma+D\frac{\partial^2 R_1}{\partial x^2}+\left\{(1-\phi)\eta b-(1-\phi)\frac{\eta}{\gamma}d-s(1-\phi)\frac{\eta}{\gamma}\right\}\frac{\partial^2 h_1}{\partial x^2}-\kappa(1-\phi)\frac{\eta}{\gamma}\frac{\partial^4 h_1}{\partial x^4}$$

A Fourier analysis leads to

$$iw\hat{h}=\gamma\hat{R}_1+\left((1-\phi)\frac{\eta}{\gamma}d-b\eta\right)\left(-k^2\right)\hat{h}_1$$

,

$$iw\hat{R}_1 = -\gamma\hat{R}_1 + D\left(-k^2\right)\hat{R}_1 + \left\{(1-\phi)\eta b - (1-\phi)\frac{\eta}{\gamma}d - s(1-\phi)\frac{\eta}{\gamma}\right\}\left(-k^2\right)\hat{h}_1 - \kappa(1-\phi)\frac{\eta}{\gamma}\left(k^4\right)\hat{h}_1$$

Summarize the equations,

$$\left\{\left((1-\phi)\frac{\eta}{\gamma}d - b\eta\right)k^2 + iw\right\}\hat{h}_1 - \gamma\hat{R}_1 = 0$$

,

$$\left[\left\{(1-\phi)\eta b - (1-\phi)\frac{\eta}{\gamma}d - s(1-\phi)\frac{\eta}{\gamma}\right\}k^2 + \kappa(1-\phi)\frac{\eta}{\gamma}k^4\right]\hat{h}_1 + \left(iw + \gamma + Dk^2\right)\hat{R}_1 = 0$$

.

To have a non-trivial solution, the determinant of the coefficients is equal to zero, which leads to,

$$\left(iw + \gamma + Dk^2\right)\left\{\left((1-\phi)\frac{\eta}{\gamma}d - b\eta\right)k^2 + iw\right\}$$
$$+\gamma\left[\left\{(1-\phi)\eta b - (1-\phi)\frac{\eta}{\gamma}d - s(1-\phi)\frac{\eta}{\gamma}\right\}k^2 + \kappa(1-\phi)\frac{\eta}{\gamma}k^4\right] = 0$$

.

Let $D_1 = \eta b$, $D_2 = \frac{\eta}{\gamma}d$, $s_2 = \frac{\eta}{\gamma}s$ and $K_1 = \frac{\eta}{\gamma}\kappa$, then

$$\left(iw + \gamma + Dk^2\right)\left\{iw - \left(D_1 - (1-\phi)D_2\right)k^2\right\} + \gamma(1-\phi)\left[\left(D_1 - D_2 - s_1\right)k^2 + K_1k^4\right] = 0$$

Expand the equation,

$$-w^2 - \left(D_1 - (1-\phi)D_2\right)k^2 iw + \left(\gamma + Dk^2\right)iw - \left(\gamma + Dk^2\right)\left(D_1 - (1-\phi)D_2\right)k^2$$
$$+\gamma(1-\phi)\left[\left(D_1 - D_2 - s_1\right)k^2 + K_1k^4\right] = 0$$

,

$$-w^2 + \left\{-\left(D_1 - (1-\phi)D_2\right)k^2 i + \left(\gamma + Dk^2\right)i\right\}w$$
$$-\left(\gamma + Dk^2\right)\left(D_1 - (1-\phi)D_2\right)k^2 + \gamma(1-\phi)\left[\left(D_1 - D_2 - s_1\right)k^2 + K_1k^4\right] = 0$$

.

Solving the quadratic equation about w, then we have $w = \alpha + \beta i$. If $\beta < 0$, from $h_1 = \hat{h}_1 \exp(iwt + i\mathbf{kr})$, the temporal term will increase exponentially with the magnitude of $\hat{h}_1 \exp(\beta)$. Figure 2.15 (a) is a graph of β, which is the imaginary part of w.

APPENDIX C

Mie Theory

In this section, the solutions of the scattered electromagnetic field by a spherical particle are reviewed using the notation of Bohren and Huffman[135]. First, we prepare general equations of spherical vectors derived from Maxwell's equations. Then, we will consider a special case for a spherical particle subjected to the electromagnetic field.

Consider Maxwell's equations in the case of time harmonic dependence

$$\nabla \bullet \mathbf{E} = 0 , \tag{2}$$

$$\nabla \bullet \mathbf{H} = 0 , \tag{3}$$

$$\nabla \times \mathbf{E} = i\omega\mu\mathbf{H} , \tag{4}$$

$$\nabla \times \mathbf{H} = -i\omega\varepsilon\mathbf{E} , \tag{5}$$

where $\mathbf{E}$ is the electric field, $\mathbf{H}$ is the magnetic field, ω is the angular frequency, μ is the permeability, and ε is the permittivity. The curl of Equation (3) and (4) is

$$\nabla \times (\nabla \times \mathbf{E}) = i\omega\mu\nabla \times \mathbf{H} = \omega^2\varepsilon\mu\mathbf{E} ,$$

$$\nabla \times (\nabla \times \mathbf{H}) = i\omega\mu\nabla \times \mathbf{E} = \omega^2\varepsilon\mu\mathbf{H} ,$$

and use the vector identity $\nabla \times (\nabla \times \mathbf{A}) = \nabla(\nabla \bullet \mathbf{A}) - \nabla \bullet (\nabla \mathbf{A})$. Then,

$$\nabla^2\mathbf{E} + \mathrm{k}^2\mathbf{E} = 0 , \ \nabla^2\mathbf{H} + \mathrm{k}^2\mathbf{H} = 0 , \tag{6}$$

where $k^2 = \omega^2 \varepsilon \mu$ and $\nabla^2 \mathbf{A} = \nabla \bullet (\nabla \mathbf{A})$. Equations (5) represent $\mathbf{E}$ and $\mathbf{H}$ satisfy the vector wave equation.

Consider a scalar function ψ and an arbitrary constant vector $\mathbf{c}$, and formulate a vector function $\mathbf{M}$ as following,

$$\mathbf{M} = \nabla \times (\mathbf{c}\psi).$$

The divergence of both sides leads to

$$\nabla \bullet \mathbf{M} = 0.$$

Use the vector identities

$$\nabla \times (\mathbf{A} \times \mathbf{B}) = \mathbf{A}(\nabla \bullet \mathbf{B}) - \mathbf{B}(\nabla \bullet \mathbf{A}) + (\mathbf{B} \bullet \nabla)\mathbf{A} - (\mathbf{A} \bullet \nabla)\mathbf{B},$$

$$\nabla (\mathbf{A} \bullet \mathbf{B}) = \mathbf{A} \times (\nabla \times \mathbf{B}) + \mathbf{B} \times (\nabla \times \mathbf{A}) + (\mathbf{B} \bullet \nabla)\mathbf{A} + (\mathbf{A} \bullet \nabla)\mathbf{B}.$$

Then, we have

$$\nabla^2 \mathbf{M} + k^2 \mathbf{M} = \nabla \times \left[\mathbf{c}(\nabla^2 \psi + k^2 \psi) \right].$$

If ψ is the solution of the scalar wave equation $\nabla^2 \psi + k^2 \psi = 0$, $\mathbf{M}$ satisfies the vector wave equation.

Define another vector function

$$\mathbf{N} = \frac{\nabla \times \mathbf{M}}{k}.$$

$\mathbf{N}$ also satisfies $\nabla \bullet \mathbf{N} = 0$ and $\nabla^2 \mathbf{N} + k^2 \mathbf{N} = 0$.

Therefore, $\mathbf{M}$ and $\mathbf{N}$ satisfy the properties of an electromagnetic field; they satisfy the vector wave equation, the divergence of both is zero, and the curl of $\mathbf{M}$ is proportional to $\mathbf{N}$. If we choose the vector constant $\mathbf{c}$ as a radius vector $\mathbf{r}$, then, $\mathbf{M} = \nabla \times (\mathbf{r}\psi)$, representing $\mathbf{M}$ is the solution of the vector wave equation in spherical

polar coordinates. $\mathbf{M}$ and the associated $\mathbf{N}$ can be used as fundamental solutions for the field equation.

The scalar wave equation in spherical polar coordinates is

$$\frac{1}{r^2}\frac{\partial}{\partial r}\left(r^2\frac{\partial\psi}{\partial r}\right)+\frac{1}{r^2\sin\theta}\frac{\partial}{\partial\theta}\left(\sin\theta\frac{\partial\psi}{\partial\theta}\right)+\frac{1}{r^2\sin\theta}\frac{\partial^2\psi}{\partial\phi^2}+\mathrm{k}^2\psi=0. \qquad (7)$$

Assuming the solution of Equation (6) as a form of

$$\psi(r,\theta,\phi)=R(r)\Theta(\theta)\Phi(\phi).$$

When we substitute the solution to Equation (6), three separated equations are derived.

$$\frac{d^2\Phi}{d\phi^2}+m^2\Phi=0, \qquad (8)$$

$$\frac{1}{\sin\theta}\frac{d}{d\theta}\left(\sin\theta\frac{d\Theta}{d\theta}\right)+\left[n(n+1)-\frac{m^2}{\sin^2\theta}\right]\Theta=0, \qquad (9)$$

$$\frac{d}{dr}\left(r^2\frac{dR}{dr}\right)+\left[\mathrm{k}^2r^2-n(n+1)\right]R=0, \qquad (10)$$

The linearly independent solutions of Equation (7) can be written

$$\Phi_e=\cos m\phi,\ \Phi_o=\sin n\phi,$$

where subscripts e and o represent even and odd, respectively. The solutions to Equation (8) are the associated Legendre functions of the first kind $P_n^m(\cos\theta)$ of degree n and order m, where $n=m,m+1,\ldots$. The functions are orthogonal. If we introduce a dimensionless variable $\rho=\mathrm{k}r$, and define a function $Z=R\sqrt{\rho}$, Equation (9) becomes

$$\rho\frac{d}{d\rho}\left(\rho\frac{dZ}{d\rho}\right)+\left[\rho^2-\left(n+\frac{1}{2}\right)^2\right]Z=0. \qquad (11)$$

The linearly independent solutions to Equation (10) are the Bessel functions first and second kind J_v and Y_v where the order $v = n + 1/2$ is half-integral. Therefore, the linearly independent solutions of Equation (9) are the spherical Bessel functions

$$j_n(\rho) = \sqrt{\frac{\pi}{2\rho}} J_{n+1/2}(\rho)\,, y_n(\rho) = \sqrt{\frac{\pi}{2\rho}} Y_{n+1/2}(\rho)\,.$$

Any linear combination of j_n and y_n is also a solution to Equation (9). Let us define combinations, which are called the spherical Bessel functions of the third kind,

$$h_n^{(1)}(\rho) = j_n(\rho) + iy_n(\rho)\,,\ h_n^{(2)}(\rho) = j_n(\rho) - iy_n(\rho)\,. \tag{12}$$

Now we can write the solutions of the scalar wave equation in spherical polar coordinates

$$\psi_{emn} = \cos m\phi P_n^m(\cos\theta) z_n(\mathrm{k}r)\,,$$

$$\psi_{omn} = \sin m\phi P_n^m(\cos\theta) z_n(\mathrm{k}r)\,,$$

where z_n is any spherical Bessel functions of j_n, y_n, $h_n^{(1)}$, and $h_n^{(2)}$.

The vector spherical harmonics generated by the scalar wave equations can be written as

$$\mathbf{M}_{emn} = \nabla \times (\mathbf{r}\psi_{emn})\,,\ \mathbf{M}_{omn} = \nabla \times (\mathbf{r}\psi_{omn})\,,$$

$$\mathbf{N}_{emn} = \frac{\nabla \times \mathbf{M}_{emn}}{\mathrm{k}}\,,\ \mathbf{N}_{omn} = \frac{\nabla \times \mathbf{M}_{omn}}{\mathrm{k}}\,.$$

These equations can be expressed in component forms as

$$\mathbf{M}_{emn} = \frac{-m}{\sin\theta} \sin m\phi P_n^m(\cos\theta) z_n(\rho)\hat{\mathbf{e}}_\theta - \cos m\phi \frac{dP_n^m(\cos\theta)}{d\theta} z_n(\rho)\hat{\mathbf{e}}_\phi\,, \tag{13}$$

$$\mathbf{M}_{omn} = \frac{m}{\sin\theta} \cos m\phi P_n^m(\cos\theta) z_n(\rho)\hat{\mathbf{e}}_\theta - \sin m\phi \frac{dP_n^m(\cos\theta)}{d\theta} z_n(\rho)\hat{\mathbf{e}}_\phi\,, \tag{14}$$

$$\mathbf{N}_{emn} = \frac{z_n(\rho)}{\rho}\cos m\phi n(n+1)P_n^m(\cos\theta)\hat{\mathbf{e}}_r + \cos m\phi \frac{dP_n^m(\cos\theta)}{d\theta}\frac{1}{\rho}\frac{d}{d\rho}\left[\rho z_n(\rho)\right]\hat{\mathbf{e}}_\theta$$
$$-m\sin m\phi \frac{P_n^m(\cos\theta)}{\sin\theta}\frac{1}{\rho}\frac{d}{d\rho}\left[\rho z_n(\rho)\right]\hat{\mathbf{e}}_\phi \quad ,(15)$$

$$\mathbf{N}_{omn} = \frac{z_n(\rho)}{\rho}\sin m\phi n(n+1)P_n^m(\cos\theta)\hat{\mathbf{e}}_r + \sin m\phi \frac{dP_n^m(\cos\theta)}{d\theta}\frac{1}{\rho}\frac{d}{d\rho}\left[\rho z_n(\rho)\right]\hat{\mathbf{e}}_\theta$$
$$+m\cos m\phi \frac{P_n^m(\cos\theta)}{\sin\theta}\frac{1}{\rho}\frac{d}{d\rho}\left[\rho z_n(\rho)\right]\hat{\mathbf{e}}_\phi \quad .(16)$$

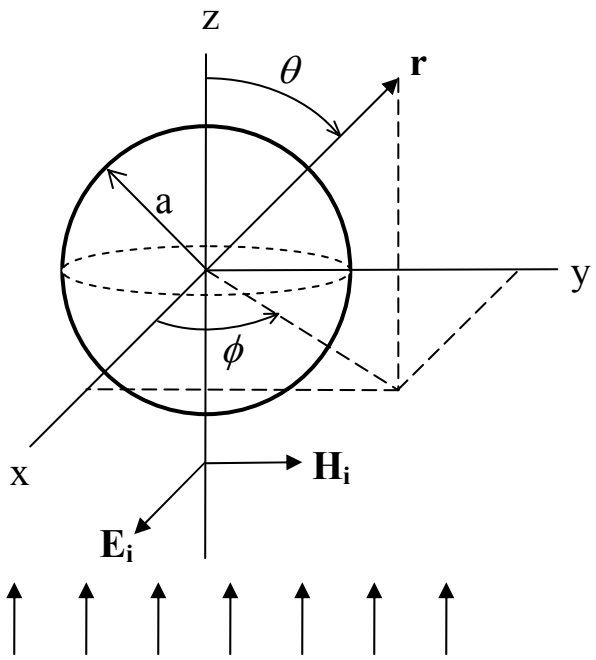

Figure C1. A schematic diagram of a spherical particle subjected to the electromagnetic wave. The polarized wave to the x axis is incident along the z direction. The spherical polar coordinate system has its origin at the center of the particle.

Now we will apply the general equations derived so far to a specific case: a spherical particle subjected to the electromagnetic field. Figure C1 shows the system considered here. We consider scattering of a plane x-polarized wave in spherical polar coordinates. The electric field is written

$$\mathbf{E}_i = E_0 e^{ikr\cos\theta}\hat{\mathbf{e}}_x , \tag{17}$$

where $\hat{\mathbf{e}}_x = \sin\theta\cos\phi\hat{\mathbf{e}}_r + \cos\theta\cos\phi\hat{\mathbf{e}}_\theta - \sin\phi\hat{\mathbf{e}}_\phi$. We can expand Equation (16) in vector spherical harmonics

$$\mathbf{E}_i = \sum_{m=0}^{\infty}\sum_{n=m}^{\infty}(B_{emn}\mathbf{M}_{emn} + B_{omn}\mathbf{M}_{omn} + A_{emn}\mathbf{N}_{emn} + A_{omn}\mathbf{N}_{omn}) .$$

The coefficients are of the form

$$B_{emn} = \frac{\int_0^{2\pi}\int_0^{\pi}\mathbf{E}_i \bullet \mathbf{M}_{emn}\sin\theta d\theta d\phi}{\int_0^{2\pi}\int_0^{\pi}\left|\mathbf{M}_{emn}\right|^2\sin\theta d\theta d\phi} . \tag{18}$$

B_{omn}, A_{emn}, and A_{omn} are in the similar form. From Equation (12), (15), and (16), the orthogonality of the sine and cosine leads to $B_{emn} = A_{omn} = 0$. For the same reason, the remaining coefficients vanish unless $m = 1$. Therefore, the expansion reduces to

$$\mathbf{E}_i = \sum_{n=1}^{\infty}(B_{o1n}\mathbf{M}_{o1n}^{(1)} + A_{e1n}\mathbf{N}_{e1n}^{(1)}) ,$$

where the superscript (1) represents the vector spherical harmonics generated by the spherical Bessel function j_n. Here, y_n is discarded because it is not finite at the origin, which is not appropriate. The mathematical algebra of Equation (17) for B_{o1n} and A_{e1n} leads to respectively,

$$B_{o1n} = i^n E_0\frac{2n+1}{n(n+1)},\ A_{e1n} = -iE_0 i^n\frac{2n+1}{n(n+1)} .$$

Finally, the expansion of a plane wave in spherical harmonics is summarized

$$\mathbf{E}_i = E_0\sum_{n=1}^{\infty} i^n\frac{2n+1}{n(n+1)}(\mathbf{M}_{o1n}^{(1)} - i\mathbf{N}_{e1n}^{(1)}) . \tag{19}$$

Now we consider a plane x-polarized electric field, which is expressed by Equation (18), is incident on a homogeneous, isotropic sphere of a radius a. The associate magnetic field is obtained by the curl

$$\mathbf{H}_i = \frac{-\mathrm{k}}{\omega\mu} E_0 \sum_{n=1}^{\infty} i^n \frac{2n+1}{n(n+1)} (\mathbf{M}_{e1n}^{(1)} + i\mathbf{N}_{o1n}^{(1)}) . \tag{20}$$

We denote the electromagnetic field inside of the sphere as $(\mathbf{E}_t, \mathbf{H}_t)$ and the scattered field as $(\mathbf{E}_s, \mathbf{H}_s)$. The boundary conditions are

$$(\mathbf{E}_i + \mathbf{E}_s - \mathbf{E}_t) \times \hat{\mathbf{e}}_r = (\mathbf{H}_i + \mathbf{H}_s - \mathbf{H}_t) \times \hat{\mathbf{e}}_r = 0 .$$

From the boundary conditions and the orthorgonality of the vector harmonics, the form of inside and scattered fields is similarly derived. The electromagnetic field inside the sphere is written

$$\mathbf{E}_t = \sum_{n=1}^{\infty} E_n (c_n \mathbf{M}_{o1n}^{(1)} - i d_n \mathbf{N}_{e1n}^{(1)}) , \tag{21}$$

$$\mathbf{H}_t = \frac{-\mathrm{k}_t}{\omega\mu_t} \sum_{n=1}^{\infty} E_n (d_n \mathbf{M}_{e1n}^{(1)} + i c_n \mathbf{N}_{o1n}^{(1)}) , \tag{22}$$

where $E_n = i^n E_0 (2n+1)/n(n+1)$, k_t is the wave number in the sphere, and μ_t is the permeability of the sphere. The electromagnetic field scattered out of the sphere is written

$$\mathbf{E}_s = \sum_{n=1}^{\infty} E_n (i a_n \mathbf{N}_{e1n}^{(3)} - b_n \mathbf{M}_{o1n}^{(3)}) , \tag{23}$$

$$\mathbf{H}_s = \frac{\mathrm{k}}{\omega\mu} \sum_{n=1}^{\infty} E_n (i b_n \mathbf{N}_{o1n}^{(3)} + a_n \mathbf{M}_{e1n}^{(3)}) , \tag{24}$$

where the superscript (3) represents vector spherical harmonics generated by the spherical Hankel functions $h_n^{(1)}$, which is introduced in Equation (11). $h_n^{(1)}$ is used

because the infinite behavior of y_n at the origin does not matter outside the sphere. For convenience, define angle-dependent functions

$$\pi_n = \frac{P_n^1}{\sin\theta},\ \tau_n = \frac{dP_n^1}{d\theta}$$

We can rewrite the vector spherical harmonics of Equations (12)-(15) in a simple form with $m = 1$

$$\mathbf{M}_{e1n} = -\sin\phi\pi_n(\cos\theta)z_n(\rho)\hat{\mathbf{e}}_\theta - \cos\phi\tau_n(\cos\theta)z_n(\rho)\hat{\mathbf{e}}_\phi, \tag{25}$$

$$\mathbf{M}_{o1n} = \cos\phi\pi_n(\cos\theta)z_n(\rho)\hat{\mathbf{e}}_\theta - \sin\phi\tau_n(\cos\theta)z_n(\rho)\hat{\mathbf{e}}_\phi, \tag{26}$$

$$\mathbf{N}_{e1n} = \cos\phi n(n+1)\sin\theta\pi_n(\cos\theta)\frac{z_n(\rho)}{\rho}\hat{\mathbf{e}}_r + \cos\phi\tau_n(\cos\theta)\frac{[\rho z_n(\rho)]'}{\rho}\hat{\mathbf{e}}_\theta - \sin\phi\pi_n(\cos\theta)\frac{[\rho z_n(\rho)]'}{\rho}\hat{\mathbf{e}}_\phi, \tag{27}$$

$$\mathbf{N}_{o1n} = \sin\phi n(n+1)\sin(\theta)\pi_n(\cos\theta)\frac{z_n(\rho)}{\rho}\hat{\mathbf{e}}_r + \sin\phi\tau_n(\cos\theta)\frac{[\rho z_n(\rho)]'}{\rho}\hat{\mathbf{e}}_\theta + \cos\phi\pi_n(\cos\theta)\frac{[\rho z_n(\rho)]'}{\rho}\hat{\mathbf{e}}_\phi. \tag{28}$$

To define four unknown coefficients a_n, b_n, c_n, and d_n, four independent equations are needed. From the boundary conditions,

$$E_{i\theta} + E_{s\theta} = E_{t\theta},\ E_{i\phi} + E_{s\phi} = E_{t\phi},$$

$$H_{i\theta} + H_{s\theta} = H_{t\theta},\ H_{i\phi} + H_{s\phi} = H_{t\phi}. \tag{29}$$

From Equations (18)-(28) and the orthogonal relations of

$$\int_0^\pi (\tau_n + \pi_n)(\tau_m + \pi_m)\sin\theta d\theta = \int_0^\pi (\tau_n - \pi_n)(\tau_m - \pi_m)\sin\theta d\theta = 0 \ \ (m \neq n),$$

we can obtain four linear equations

$$j_n(mx)c_n + h_n^{(1)}(x)b_n = j_n(x),$$

$$\mu\left[mxj_n(mx)\right]'c_n+\mu_t\left[xh_n^{(1)}(x)\right]'b_n=\mu_t\left[xj_n(x)\right]',$$

$$\mu mj_n(mx)d_n+\mu_t h_n^{(1)}(x)a_n=\mu_t j_n(x),$$

$$\left[mxj_n(mx)\right]'d_n+m\left[xh_n^{(1)}(x)\right]'a_n=m\left[xj_n(x)\right]',$$

where the size parameter x and the relative refractive index m are defined

$$x=ka=\frac{2\pi Na}{\lambda},\ m=\frac{\mathrm{k_t}}{\mathrm{k}}=\frac{N_t}{N}.$$

N_1 and N are the refractive indices of particle and medium, respectively. The unknown coefficients can be solved from the equations,

$$a_n=\frac{\mu m^2 j_n(mx)\left[xj_n(x)\right]'-\mu_t j_n(x)\left[mxj_n(mx)\right]'}{\mu m^2 j_n(mx)\left[xh_n^{(1)}(x)\right]'-\mu_t h_n^{(1)}(x)\left[mxj_n(mx)\right]'},$$

$$b_n=\frac{\mu_t j_n(mx)\left[xj_n(x)\right]'-\mu j_n(mx)\left[mxj_n(mx)\right]'}{\mu_t j_n(mx)\left[xh_n^{(1)}(x)\right]'-\mu h_n^{(1)}(x)\left[mxj_n(mx)\right]'},$$

$$c_n=\frac{\mu_t j_n(x)\left[xh_n^{(1)}(x)\right]'-\mu_t h_n^{(1)}(x)\left[xj_n(x)\right]'}{\mu_t j_n(mx)\left[xh_n^{(1)}(x)\right]'-\mu h_n^{(1)}(x)\left[mxj_n(mx)\right]'},$$

$$d_n=\frac{\mu_t mj_n(x)\left[xh_n^{(1)}(x)\right]'-\mu_t mh_n^{(1)}(x)\left[xj_n(x)\right]'}{\mu m^2 j_n(mx)\left[xh_n^{(1)}(x)\right]'-\mu_t h_n^{(1)}(x)\left[mxj_n(mx)\right]'}.$$

We are interested in the scattered field. To simplify the equations, introduce the Riccati-Bessel functions

$$\psi_n(\rho)=\rho j_n(\rho),\ \xi_n(\rho)=\rho h_n^{(1)}(\rho).$$

And assume the permeability of the particle and the medium is same. Then,

$$a_n=\frac{m\psi_n(mx)\psi'_n(x)-\psi_n(x)\psi'_n(mx)}{m\psi_n(mx)\xi'_n(x)-\xi_n(x)\psi'_n(mx)},$$

$$b_n = \frac{\psi_n(mx)\psi'_n(x) - m\psi_n(x)\psi'_n(mx)}{\psi_n(mx)\xi'_n(x) - m\xi_n(x)\psi'_n(mx)}.$$

We assume the expansion of the scattered field is convergent. Thus, we can truncate the series after a sufficiently large n_c. If we use an asymptotical expression about the spherical Hankel function given by

$$h_n^{(1)}(kr) \sim \frac{(-i)^n e^{ikr}}{ikr} \quad , kr \gg n^2,$$

the transverse components of the scattered electric field are

$$E_{s\theta} \sim E_0 \frac{e^{ikr}}{-ikr} \cos\phi S_2(\cos\theta),$$

$$E_{s\phi} \sim -E_0 \frac{e^{ikr}}{-ikr} \sin\phi S_1(\cos\theta),$$

where

$$S_1 = \sum_n^{n_c} \frac{2n+1}{n(n+1)} (a_n \pi_n + b_n \tau_n),$$

$$S_2 = \sum_n^{n_c} \frac{2n+1}{n(n+1)} (a_n \tau_n + b_n \pi_n).$$

The scattered light from the incident light that is polarized perpendicular to the scattering plane has the intensity of $|S_1|^2$ and if the incident light is polarized parallel to the plane, the scattered intensity is $|S_2|^2$. These intensities are derived from the relation between incident and scattered Stokes parameters. The scattered intensity from the unpolarized light is

$$\left(|S_1|^2 + |S_2|^2\right)/2.$$

BIBLIOGRAPHY

[1] Karen, A., K. Okuno, F. Soeda, and A. Ishitani, *A study of the secondary-ion yield change on the GaAs surface caused by the O^+_2 ion-beam-induced rippling,* Journal of Vacuum Science & Technology A: Vacuum, Surfaces, and Films, **9**, 2247 (1991)

[2] Elst, K., W. Vandervorst, J. Alay, J. Snauwaert, and L. Hellemans, *Influence of oxygen on the formation of ripples on Si,* Journal of Vacuum Science & Technology B: Microelectronics and Nanometer Structures, **11**, 1968 (1993)

[3] Smirnov, V.K., D.S. Kibalov, S.A. Krivelevich, P.A. Lepshin, E.V. Potapov, R.A. Yankov, W. Skorupa, V.V. Makarov, and A.B. Danilin, *Wave-ordered structures formed on SOI wafers by reactive ion beams,* Nuclear Instruments and Methods in Physics Research Section B: Beam Interactions with Materials and Atoms, **147**, 310 (1999)

[4] Habenicht, S., K.P. Lieb, J. Koch, and A.D. Wieck, *Ripple propagation and velocity dispersion on ion-beam-eroded silicon surfaces,* Physical Review B, **65**, 115327 (2002)

[5] Rusponi, S., G. Costantini, C. Boragno, and U. Valbusa, *Ripple Wave Vector Rotation in Anisotropic Crystal Sputtering,* Physical Review Letters, **81**, 2735 (1998)

[6] Rusponi, S., G. Costantini, C. Boragno, and U. Valbusa, *Scaling Laws of the Ripple Morphology on Cu(110),* Physical Review Letters, **81**, 4184 (1998)

[7] Habenicht, S., W. Bolse, K.P. Lieb, K. Reimann, and U. Geyer, *Nanometer ripple formation and self-affine roughening of ion-beam-eroded graphite surfaces,* Physical Review B, **60**, R2200 (1999)

[8] Habenicht, S., *Morphology of graphite surfaces after ion-beam erosion,* Physical Review B, **63**, 125419 (2001)

[9] Mayer, T.M., E. Chason, and A.J. Howard, *Roughening instability and ion-induced viscous relaxation of SiO2 surfaces,* Journal of Applied Physics, **76**, 1633 (1994)

[10] Duncan, S., R. Smith, D.E. Sykes, and J.M. Walls, *Surface morphology of Si(100), GaAs(100) and InP(100) following O^+_2 and Cs^+ ion bombardment,* Vacuum, **34**, 145 (1984)

[11] Brown, A.-D. and J. Erlebacher, *Temperature and fluence effects on the evolution of regular surface morphologies on ion-sputtered Si(111),* Physical Review B, **72**, 075350 (2005)

[12] Brown, A.-D., J. Erlebacher, W.-L. Chan, and E. Chason, *Transient Topographies of Ion Patterned Si(111),* Physical Review Letters, **95**, 056101 (2005)

[13] Karmakar, P. and D. Ghose, *Nanoscale periodic and faceted structures formation on Si(100) by oblique angle oxygen ion sputtering,* Nuclear Instruments and Methods in Physics Research Section B: Beam Interactions with Materials and Atoms, **230**, 539 (2005)

[14] Adrian, K. and et al., *Minimization of topological defects in ion-induced ripple patterns on silicon,* New Journal of Physics, **10**, 063004 (2008)

[15] Carter, G. and V. Vishnyakov, *Roughening and ripple instabilities on ion-bombarded Si,* Physical Review B, **54**, 17647 (1996)

[16] Chason, E., T.M. Mayer, B.K. Kellerman, D.T. McIlroy, and A.J. Howard, *Roughening instability and evolution of the Ge(001) surface during ion sputtering,* Physical Review Letters, **72**, 3040 (1994)

[17] Rusponi, S., C. Boragno, and U. Valbusa, *Ripple Structure on Ag(110) Surface Induced by Ion Sputtering,* Physical Review Letters, **78**, 2795 (1997)

[18] Erlebacher, J., M.J. Aziz, E. Chason, M.B. Sinclair, and J.A. Floro, *Spontaneous Pattern Formation on Ion Bombarded Si(001),* Physical Review Letters, **82**, 2330 (1999)

[19] Karen, A., Y. Nakagawa, M. Hatada, K. Okuno, F. Soeda, and A. Ishitani, *Quantitative investigation of the O^+_2 -induced topography of GaAs and other III–V semiconductors: An STM study of the ripple formation and suppression of the secondary ion yield change by sample rotation,* Surface and Interface Analysis, **23**, 506 (1995)

[20] Vajo, J.J., R.E. Doty, E. Cirlin, x, and Hee, *Influence of O^+_2 energy, flux, and fluence on the formation and growth of sputtering-induced ripple topography on silicon,* Journal of Vacuum Science & Technology A: Vacuum, Surfaces, and Films, **14**, 2709 (1996)

[21] Ziberi, B., F. Frost, T. Hoche, and B. Rauschenbach, *Ripple pattern formation on silicon surfaces by low-energy ion-beam erosion: Experiment and theory,* Physical Review B, **72**, 235310 (2005)

[22] Stevie, F.A., P.M. Kahora, D.S. Simons, and P. Chi, *Secondary ion yield changes in Si and GaAs due to topography changes during O^+_2 or Cs^+ ion bombardment,* Journal of Vacuum Science & Technology A: Vacuum, Surfaces, and Films, **6**, 76 (1988)

[23] Facsko, S., T. Dekorsy, C. Koerdt, C. Trappe, H. Kurz, A. Vogt, and H.L. Hartnagel, *Formation of Ordered Nanoscale Semiconductor Dots by Ion Sputtering,* Science, **285**, 1551 (1999)

[24] Frost, F., A. Schindler, and F. Bigl, *Roughness Evolution of Ion Sputtered Rotating InP Surfaces: Pattern Formation and Scaling Laws,* Physical Review Letters, **85**, 4116 (2000)

[25] Frost, F. and B. Rauschenbach, *Nanostructuring of solid surfaces by ion-beam erosion,* Applied Physics A: Materials Science & Processing, **77**, 1 (2003)

[26] Frost, F., B. Ziberi, T. H?he, and B. Rauschenbach, *The shape and ordering of self-organized nanostructures by ion sputtering,* Nuclear Instruments and Methods in Physics Research Section B: Beam Interactions with Materials and Atoms, **216**, 9 (2004)

[27] Gago, R., L. Vazquez, R. Cuerno, M. Varela, C. Ballesteros, and J.M. Albella, *Production of ordered silicon nanocrystals by low-energy ion sputtering,* Applied Physics Letters, **78**, 3316 (2001)

[28] Bobek, T., S. Facsko, T. Dekorsy, and H. Kurz, *Ordered quantum dot formation on GaSb surfaces during ion sputtering,* Nuclear Instruments and Methods in Physics Research Section B: Beam Interactions with Materials and Atoms, **178**, 101 (2001)

[29] S. Facsko, T.B.T.D.H.K., *Ordered Quantum Dot Formation by Ion Sputtering,* physica status solidi (b), **224**, 537 (2001)

[30] Ziberi, B., F. Frost, and B. Rauschenbach, *Pattern transitions on Ge surfaces during low-energy ion beam erosion,* Applied Physics Letters, **88**, 173115 (2006)

[31] Ziberi, B., F. Frost, T. Hoche, and B. Rauschenbach, *Ion-induced self-organized dot and ripple patterns on Si surfaces,* Vacuum, **81**, 155 (2006)

[32] Gago, R., L. Vazquez, O. Plantevin, T.H. Metzger, J. Munoz-Garcia, R. Cuerno, and M. Castro, *Order enhancement and coarsening of self-organized silicon nanodot patterns induced by ion-beam sputtering,* Applied Physics Letters, **89**, 233101 (2006)

[33] Ziberi, B., F. Frost, and B. Rauschenbach, *Self-organized dot patterns on Si surfaces during noble gas ion beam erosion,* Surface Science, **600**, 3757 (2006)

[34] Gago, R., aacute, L. zquez, O. Plantevin, aacute, G. nchez, iacute, J.A. a, M. Varela, M.C. Ballesteros, J.M. Albella, and T.H. Metzger, *Temperature influence on the production of nanodot patterns by ion beam sputtering of Si(001),* Physical Review B, **73**, 155414 (2006)

[35] Allmers, T., M. Donath, and G. Rangelov, *Pattern formation by erosion sputtering on GaSb: Transition from dot to ripple formation and influence of impurities,* Journal of Vacuum Science & Technology B: Microelectronics and Nanometer Structures, **24**, 582 (2006)

[36] Ziberi, B., F. Frost, M. Tartz, H. Neumann, and B. Rauschenbach, *Ripple rotation, pattern transitions, and long range ordered dots on silicon by ion beam erosion,* Applied Physics Letters, **92**, 063102 (2008)

[37] MacLaren, S.W., J.E. Baker, N.L. Finnegan, and C.M. Loxton, *Surface roughness development during sputtering of GaAs and InP: Evidence for the role of surface diffusion in ripple formation and sputter cone development,* Journal of Vacuum Science & Technology A: Vacuum, Surfaces, and Films, **10**, 468 (1992)

[38] Datta, D., S.R. Bhattacharyya, T.K. Chini, and M.K. Sanyal, *Evolution of surface morphology of ion sputtered GaAs(1 0 0),* Nuclear Instruments and Methods in Physics Research Section B: Beam Interactions with Materials and Atoms, **193**, 596 (2002)

[39] Schoendorfer, C., A. Lugstein, and E. Bertagnolli, *Focused ion beam induced nanodot and nanofiber growth,* Microelectronic Engineering, **83**, 1491 (2006)

[40] Rose, F. and et al., *Real-time observation of FIB-created dots and ripples on GaAs,* Nanotechnology, **19**, 035301 (2008)

[41] Qiangmin, W., L. Jie, L. Wei, and W. Lumin, *Highly Ordered Ga Nanodroplets on a GaAs Surface Formed by a Focused Ion Beam,* Physical Review Letters, **100**, 076103 (2008)

[42] Wu, J.H., W. Ye, B.L. Cardozo, D. Saltzman, K. Sun, H. Sun, J.F. Mansfield, and R.S. Goldman, *Formation and coarsening of Ga droplets on focused-ion-beam irradiated GaAs surfaces,* Applied Physics Letters, **95**, 153107 (2009)

[43] Lugstein, A., B. Basnar, and E. Bertagnolli, *Size and site controlled Ga nanodots on GaAs seeded by focused ion beams,* Journal of Vacuum Science & Technology B: Microelectronics and Nanometer Structures, **22**, 888 (2004)

[44] Tan, S.K., R. Liu, C.H. Sow, and A.T.S. Wee, *Self-organized nanodot formation on InP(100) by oxygen ion sputtering,* Nuclear Instruments and Methods in Physics Research Section B: Beam Interactions with Materials and Atoms, **248**, 83 (2006)

[45] Bradley, R.M. and M.E.H. James, *Theory of ripple topography induced by ion bombardment,* Journal of Vacuum Science & Technology A: Vacuum, Surfaces, and Films, **6**, 2390 (1988)

[46] Sigmund, P., *A mechanism of surface micro-roughening by ion bombardment,* Journal of Materials Science, **8**, 1545 (1973)

[47] Cuerno, R., Barab, aacute, A.-L. si, aacute, szl, and oacute, *Dynamic Scaling of Ion-Sputtered Surfaces,* Physical Review Letters, **74**, 4746 (1995)

[48] Park, S., B. Kahng, H. Jeong, Barab, aacute, and A.L. si, *Dynamics of Ripple Formation in Sputter Erosion: Nonlinear Phenomena,* Physical Review Letters, **83**, 3486 (1999)

[49] Kahng, B., H. Jeong, and A.L. Barabasi, *Quantum dot and hole formation in sputter erosion,* Applied Physics Letters, **78**, 805 (2001)

[50] Kim, T.C., C.M. Ghim, H.J. Kim, D.H. Kim, D.Y. Noh, N.D. Kim, J.W. Chung, J.S. Yang, Y.J. Chang, T.W. Noh, B. Kahng, and J.S. Kim, *Kinetic Roughening of Ion-Sputtered Pd(001) Surface: Beyond the Kuramoto-Sivashinsky Model,* Physical Review Letters, **92**, 246104 (2004)

[51] Facsko, S., T. Bobek, A. Stahl, H. Kurz, and T. Dekorsy, *Dissipative continuum model for self-organized pattern formation during ion-beam erosion,* Physical Review B, **69**, 153412 (2004)

[52] Paniconi, M. and K.R. Elder, *Stationary, dynamical, and chaotic states of the two-dimensional damped Kuramoto-Sivashinsky equation,* Physical Review E, **56**, 2713 (1997)

[53] Vogel, S. and S.J. Linz, *How ripples turn into dots: Modeling ion-beam erosion under oblique incidence,* Europhys. Lett., **76**, 884 (2006)

[54] Castro, M., R. Cuerno, aacute, L. zquez, R. Gago, and uacute, *Self-Organized Ordering of Nanostructures Produced by Ion-Beam Sputtering,* Physical Review Letters, **94**, 016102 (2005)

[55] Aste, T. and U. Valbusa, *Surface instabilities in granular matter and ion-sputtered surfaces,* Physica A: Statistical Mechanics and its Applications, **332**, 548 (2004)

[56] Valbusa, T.A.a.U., *Ripples and ripples: from sandy deserts to ion-sputtered surfaces,* New Journal of Physics, **7**, 122 (2005)

[57] Munoz-Garcia, J., R. Cuerno, and M. Castro, *Short-range stationary patterns and long-range disorder in an evolution equation for one-dimensional interfaces,* Physical Review E (Statistical, Nonlinear, and Soft Matter Physics), **74**, 050103 (2006)

[58] Munoz-Garcia, J., M. Castro, and R. Cuerno, *Nonlinear Ripple Dynamics on Amorphous Surfaces Patterned by Ion Beam Sputtering,* Physical Review Letters, **96**, 086101 (2006)

[59] Javier, M.-G. and et al., *Coupling of morphology to surface transport in ion-beam-irradiated surfaces: normal incidence and rotating targets,* Journal of Physics: Condensed Matter, **21**, 224020 (2009)

[60] Alkemade, P.F.A., *Propulsion of Ripples on Glass by Ion Bombardment,* Physical Review Letters, **96**, 107602 (2006)

[61] Yewande, E.O., A.K. Hartmann, and R. Kree, *Propagation of ripples in Monte Carlo models of sputter-induced surface morphology,* Physical Review B, **71**, 195405 (2005)

[62] Yewande, E.O., R. Kree, and A.K. Hartmann, *Morphological regions and oblique-incidence dot formation in a model of surface sputtering,* Physical Review B, **73**, 115434 (2006)

[63] Bradley, R.M. and M.E.H. James, *Theory of ripple topography induced by ion bombardment,* Journal of Vacuum Science & Technology A: Vacuum, Surfaces, and Films, **6**, 2390 (1988)

[64] Barabasi, A.-L. and H.E. Stanley, *Fractal Concepts in Surface Growth*. Cambridge: Cambridge University Press. (1995)

[65] Bobek, T., S. Facsko, H. Kurz, T. Dekorsy, M. Xu, and C. Teichert, *Temporal evolution of dot patterns during ion sputtering,* Physical Review B, **68**, 085324 (2003)

[66] Mullins, W.W., *Theory of Thermal Grooving,* Journal of Applied Physics, **28**, 333 (1957)

[67] Vogel, S. and S.J. Linz, *How ripples turn into dots: Modeling ion-beam erosion under oblique incidence,* Europhysics Letters, **76**, 884 (2006)

[68] Golovin, A.A., M.S. Levine, T.V. Savina, and S.H. Davis, *Faceting instability in the presence of wetting interactions: A mechanism for the formation of quantum dots,* Physical Review B, **70**, 235342 (2004)

[69] Balzani, V., A. Credi, F.M. Raymo, and J.F. Stoddart, *Artificial Molecular Machines,* Angewandte Chemie, **39**, 3348 (2000)

[70] Balzani, V., M. Gomez-Lopez, and J.F. Stoddart, *Molecular Machines,* Accounts of Chemical Research, **31**, 405 (1998)

[71] Ballardini, R., V. Balzani, A. Credi, M.T. Gandolfi, and M. Venturi, *Artificial Molecular-Level Machines: Which Energy To Make Them Work?,* Accounts of Chemical Research, **34**, 445 (2001)

[72] Klajn, R., J.F. Stoddart, and B.A. Grzybowski, *Nanoparticles functionalised with reversible molecular and supramolecular switches,* Chemical Society Reviews, **39**, 2203 (2010)

[73] Angelos, S., E. Johansson, J.F. Stoddart, and J.I. Zink, *Mesostructured Silica Supports for Functional Materials and Molecular Machines,* Advanced Functional Materials, **17**, 2261 (2007)

[74] Huang, T.J., *Recent Developments in Artificial Molecular Machine-Based Active Nanomaterials and Nanosystems,* MRS Bulletin, **33**, 226 (2008)

[75] Yoon, I., D. Benítez, Y.-L. Zhao, O.Š. Miljanić, S.-Y. Kim, E. Tkatchouk, K.C.F. Leung, S.I. Khan, W.A. Goddard, and J.F. Stoddart, *Functionally Rigid and Degenerate Molecular Shuttles,* Chemistry – A European Journal, **15**, 1115 (2009)

[76] Nguyen, T.D., K.C.F. Leung, M. Liong, C.D. Pentecost, J.F. Stoddart, and J.I. Zink, *Construction of a pH-Driven Supramolecular Nanovalve,* Organic Letters, **8**, 3363 (2006)

[77] Badjic, J.D., C.M. Ronconi, J.F. Stoddart, V. Balzani, S. Silvi, and A. Credi, *Operating Molecular Elevators,* Journal of the American Chemical Society, **128**, 1489 (2006)

[78] Claessens, C.G. and J.F. Stoddart, *π–π INTERACTIONS IN SELF-ASSEMBLY,* Journal of Physical Organic Chemistry, **10**, 254 (1997)

[79] Hunter, C.A. and J.K.M. Sanders, *The nature of .pi.-.pi. interactions,* Journal of the American Chemical Society, **112**, 5525 (1990)

[80] Juluri, B.K., A.S. Kumar, Y. Liu, T. Ye, Y.-W. Yang, A.H. Flood, L. Fang, J.F. Stoddart, P.S. Weiss, and T.J. Huang, *A Mechanical Actuator Driven Electrochemically by Artificial Molecular Muscles,* ACS Nano, **3**, 291 (2009)

[81] Ye, T., A.S. Kumar, S. Saha, T. Takami, T.J. Huang, J.F. Stoddart, and P.S. Weiss, *Changing Stations in Single Bistable Rotaxane Molecules under Electrochemical Control,* ACS Nano, **4**, 3697 (2010)

[82] Brouwer, A.M., C. Frochot, F.G. Gatti, D.A. Leigh, L.c. Mottier, F. Paolucci, S. Roffia, and G.W.H. Wurpel, *Photoinduction of Fast, Reversible Translational Motion in a Hydrogen-Bonded Molecular Shuttle,* Science, **291**, 2124 (2001)

[83] Serreli, V., C.-F. Lee, E.R. Kay, and D.A. Leigh, *A molecular information ratchet,* Nature, **445**, 523 (2007)

[84] Berna, J., D.A. Leigh, M. Lubomska, S.M. Mendoza, E.M. Perez, P. Rudolf, G. Teobaldi, and F. Zerbetto, *Macroscopic transport by synthetic molecular machines,* Nat Mater, **4**, 704 (2005)

[85] Anelli, P.L., N. Spencer, and J.F. Stoddart, *A molecular shuttle,* Journal of the American Chemical Society, **113**, 5131 (1991)

[86] Tseng, H.-R., S.A. Vignon, and J.F. Stoddart, *Toward Chemically Controlled Nanoscale Molecular Machinery,* Angewandte Chemie, **115**, 1529 (2003)

[87] Collier, C.P., E.W. Wong, Belohradsk, yacute, M., F.M. Raymo, J.F. Stoddart, P.J. Kuekes, R.S. Williams, and J.R. Heath, *Electronically Configurable Molecular-Based Logic Gates,* Science, **285**, 391 (1999)

[88] Luo, Y., C.P. Collier, J.O. Jeppesen, K.A. Nielsen, E. DeIonno, G. Ho, J. Perkins, H.-R. Tseng, T. Yamamoto, J.F. Stoddart, and J.R. Heath, *Two-Dimensional Molecular Electronics Circuits,* ChemPhysChem, **3**, 519 (2002)

[89] Dichtel, W.R., J.R. Heath, and J.F. Stoddart, *Designing Bistable [2]Rotaxanes for Molecular Electronic Devices,* Philosophical Transactions: Mathematical, Physical and Engineering Sciences, **365**, 1607 (2007)

[90] Tony Jun, H., B. Branden, H. Chih-Ming, L. Yi, H.F. Amar, A.B. Paul, T. Hsian-Rong, J.F. Stoddart, B. Marko, and M. Sergei, *A nanomechanical device based on linear molecular motors,* Appl. Phys. Lett., **85**, 5391 (2004)

[91] Liu, Y., A.H. Flood, P.A. Bonvallet, S.A. Vignon, B.H. Northrop, H.R. Tseng, J.O. Jeppesen, T.J. Huang, B. Brough, M. Baller, S. Magonov, S.D. Solares, W.A. Goddard, C.M. Ho, and J.F. Stoddart, *Linear Artificial Molecular Muscles,* J. Am. Chem. Soc., **127**, 9745 (2005)

[92] Jang, S.S., Y.H. Jang, Y.H. Kim, W.A. Goddard, A.H. Flood, B.W. Laursen, H.R. Tseng, J.F. Stoddart, J.O. Jeppesen, J.W. Choi, D.W. Steuerman, E. DeIonno, and J.R. Heath, *Structures and Properties of Self-Assembled Monolayers of Bistable [2]Rotaxanes on Au (111) Surfaces from Molecular Dynamics Simulations Validated with Experiment,* J. Am. Chem. Soc., **127**, 1563 (2005)

[93] Grabuleda, X., P. Ivanov, and C. Jaime, *Computational Studies on Pseudorotaxanes by Molecular Dynamics and Free Energy Perturbation Simulations,* J Org. Chem., **68**, 1539 (2003)

[94] Grabuleda, X., P. Ivanov, and C. Jaime, *Shuttling Process in [2]Rotaxanes. Modeling by Molecular Dynamics and Free Energy Perturbation Simulations,* J. Phys. Chem. B, **107**, 7582 (2003)

[95] Briquet, L., N. Staelens, L. Leherte, and D.P. Vercauteren, *Structural, energetic, and dynamical properties of rotaxanes constituted of [alpha]-cyclodextrins and an azobenzene chain,* J Mol Graph Model., **26**, 104 (2007)

[96] Jang, Y.H., S.S. Jang, and W.A. Goddard, *Molecular Dynamics Simulation Study on a Monolayer of Half [2]Rotaxane Self-Assembled on Au(111),* J. Am. Chem. Soc., **127**, 4959 (2005)

[97] Jang, S.S., Y.H. Jang, Y.-H. Kim, W.A. Goddard, J.W. Choi, J.R. Heath, B.W. Laursen, A.H. Flood, J.F. Stoddart, K. Norgaard, and T. Bjornholm, *Molecular Dynamics Simulation of Amphiphilic Bistable [2]Rotaxane Langmuir Monolayers at the Air/Water Interface,* J. Am. Chem. Soc., **127**, 14804 (2005)

[98] Jang, S.S., S.-T. Lin, P.K. Maiti, M. Blanco, W.A. Goddard, P. Shuler, and Y. Tang, *Molecular Dynamics Study of a Surfactant-Mediated Decane−Water Interface: Effect of Molecular Architecture of Alkyl Benzene Sulfonate,* J. Phys. Chem. B, **108**, 12130 (2004)

[99] Plimpton, S., *Fast Parallel Algorithms for Short-Range Molecular Dynamics,* J. Comput. Phys., **117**, 1 (1995)

[100] Verlet, L., *Computer "Experiments" on Classical Fluids. I. Thermodynamical Properties of Lennard-Jones Molecules,* Phys. Rev., **159**, 98 (1967)

[101] Shuichi, N., *A unified formulation of the constant temperature molecular dynamics methods,* J. Chem. Phys., **81**, 511 (1984)

[102] Hoover, W.G., *Canonical dynamics: Equilibrium phase-space distributions,* Phys. Rev. A, **31**, 1695 (1985)

[103] Mayo, S.L., B.D. Olafson, and W.A. Goddard, III, *DREIDING: A generic force field for molecular simulations,* J. Phys. Chem., **94**, 8897 (1990)

[104] www.gaussian.com,

[105] http://www.cdc.gov/malaria/about/facts.html.

[106] http://cdc-malaria.ncsa.uiuc.edu/.

[107] http://www.cdc.gov/malaria/about/biology/index.html.

[108] http://www.cdc.gov/malaria/diagnosis_treatment/diagnosis.html.

[109] http://www.cdc.gov/malaria/about/biology/parasites.html.

[110] Van Ooij, C. and K. Haldar, *Protein export from Plasmodium parasites,* Cellular Microbiology, **9**, 1086 (2007)

[111] Park, Y., M. Diez-Silva, G. Popescu, G. Lykotrafitis, W. Choi, M. S.Feld, and S. Sutresh, *Refractive index maps and membrane dynamics of human red blood cells parasiteized by Plasmodium falciparum,* Proceedings of the National Academy of Sciences of the United States of America, **105**, 13730 (2008)

[112] Gollin, D. and C. Zimmermann, *Malaria:Disease Impacts and Long-Run Income Differences,* IZA Discussion Paper No. 2997, (2007)

[113] Wood, B.R. and D. McNaughton, *Resonance Raman spectroscopy in malaria research,* Expert review of proteomics, **3**, 525 (2006)

[114] Castagner, J.-L. and I.J. Bigio, *Particle sizing with a fast polar nephelometer,* Appl. Opt., **46**, 527 (2007)

[115] Mourant, J.R., I.J. Bigio, J. Boyer, R.L. Conn, T. Johnson, and T. Shimada, *Spectroscopic diagnosis of bladder cancer with elastic light scattering,* Lasers in Surgery and Medicine, **17**, 350 (1995)

[116] Dhar, A., K.S. Johnson, M.R. Novelli, S.G. Bown, I.J. Bigio, L.B. Lovat, and S.L. Bloom, *Elastic scattering spectroscopy for the diagnosis of colonic lesions: initial results of a novel optical biopsy technique,* Gastrointestinal Endoscopy, **63**, 257 (2006)

[117] Gurjar, R.S., V. Backman, L.T. Perelman, I. Georgakoudi, K. Badizadegan, I. Itzkan, R.R. Dasari, and M.S. Feld, *Imaging human epithelial properties with polarized light-scattering spectroscopy,* Nat Med, **7**, 1245 (2001)

[118] Dunn, A.K., H. Bolay, M.A. Moskowitz, and D.A. Boas, *Dynamic Imaging of Cerebral Blood Flow Using Laser Speckle,* J Cereb Blood Flow Metab, **21**, 195 (2001)

[119] Bigio, I.J., S.G. Bown, G. Briggs, C. Kelley, S. Lakhani, D. Pickard, P.M. Ripley, I.G. Rose, and C. Saunders, *Diagnosis of breast cancer using elastic-scattering spectroscopy,* Journal of Biomedical Optics, **5**, (2000)

[120] Mulvery, c.S., A.L. Curtis, S.K. Singh, and I.J. Bigio, *Elastic Scattering Spectroscopy as a Diagnostic Tool for Apoptosis in Cell Cultures,* IEEE Journal of Selected Topics in Quantum Electronic, **13**, 1663 (2007)

[121] Goldberg, D.E., A.F.G. Slater, A. Cerami, and G.B. Henderson, *Hemoglobin Degradation in the Malaria Parasite Plasmodium falciparum: An Ordered Process in a Unique Organelle,* Proceedings of the National Academy of Sciences of the United States of America, **87**, 2931 (1990)

[122] Park, Y., M. Diez-Silva, D. Fu, G. Popescu, W. Choi, I. Barman, S. Suresh, and M.S. Feld, *Static and dynamic light scattering of healthy and malaria-parasite invaded red blood cells,* Journal of Biomedical Optics Letters, **15**, 020506 (2010)

[123] Suresh, S., J. Spatz, J.P. Mills, A. Micoulet, M. Dao, C.T. Lim, M. Beil, and T. Seufferlein, *Connections between single-cell biomechanics and human disease states: gastrointestinal cancer and malaria,* Acta Biomaterialia, **1**, 15 (2005)

[124] Cooke, B.M., N. Mohandas, and R.L. Coppel, *The malaria-infected red blood cell: Structural and functional changes*, in *Advances in Parasitology*. Academic Press. 1. (2001),

[125] Steinke, J.M. and A.P. Shepherd, *Comparison of Mie theory and the light scattering of red blood cells,* Appl. Opt., **27**, 4027 (1988)

[126] Hammer, M., D. Schweitzer, B. Michel, E. Thamm, and A. Kolb, *Single Scattering by Red Blood Cells,* Appl. Opt., **37**, 7410 (1998)

[127] Tycko, D.H., M.H. Metz, E.A. Epstein, and A. Grinbaum, *Flow-cytometric light scattering measurement of red blood cell volume and hemoglobin concentration,* Appl. Opt., **24**, 1355 (1985)

[128] He, J., A. Karlsson, J. Swartling, and S. Andersson-Engels, *Light scattering by multiple red blood cells,* J. Opt. Soc. Am. A, **21**, 1953 (2004)

[129] Tsinopoulos, S.V., E.J. Sellountos, and D. Polyzos, *Light Scattering by Aggregated Red Blood Cells,* Appl. Opt., **41**, 1408 (2002)

[130] Nilsson, A.M.K., P. Alsholm, A. Karlsson, and S. Andersson-Engels, *T-Matrix Computations of Light Scattering by Red Blood Cells,* Appl. Opt., **37**, 2735 (1998)

[131] Serebrennikova, Y.M., J. Patel, and L.H. Garcia-Rubio, *Interpretation of the ultraviolet-visible spectra of malaria parasite Plasmodium falciparum,* Appl. Opt., **49**, 180

[132] Trager, W. and J. Jensen, *Human malaria parasites in continuous culture,* Science, **193**, 673 (1976)

[133] Epstein, M. and L. Garlaschelli, *Better Blood Through Chemistry: A Laboratory Replication of a Miracle,* Journal of Scientific Exploration, **6**, 233 (1992)

[134] Brough, B., B.H. Northrop, J.J. Schmidt, H.-R. Tseng, K.N. Houk, J.F. Stoddart, and C.-M. Ho, *Evaluation of synthetic linear motor-molecule actuation energetics,* Proceedings of the National Academy of Sciences, **103**, 8583 (2006)

[135] Bohren, C.F. and D.R. Huffman, Absorption and Scattering of Light by Small Particles. New York: Wiley. (1983)